

A Finite Difference Representation of Neutrino Radiation Hydrodynamics for Spherically Symmetric General Relativistic Supernova Simulations

Matthias Liebendörfer^{1,2,4}, O. E. Bronson Messer^{1,2,5}, Anthony Mezzacappa²,
Stephen W. Bruenn³, Christian Y. Cardall^{1,2,5}, and F.-K. Thielemann⁴

ABSTRACT

We outline an implicit finite difference representation for general relativistic radiation hydrodynamics in spherical symmetry. Our code, AGILE-BOLTZTRAN, solves a full Boltzmann equation for the angular and spectral neutrino distribution functions in self-consistent simulations of stellar core collapse and postbounce evolution. It implements a dynamically adaptive grid in the comoving metric of Misner and Sharp. This metric evokes a multitude of observer corrections in the formulation of the transport equation. We choose the finite differencing of microscopic terms in the Boltzmann equation such that basic requirements of derived macroscopic physical quantities are ensured, e.g. the diffusion limit, or an accurate conservation of global energy and lepton number. We test the new gravitational and dynamical terms in our code and perform a detailed energy conservation analysis in the evolution of a 40 solar mass progenitor star. We comment on two representative simulations, initiated from very different stellar progenitors, and present our first self-consistent simulation that reaches black hole formation. Based on standard nuclear and weak interaction physics, we investigate the origin of the neutrino luminosities, supplementing the concept of neutrinospheres with a more detailed statistical description of escaping neutrinos. We compare the evolution of a 13 solar mass progenitor to corresponding simulations employing the multi-group flux-limited diffusion approximation with a recently developed sophisticated flux limiter. We find solid agreement in all phases of the postbounce evolution and validate this MGFLD approximation for spherically symmetric supernova simulations.

Subject headings: supernovae: general—neutrinos—radiative transfer—hydrodynamics—relativity—methods: numerical

¹Department of Physics and Astronomy, University of Tennessee, Knoxville, Tennessee 37996-1200

²Physics Division, Oak Ridge National Laboratory, Oak Ridge, Tennessee 37831-6354

³Department of Physics, Florida Atlantic University, Boca Raton, Florida 33431-0991

⁴Department of Physics and Astronomy, University of Basel, Klingelbergstrasse 82, 4056 Basel, Switzerland

⁵Joint Institute for Heavy Ion Research, Oak Ridge National Laboratory, Oak Ridge, Tennessee 37831-6374

1. Neutrino transport in supernovae

A supernova explosion is a dramatic event which includes such a rich diversity of physics (Bethe 1990; Janka, Kifonidis & Rampp 2001) that self-consistent numerical simulations on current computer hardware do not allow the inclusion all relevant pieces at once. After stellar core collapse, a nascent neutron star is formed at the center of the event, requiring a description in general relativity. Neutrinos generated in the compactifying region are tightly coupled to the matter at high densities, while they leak or stream out at lower densities. The collapsing stellar core bounces as the equation of state stiffens when nuclear densities are exceeded, and a shock wave is formed that ploughs outwards through the still infalling outer layers. Multi-frequency radiation hydrodynamics must be used to quantify the energy that these neutrinos deposit in the material behind the shock. This energy deposition has been considered to be essential for the success or failure of the supernova explosion (Colgate & White 1966; Wilson 1985; Bethe & Wilson 1985). Observational and theoretical evidence suggests that this neutrino heating drives convection behind the shock. Instabilities in the proto neutronstar, significant rotation, and strong magnetic fields further complicate the picture. Observations of neutron star kicks, mixing of nuclear species, inhomogeneous ejecta, and polarization of spectra support the presence of asymmetries in supernova explosions (Tueller et al. 1991; Strom et al. 1995; Galama et al. 1998; Leonard et al. 2000). Motivated by such observations, the neutrino driven explosion mechanism has been explored in multidimensions (Herant, Benz, & Colgate 1992; Miller, Wilson, & Mayle 1993; Herant et al. 1994; Burrows, Hayes, & Fryxell 1995; Janka & Müller 1996; Mezzacappa et al. 1998; Fryer & Heger 2000; Fryer & Warren 2002), and alternative jet-based explosion scenarios have received new momentum (Höflich, Wheeler, & Wang 1999; Khoklov et al. 1999; MacFadyen & Woosley 1999; Wheeler et al. 2000).

Because of their excessive computational demand, multi-dimensional simulations have had to rely on physically significant approximations. Simulations are performed that impose the neutrino radiation field externally or uniformly, that prescribe the neutrino spectrum *ab initio*, that artificially seed instabilities, or that insert jets in order to explore important phenomena of supernova explosions evident in observational data. A complementary approach is to model supernovae in spherical symmetry. Spherically symmetric simulations of stellar core collapse reach back to the late sixties (Colgate & White 1966; May & White 1967; Arnett 1967; Schwartz 1967; Wilson 1971) when computers first became available. Although the assumption of pure spherical symmetry is also a physically significant simplification, it can provide an essential contribution to the quality of numerical supernova models and their interpretation. A spherically symmetric model may easily implement full general relativity. Additionally, the reduced number of computational zones allows an accurate treatment of neutrino radiation transport and the inclusion of sophisticated microscopic input physics. During the search for a robust supernova mechanism, standards in the nuclear input physics (Lattimer & Swesty 1991) and weak interaction physics (Bruenn 1985) have been established. Recognizing the importance of neutrino transport in the supernova, its numerical treatment has been improved from simple leakage schemes (Van Riper & Lattimer 1981; Baron,

Cooperstein, & Kahana 1985) to multi-group flux limited diffusion (MGFLD) approximations (Arnett 1977; Bowers & Wilson 1982; Bruenn 1985; Myra et al 1987) to investigations of the full Boltzmann transport equation (Mezzacappa & Bruenn 1993a; Messer et al. 1998; Yamada, Janka, & Suzuki 1999; Burrows et al. 2000; Rampp & Janka 2002). Only recently have self-contained simulations of stellar core collapse and postbounce evolution with Boltzmann neutrino transport been performed (Rampp & Janka 2000), with standard nuclear and weak interaction physics in the $O(v/c)$ limit (Mezzacappa et al. 2001), and in general relativistic space-time (Liebendörfer et al. 2001). In addition to the exploration of the physics of nuclear processes under extreme conditions, spherically symmetric and fully self-contained supernova simulations aim to provide a solid foundation and a reference point for more involved future multidimensional approaches.

Basic numerical techniques for radiative transfer have been designed and continuously improved over the last three decades (see e.g. (Mihalas & Mihalas 1984) and (Lewis & Miller 1993) for a review). In most applications, photons or neutrons are the transported particles. In our application to supernova dynamics, the transport of neutrinos requires a new combination of capabilities derived from both fields, photon and neutron transport.

As in *neutron transport* the radiation particles are fermions. In contrast to photon transport, the neutrinos assume in thermodynamic equilibrium a Fermi-Dirac distribution. Weak interactions with nuclear matter are suppressed due to Pauli blocking of final states, and the compression of trapped fermions in a dynamical simulation may lead to the population of higher energy states. This particular situation has barely been considered within neutron transport because free neutrons in the laboratory do not reach degeneracy. However, accurate knowledge of the neutrino spectrum is a prerequisite for the reliable calculation of the highly energy dependent particle-fluid interaction rates. We therefore split the particles into multiple energy groups and propagate them separately, while allowing for coupling by local interactions via emission, absorption and scattering.

Several quantities have to be evolved with special care: First, an important constraint is the lepton number conservation law, that applies to the neutrinos (and electrons). Whether we choose a kinetic equation for the propagation of particle number or an equation prescribing the evolution of radiation intensity, it is a numerical challenge to conserve both lepton number and energy with the same finite difference representation of the transport equation. While applications to photon transport do not require an exact count of photons as particles, the outcome of a supernova simulation sensitively depends on deleptonization *and* energy transport. The transfer of lepton number occurs via the reactions $e^- + p^+ \rightleftharpoons n + \nu_e$ and $e^+ + n \rightleftharpoons p + \bar{\nu}_e$ where the protons, p , and neutrons, n , are free or bound in nuclei. The electron neutrino, ν_e , and antineutrino, $\bar{\nu}_e$, may escape to infinity or be absorbed at distant locations. These reactions determine the partial pressure of the electron gas by the electron fraction in the fluid elements. As long as the electron gas is degenerate, this pressure contribution has a strong impact on the fluid dynamics at densities below nuclear density. Second, the energy transport is crucial for the evolution of the fluid temperature. The small fraction of energy deposited behind the shock by the absorption of otherwise escaping neutrinos is believed to maintain the support of the shock by thermal pressure and to ultimately

launch a supernova explosion with the ejection of the outer layers (Colgate & White 1966; Bethe & Wilson 1985). Last, but not least, the evolution of global energy is as important as the microscopic energy transport. Just before collapse, the progenitor star is marginally bound. During collapse, the binding energy of the nascent protoneutron star increases dramatically. It is balanced by the internal energy of the compressed matter, having a fluid and a radiative neutrino component. Only on a longer time scale is the energy of the radiation field transported away from the star while the emptied states in the neutrino phase space are immediately replenished by neutrino emission in the cooling protoneutron star. Since the gravitational energy, the internal energy, and the energy in the radiation field rise to the order of 10^{53} erg, a detailed analysis of global energy conservation is required in order to make the comparatively small explosion energy of 10^{51} erg predictable.

The following transport requirements more closely resemble the astrophysical applications of *photon transport* than neutron transport. Owing to the protoneutron star or black hole formed at the center of the event, space-time is considerably curved. The particles need to be propagated on geodesics in general relativistic space-time. The particles are subject to a gravitational frequency shift. Moreover, their angular distribution (and with it the path along which the particles are subject to absorption) is affected by gravitational light bending. In contrast to many neutron transport applications, the fluid is highly dynamic during collapse and even more so after shock formation. This requires a careful implementation of observer corrections (Doppler shift and angular aberration) as in photon transport applications. However, there is some freedom in the choice of where to implement these corrections. For example, the transport equation can be written in the lab frame and these corrections applied to the source, or the transport equation can be written in a frame comoving with the fluid and these corrections applied to the transport terms. The former results in simple transport terms and complicated source terms, the latter in complicated transport terms but much simpler source terms.

We proceed with the latter choice and an S_N -method because it offers advantages in the implicit finite difference representation of the transport equations (Mezzacappa & Bruenn 1993a). First, a smooth transition from neutrino opaque to neutrino transparent regimes is desired. An implicit scheme can at once handle the transport at lower densities, where e.g. neutrinos with a total energy of 10^{53} erg flow through matter, as well as determine and maintain an equilibrium in higher density regions where the short mean free path leads to neutrino thermalization on a much smaller time scale than the desired code time step, analogously to the instantaneous equilibrium assumed for the reactions in the equation of state. Second, the neutrinos are never completely trapped and a stationary neutrino flux may become established when the neutrinos diffuse out of the high density regions on a diffusion time scale. Implicit finite differencing in the transport equation assures the convergence to this stationary state in the limit of large time steps. We call a time step large if it reflects the neutrino diffusion time scale instead of the free propagation time scale determined by the quotient of a zone width and the speed of light.

Our code, AGILE-BOLTZTRAN, emerged from the following components: The neutrino transport part, BOLTZTRAN, has been developed for the simulation of stellar core collapse in an $O(v/c)$

approximation (Mezzacappa & Bruenn 1993a,b,c). It has been compared to MGFLD in stationary state studies and tested with standard test problems for radiative transfer in supernovae (Messer et al. 1998; Messer 2000). AGILE is an implicit general relativistic hydrodynamics code that accurately evolves the Einstein equations with its conservative finite differencing and flexible adaptive grid as documented in (Liebendörfer, Rosswog & Thielemann 2002). In this paper, we detail the intricate finite difference representation of the observer corrections for the dynamic conservation of particle number and total energy in the transport scheme, and document the extension of BOLTZTRAN to general relativistic flows as in (Liebendörfer 2000). The operator split coupling to the hydrodynamics in AGILE is also described. With this, we hope to add to the reproduceability of our physical results (Mezzacappa et al. 2001; Liebendörfer et al. 2001) as well as to provide, together with independent efforts (Rampp & Janka 2000, 2002), a solid point of reference for future, multi-dimensional supernova models.

We describe our physical model for neutrino transport in spherical symmetry in section 2. The computer representation of the model is constructed in section 3. In section 4, we discuss aspects of our simulations in the postbounce evolution of a $13 M_{\odot}$ and a $40 M_{\odot}$ progenitor star. Based on these simulations, we analyze and verify the performance of our code in various example situations in section 5. The section closes with a comparison to simulations obtained with a code using the multi-group flux-limited diffusion approximation (Bruenn et al. 2002).

2. Physical model

2.1. Equation of state and weak interactions

The micro-physics describing the interaction between the components of the fluid and the transported particles is split into the following two parts:

The equation of state describes the thermodynamical state of a fluid element based on density, ρ , temperature, T , and the composition. We use in our code the equation of state of (Lattimer & Swesty 1991): In the density range from nuclear densities down to 10^7 g/cm^3 , matter is in nuclear statistical equilibrium if the temperature exceeds $5 \times 10^9 \text{ K}$. This region is described by a liquid drop model for a representative nucleus with atomic number A and charge Z , surrounded by free alpha particles, protons, and neutrons. These baryons are immersed in an electron- and positron gas that equilibrates with a photon gas by the pair creation process. At higher than nuclear density, where no isolated nuclei are present, the by far more complicated population of hadrons (Glendenning 1985; Pons et al. 1999) is approximated by bulk nuclear matter based on protons, neutrons, and electrons. At the low temperature border of nuclear statistical equilibrium, the equation of state is connected to a Boltzmann gas of silicon atoms. In any of these cases, once the density and temperature are given, the composition is fully determined by the specification of the electron fraction Y_e .

A second microphysical ingredient are the interactions of the three neutrino flavors with the fluid element. The neutrino distribution functions evolve dynamically according to the Boltzmann transport equation. The weak interactions enter the collision term on the right hand side of the Boltzmann equation and appear as emissivities, opacities, and scattering kernels. We include the selection of reactions defined in (Bruenn 1985): (i) electron-type neutrino absorption on neutrons, (ii) electron antineutrino absorption on protons, (iii) electron-type neutrino absorption on nuclei, (iv) neutrino-nucleon scattering, (v) coherent scattering of neutrinos on nuclei, (vi) neutrino-electron scattering, (vii) neutrino production from electron/positron pair annihilation. These reactions, and their inverses, are implemented in our code as described in (Mezzacappa & Bruenn 1993b,c; Messer 2000).

The reactions collected in the equation of state are assumed to occur on very small time scales such that a description in terms of an instantaneous equilibrium is appropriate. This is also true in extreme conditions for the weak interactions between the neutrinos and the fluid. Unlike the equilibrium with respect to the strong interaction, however, the latter equilibrium is found within our solution of the transport equation. In the protoneutron star, at densities above 10^{12} g cm $^{-3}$ and temperatures above 5×10^{10} K, the neutrinos are trapped and well described by a Fermi-gas in thermal equilibrium with the fluid. However, the thermalization time scale becomes longer at lower densities and the neutrinos may propagate with a nonequilibrium spectrum throughout these regions and occasionally be absorbed or leave the star.

The above-mentioned emissivities, absorptivities, and scattering kernels strongly depend on the neutrino energies and, in the latter case, on the neutrino propagation directions. The numerical evaluation of the detailed collision term in the Boltzmann equation easily becomes a nonnegligible part of the overall computational effort. Moreover, an implicit finite differencing of the Boltzmann equation additionally requires the availability of the derivatives of all reaction rates with respect to changes in the physical state, i.e. in density, temperature, and electron fraction. In (Mezzacappa & Bruenn 1993a), a storage scheme was developed that allows the reuse of previously calculated emissivities, absorptivities, and scattering kernels by linear interpolation within a dynamical table in the independent logarithmic variables of density, ρ , temperature, T , and electron fraction, Y_e . If one uses these same independent variables in the implicit formulation of the Boltzmann equation, the correct partial derivatives of the reactions directly emerge from the coefficients of the linear interpolation, without causing additional computational effort. On average, the evaluation of the collision term is only necessary for the update of the interpolation coefficients in about two zones per time step (out of hundred zones).

However, the direct reuse is only possible if the reactions are described in a frame whose velocity with respect to the fluid is constant, for example the rest frame of the fluid element. It is therefore natural to refer the momentum components to a comoving (Lagrangian) frame. No doubt that this choice of basis is advantageous for the implementation of the collision term, but on the other hand, it raises the complexity of the left hand side of the Boltzmann equation describing the transport between non-inertial fluid elements. A consistent finite differencing of the Doppler shift,

redshift, and angular aberration in the microscopic Boltzmann equation for fermion transport will be given in section 3.

2.2. Radiation hydrodynamics in spherical symmetry

We first summarize the basic physical equations for radiation hydrodynamics in spherical symmetry in terms of momentum phase space integrated transport quantities. They form a set of hydrodynamics equations with energy flux. In a second step we detail the transport with a microscopic Boltzmann equation and show that it reduces in its momentum integration to the equations found in the first step. Finally we emphasize the conservation laws that we have to respect in the finite difference representation of the Boltzmann equation. As motivated in the previous subsection, we investigate the dynamics in comoving coordinates.

Many spherically symmetric simulations of compact objects were based on the comoving orthogonal coordinates of Misner & Sharp (1964). Finite difference schemes were constructed (May & White 1967; Van Riper 1979; Bruenn 1985; Rezzolla & Miller 1994; Swesty 1995; Liebendörfer, Rosswog & Thielemann 2002), culminating in an approximate Riemann solver (Yamada 1997). The left-hand side of the Einstein field equation, the Einstein tensor, is constructed from the metric

$$ds^2 = -\alpha^2 dt^2 + \left(\frac{r'}{\Gamma}\right)^2 da^2 + r^2 (d\vartheta^2 + \sin^2 \vartheta d\varphi^2), \quad (1)$$

where r is the areal radius and a is a label corresponding to an enclosed rest mass (the prime denotes a derivative with respect to a : $r' = \partial r / \partial a$). The proper time lapse of a comoving observer is related to the coordinate time dt by the lapse function α . The angles ϑ and φ describe a two-sphere. We use natural units such that the velocity of light, c , and the gravitational constant, G , become 1.

The right-hand side of the Einstein equations is given by the fluid- and radiation stress-energy tensor, T , which, in a comoving orthonormal basis, has the components (Lindquist 1966)

$$\begin{aligned} T^{tt} &= \rho(1 + e + J) \\ T^{ta} = T^{at} &= H \\ T^{aa} &= p + \rho K \\ T^{\vartheta\vartheta} = T^{\varphi\varphi} &= p + \frac{1}{2}\rho(J - K). \end{aligned} \quad (2)$$

The total energy is expressed in terms of the rest mass density, ρ , the specific internal fluid energy, e , and the specific radiation energy, J . The isotropic fluid pressure is denoted by p , and the radiation pressure is composed from the zeroth (J) and second (K) angular moment of the radiation intensity. Radial net energy transport is accounted for by the nondiagonal component of the stress-energy tensor, the first angular moment (H) of the radiation intensity.

We define a velocity u , equivalent to the r component of the fluid four-velocity as observed from a frame at constant areal radius r (May & White 1967), and identify the total energy enclosed in a sphere with the gravitational mass, m . In the special relativistic limit, $\Gamma = \sqrt{1 + u^2 - 2m/r}$ becomes the Lorentz factor corresponding to the boost between the inertial and the comoving observers. As in nonrelativistic hydrodynamics we can define a specific volume, $1/D$, specific energy, τ , and specific radial momentum, S , by

$$\frac{1}{D} = \frac{\Gamma}{\rho} \quad (3)$$

$$\tau = \Gamma(e + J) + \frac{2}{\Gamma + 1} \left(\frac{1}{2} u^2 - \frac{m}{r} \right) + uH \quad (4)$$

$$S = u(1 + e + J) + \Gamma H, \quad (5)$$

and find conservation equations (6)-(8) analogous to the continuity equation, the conservation of total energy, and the conservation of radial momentum (Liebendörfer, Mezzacappa, & Thielemann 2001)⁶,

$$\frac{\partial}{\partial t} \left[\frac{1}{D} \right] = \frac{\partial}{\partial a} [4\pi r^2 \alpha u] \quad (6)$$

$$\frac{\partial \tau}{\partial t} = -\frac{\partial}{\partial a} [4\pi r^2 \alpha (up + u\rho K + \Gamma \rho H)] \quad (7)$$

$$\begin{aligned} \frac{\partial S}{\partial t} &= -\frac{\partial}{\partial a} [4\pi r^2 \alpha (\Gamma p + \Gamma \rho K + u\rho H)] \\ &\quad - \frac{\alpha}{r} \left[\left(1 + e + \frac{3p}{\rho} + J + 3K \right) \frac{m}{r} - \left(1 - \frac{2m}{r} \right) (J - 3K) \right. \\ &\quad \left. + 8\pi r^2 ((1 + e + J) (p + \rho K) - \rho H^2) - 2 \left(\frac{p}{\rho} + K \right) \right] \end{aligned} \quad (8)$$

$$\frac{\partial V}{\partial a} = \frac{1}{D} \quad (9)$$

$$\frac{\partial m}{\partial a} = 1 + \tau \quad (10)$$

$$\frac{\partial}{\partial t} \left[\frac{1}{4\pi r^2 \rho} H \right] = -(1 + e + J) \frac{\partial \alpha}{\partial a} - \frac{1}{\rho} \frac{\partial}{\partial a} [\alpha (p + \rho K)] + \frac{\alpha}{3VD} (J - 3K). \quad (11)$$

The change of the specific volume in Eq. (6) is given by the balance in the displacement of the zone boundaries. The rate of change of total energy in Eq. (7) is determined by the surface luminosity, $L = 4\pi r^2 \rho H$, and rate of surface work, involving pressure, $p + \rho K$, and velocity, u .

⁶The latter reference assumed an isotropic radiation pressure. We however note that the nonisotropic stress-energy tensor (2) can easily be composed by the substitution of a pressure $\tilde{p} = p + \rho J/3$ and an artificial viscosity $\tilde{Q} = -\rho(J/3 - K)$ in (Liebendörfer, Mezzacappa, & Thielemann 2001). The same substitution made in all equations leads to the correct split of fluid and radiation energy even in the unequilibrated case of large radiation energies with $J \not\simeq 3K$.

The momentum equation (8) basically contains a pressure gradient and the gravitational force, m/r^2 . The constraints (9) and (10) explain themselves in analogy to the Newtonian limit, where the first becomes the definition of the rest mass density and the second the Poisson equation for the gravitational potential. We may define an enclosed volume by $V = 4\pi r^3/3$. The time derivative in equation (11) usually is very small, so that this equation rather acts as a constraint on the lapse function α . This equation was derived from the space-space component of the four-divergence of the stress-energy tensor. We will also need an equation for the evolution of the internal energy as derived from the time-time component of the four-divergence of the stress-energy tensor,

$$\frac{\partial}{\partial t} [e + J] = -\frac{1}{\alpha} [4\pi r^2 \alpha^2 \rho H] - (p + \rho K) \frac{\partial}{\partial} \left(\frac{1}{\rho} \right) - \frac{\alpha u}{r} (J - 3K). \quad (12)$$

We now identify the energy flux ρH with a particle flux obeying the Boltzmann transport equation. The latter is usually split into a left-hand side and a right-hand side. The left-hand side is the directional derivative of the particle distribution function along trajectories of free particle propagation. This derivative is equated to the changes in the distribution function due to collisions as described by the right hand side. After the choices of a 3+1 decomposition (Arnowitt, Deser & Misner 1962; Smarr & York 1978) and a basis in the momentum phase space have been made, the directional derivative along the phase flow can be expressed in terms of partial derivatives of the distribution function with respect to the coordinates and momenta (Mezzacappa & Matzner 1989). The general relativistic Boltzmann equation in comoving coordinates has been derived in (Lindquist 1966). We measure the particle four-momentum in a comoving orthonormal frame with the components

$$p^a = p \cos \theta, \quad p^\theta = p \sin \theta \cos \phi, \quad p^\varphi = p \sin \theta \sin \phi. \quad (13)$$

In spherical symmetry, we obtain a complete description of the particle phase space by the particle energy, E , measured in a comoving frame and the direction of the particle three momentum angle cosine $\mu = \cos \theta$ to the radial direction. We assume massless neutrinos. In spherical symmetry, the distribution function does not depend on the azimuth angle ϕ . Thus, the specific particle distribution function depends on four arguments

$$dN = F(t, a, \mu, E) E^2 dE d\mu da. \quad (14)$$

The Boltzmann equation for the metric (1) then reads (Yamada, Janka, & Suzuki 1999; Liebendörfer, Mezzacappa, & Thielemann 2001)

$$C_t + D_a + D_\mu + D_E + O_\mu + O_E = C_c, \quad \text{with} \quad (15)$$

$$C_t = \frac{\partial F}{\alpha \partial t} \quad (16)$$

$$D_a = \frac{\mu}{\alpha} \frac{\partial}{\partial a} [4\pi r^2 \alpha \rho F] \quad (17)$$

$$D_\mu = \Gamma \left(\frac{1}{r} - \frac{1}{\alpha} \frac{\partial \alpha}{\partial r} \right) \frac{\partial}{\partial \mu} [(1 - \mu^2) F] \quad (18)$$

$$D_E = -\mu\Gamma \frac{1}{\alpha} \frac{\partial\alpha}{\partial r} \frac{1}{E^2} \frac{\partial}{\partial E} [E^3 F] \quad (19)$$

$$O_E = \left(\mu^2 \left(\frac{\partial \ln \rho}{\partial t} + \frac{3u}{r} \right) - \frac{u}{r} \right) \frac{1}{E^2} \frac{\partial}{\partial E} [E^3 F] \quad (20)$$

$$O_\mu = \left(\frac{\partial \ln \rho}{\partial t} + \frac{3u}{r} \right) \frac{\partial}{\partial \mu} [\mu (1 - \mu^2) F] \quad (21)$$

$$C_c = \frac{j}{\rho} - \chi F. \quad (22)$$

The first term on the left hand side of the equation, C_t , is the temporal change of the particle distribution function. The source on the right-hand side, C_c , is the collision term that describes changes in the particle distribution function due to local interactions with matter. It is represented here by an emissivity j and an absorptivity χ . The second term, D_a , counts the particles that are propagating into or out of an infinitesimal mass shell. The third term, D_μ , accounts for the change in the neutrino distribution function in an angle interval owing to the propagation of the neutrinos along geodesics with changing local angle cosine μ . The curved particle trajectory in general relativity is accounted for by the term proportional to the gradient of the gravitational potential, Φ ,

$$\frac{1}{\alpha} \frac{\partial\alpha}{\partial r} = \frac{\partial\Phi}{\partial r}.$$

The fourth term, D_E , realizes the redshift or blueshift of the particle energy that applies when the particles have a velocity component in the radial direction ($\mu \neq 0$) and therefore change their position in the gravitational potential. The fifth term, O_E , accounts for the Doppler shift between adjacent comoving observers. The sixth term, O_μ , stands for angular aberration: When the comoving observers change radius, the corresponding relabeling of particle propagation angles also adds a correction to the in-out flow balance for the particle distribution function within a constant angle interval at central angle μ .

The integration of the Boltzmann equation over momentum space, spanned by the propagation angle and particle energy, is supposed to reproduce the conservation laws for particle number and energy as stated in Eqs. (6) and (7). We define J^N and H^N to represent the zeroth and first μ moments of the distribution function:

$$\begin{aligned} J^N &= \int_{-1}^1 \int_0^\infty F E^2 dE d\mu, \\ H^N &= \int_{-1}^1 \int_0^\infty F E^2 dE \mu d\mu. \end{aligned}$$

Integration of Eq. (15) over momentum space gives the following evolution equation in terms of these moments:

$$\frac{\partial J^N}{\partial t} + \frac{\partial}{\partial a} [4\pi r^2 \alpha \rho H^N] - \alpha \int \frac{j}{\rho} E^2 dE d\mu + \alpha \int \chi F E^2 dE d\mu = 0. \quad (23)$$

The aberration and frequency shift terms do not contribute because $(1 - \mu^2)$ vanishes at $\mu = \pm 1$ and $E^3 F$ is zero for $E = 0$ as well as for $E = \infty$. The nature of Eq. (23) is a continuity equation

analogous to Eq. (6), extended by source and absorption terms for the radiation particles. One more integration over the rest mass a from the center of the star to its surface finally gives an equation for the total radiation particle number variation as a function of integrated emission and absorption.

Slightly less straightforward is the reproduction of the energy conservation. Defining the energy moments as

$$\begin{aligned} J &= \int FE^3 dEd\mu \\ H &= \int FE^3 dE\mu d\mu \\ K &= \int FE^3 dE\mu^2 d\mu \\ Q &= \int FE^3 dE\mu^3 d\mu, \end{aligned}$$

and evaluating the evolution of the radiation energy as measured by an observer at infinity,

$$\frac{\partial}{\partial t} \int (\Gamma + u\mu) FE^3 dEd\mu, \quad (24)$$

where the evolution of the particle distribution function is given by Eq. (15), one obtains the concise result (Liebendörfer, Mezzacappa, & Thielemann 2001)

$$\begin{aligned} 0 &= \frac{\partial}{\partial t} (\Gamma J + uH) + \frac{\partial}{\partial a} [4\pi r^2 \alpha \rho (uK + \Gamma H)] + 4\pi r \alpha \rho \left(1 + e + \frac{p}{\rho}\right) H \\ &\quad - \alpha \Gamma \int \left(\frac{j}{\rho} - \chi\right) E^3 dEd\mu + \alpha u \int \chi FE^3 dE\mu d\mu. \end{aligned} \quad (25)$$

The time derivative contains the conserved energy; the second term describes the change of energy in the fluid element due to surface work by the radiation pressure, ρK , and in-out flow of radiation at luminosity $L = 4\pi r^2 \rho H$. The third term contains a gravitational coupling between the matter enthalpy and the luminosity that we neglected in previous work. The source terms in Eq. (25) describe the energy exchange with matter by particle emission, absorption, and work due to particle stress. These energy terms are absorbed by the fluid. By the comparison of Eq. (25) to Eq. (7) it becomes apparent, which part of the total energy evolution is covered by the Boltzmann equation (15) and which part of the evolution is left for the hydrodynamics. This separation also applies to the momentum equation, the lapse function equation, and the internal energy equation. With the help of relations derived in (Liebendörfer, Mezzacappa, & Thielemann 2001), we find the following combinations of moments of the Boltzmann equation that describe the radiation part in Eq. (8), Eq. (11), and Eq. (12):

$$\begin{aligned} \frac{\partial}{\partial t} [uJ + \Gamma H] &= -\frac{\partial}{\partial a} [4\pi r^2 \alpha \rho (\Gamma K + uH)] \\ &\quad - \frac{\alpha}{r} \left[(J + 3K) \frac{m}{r} - \left(1 - \frac{2m}{r}\right) (J - 3K) - 2K \right] \end{aligned}$$

$$\begin{aligned}
 & + 4\pi r^2 (J(p + \rho K) + (1 + e + J)\rho K - 2\rho H^2) \\
 & - \alpha \Gamma \int \chi F E^3 dE \mu d\mu + \alpha u \int \left(\frac{j}{\rho} - \chi F \right) E^3 dE \mu d\mu
 \end{aligned} \tag{26}$$

$$\begin{aligned}
 \frac{\partial}{\partial t} \left[\frac{1}{4\pi r^2 \rho} H \right] & = -J \frac{\partial \alpha}{\partial a} - \frac{1}{\rho} \frac{\partial}{\partial a} [\alpha \rho K] + \frac{\alpha}{3VD} (J - 3K) \\
 & - \frac{1}{4\pi r^2 \rho} \int \chi F E^3 dE \mu d\mu
 \end{aligned} \tag{27}$$

$$\begin{aligned}
 \frac{\partial J}{\partial t} & = -\frac{1}{\alpha} [4\pi r^2 \alpha^2 \rho H] - \rho K \frac{\partial}{\partial t} \left(\frac{1}{\rho} \right) - \frac{\alpha u}{r} (J - 3K) \\
 & + \alpha \int \left(\frac{j}{\rho} - \chi F \right) E^3 dE \mu d\mu.
 \end{aligned} \tag{28}$$

After having numerically solved the Boltzmann equation for a finite time step, we will subtract the contributions (26)-(28) from the total evolution equations (8), (11), and (12) to determine the remaining updates left for the hydrodynamical time step. First, however, we proceed with the description of the numerical implementation of the Boltzmann equation.

3. Towards a conservative computer representation

In the introduction, we motivated the conservation of particle number and total energy in the treatment of radiation transport for supernova simulations. In a macroscopic description of the dynamics, as e.g. in hydrodynamics, each conservation law can be enforced by an individual evolution equation. Instead of determining the orbits of single particles, one solves a continuity-, energy-, and momentum equation separately for fluid elements that contain the particles in a state of thermodynamic equilibrium. This separation is helpful in the implementation of a finite difference representation of hydrodynamics equations since each equation can be arranged to ensure exactly one conservation law.

Very different are things on a single particle level. *One* kinetic equation (15) determines the complete dynamics in the phase space of the particles. Its integration over the momentum phase space is equivalent to a continuity equation (23), its integration weighed with particle energies, ε , is equivalent to an energy equation (25), and its integration weighed with the particle direction cosine and energy would lead to a momentum equation. These derived equations certainly fulfill the macroscopic conservation laws, as e.g. shown in Eq. (7). But it is a challenge to obtain the same level of consistency in a finite difference representation of the Boltzmann equation. One could solve separate microscopic equations, one describing microscopic particle flows, the other describing microscopic energy flows as in the hydrodynamical limit (see e.g. (Rampp & Janka 2002)). However, since the computational effort to solve a full kinetic equation is large, this is generally not the most efficient way to guarantee the required conservation laws. Hence, we are looking for a finite difference representation of *one* kinetic equation that obeys *two* macroscopic conservation laws, for both particle number and energy.

3.1. Conservation laws and an error matching technique

In the hope to obtain hints for the construction of a conservative finite difference representation of Eq. (15), we first analyze the synthesis of the conservation equations in the continuum world, where insight is not buried behind discretization indices. The emergence of lepton number conservation in Eq. (23) is straightforward, because the observer corrections are already written in a form that allows an immediate integration over energy or the angle cosine. Number conservation will also emerge naturally in the finite difference representation when we keep this basic structure. With the energy moments however, the particle energy E gets multiplied into the term O_E , and an angle cosine μ from $(\Gamma + u\mu)$ gets multiplied into the term O_μ . In both cases, an integration by parts with vanishing boundary conditions leads to terms that contribute to the global energy conservation. This integration by parts has to be exactly reproduced in the finite difference equations: Cancellations between the various terms in the synthesis of the energy conservation have to be exact in the finite difference representation as well. We try to identify these cancellations between terms by evaluating the energy conservation law as seen from an inertial observer at infinity,

$$\int (\Gamma + u\mu) [C_t + D_a + D_\mu + D_E + O_E + O_\mu - C_c] E^3 dE d\mu = 0. \quad (29)$$

All terms stemming from the Boltzmann equation (15) are written as the derivative of an expression with respect to time, rest mass, angle cosine, or particle energy, as it is convenient for the demonstration of number conservation. We obtain the energy conservation equation after an integration by parts with respect to all of these integration variables x . A multitude of correction terms proportional to $\partial(\Gamma + u\mu) E / \partial x$ arise. They are subject to mutual cancellation because $(\Gamma + u\mu) E$ is nearly a constant of motion along the phase flow. The contribution to Eq. (29) from each term after the integration by parts is listed in the following table:

$$\begin{aligned} C_t : & \frac{\partial}{\partial t} (\Gamma J) - \frac{\partial \Gamma}{\partial t} J + \frac{\partial}{\partial t} (uH) - \frac{\partial u}{\partial t} H \\ D_a : & \frac{\partial}{\partial a} [4\pi r^2 \alpha \rho \Gamma H] - 4\pi r^2 \rho \frac{\partial \Gamma}{\partial a} H \\ & + \frac{\partial}{\partial a} [4\pi r^2 \alpha \rho u K] - 4\pi r^2 \rho \frac{\partial u}{\partial a} K \\ D_\mu : & -\Gamma \frac{u}{r} (J - K) + \Gamma u \frac{\partial \Phi}{\partial r} (J - K) \\ D_E : & \Gamma \frac{\partial \Phi}{\partial r} (\Gamma H + uK) \\ O_E : & - \left[\frac{\partial \ln \rho}{\partial t} + \frac{2u}{r} \right] (\Gamma K + uQ) + \Gamma \frac{u}{r} (J - K) + \frac{u^2}{r} (H - Q) \\ O_\mu : & - \left[\frac{\partial \ln \rho}{\partial t} + \frac{2u}{r} \right] u (H - Q) - \frac{u^2}{r} (H - Q) \\ C_c : & \Gamma \int \left(\frac{j}{\rho} - \chi F \right) E^3 dE d\mu - u \int \chi F E^3 dE \mu d\mu. \end{aligned} \quad (30)$$

For the following analysis of cancellations we neglect terms that are nonlinear in the radiation field, i.e. terms that describe a gravitational interaction of the radiation field with itself. From the hydrodynamics equations in (Misner & Sharp 1964) we then derive the following useful relationships for the coefficients in Eq. (30).

$$\frac{1}{\Gamma} \frac{\partial \Gamma}{\alpha \partial t} = u \frac{\partial \Phi}{\partial r} \quad (31)$$

$$- \left(\frac{\partial \ln \rho}{\alpha \partial t} + \frac{2u}{r} \right) = \frac{4\pi r^2 \rho}{\Gamma} \frac{\partial u}{\partial a} \quad (32)$$

$$\frac{\partial u}{\alpha \partial t} = \Gamma^2 \frac{\partial \Phi}{\partial r} - \frac{m}{r^2} - 4\pi r p. \quad (33)$$

We may now identify cancellations in Eq. (30) and label them for later reference: The fourth term of D_a cancels with the first term of O_E ($D_a^4 O_E^1$) by Eq. (32). The first and second term of D_μ cancel with the third and fourth term in O_E ($D_\mu^{12} O_E^{34}$). These are the only $O(v/c)$ cancellations and therefore the most important ones. In an analogous notation, we find the following higher order cancellations: ($C_t^2 D_\mu^3$) by Eq. (31), ($D_\mu^4 D_E^2$), ($O_E^2 O_\mu^2$), ($O_E^{56} O_\mu^{34}$). The remaining terms, ($C_t^4 D_a^2 D_E^1 O_\mu^1$), reduce by Eq. (33) and the definition of Γ to the general relativistic term,

$$\left(-\frac{\partial u}{\alpha \partial t} - \Gamma \frac{\partial \Gamma}{\partial r} + \Gamma^2 \frac{\partial \Phi}{\partial r} + u \frac{\partial u}{\partial r} \right) H = 4\pi r \rho (1 + e + p/\rho) H \quad (34)$$

and enter in this form the radiation energy conservation equation (25).

We will adopt the following strategy in the finite differencing of Eq. (15) (the reader is invited to draw lines in Eq. (30) to visualize the relationship between the different terms): (i) The finite differencing of C_t and C_c are straightforward. (ii) Appreciable experience has been gathered in previous work (see e.g. (Lewis & Miller 1993)) with the finite differencing of the $O(v/c)$ terms in D_a and D_μ . They are assumed to be well-chosen in (Mezzacappa & Bruenn 1993a) and therefore not subject to changes. (iii) Based on this, the cancellation ($D_a^4 O_E^1$) dictates the finite difference representation of $(\partial \ln \rho / \alpha \partial t + 2u/r)$ in O_E^1 and O_E^2 . The cancellation ($O_E^2 O_\mu^2$) sets the finite difference representation of $(\partial \ln \rho / \alpha \partial t + 2u/r)$ in O_μ^2 and O_μ^1 . (iv) The cancellation ($D_\mu^{12} O_E^{34}$) dictates the finite difference representation of u/r in O_E^{34} and O_E^{56} . The cancellation ($O_E^{56} O_\mu^{34}$) propagates the finite difference representation to u/r in O_μ^{34} . (v) The evaluation of ($C_t^4 D_a^2 D_E^1 O_\mu^1$) according to Eq. (34) constrains the finite difference representation of $\Gamma \partial \Phi / \partial r$ in D_E^1 and therewith defines D_E^2 . (vi) And finally we choose a different finite difference representation for $\Gamma u \partial \Phi / \partial r$ in D_μ^3 and D_μ^4 , as suggested by the cancellation ($C_t^2 D_\mu^{34} D_E^2$). By these six chains, all terms in Eq. (15) become constrained.

3.2. Finite difference representation of the transport equation

As the reader will shortly notice: Our finite difference representation of the Boltzmann equation is quite complex and, at least in the beginning, difficult to overview. We try to compensate for this

situation with a well-structured organization of the description in the sense that a less involved reader can safely decide where to skip. A rigorous reader, on the other hand, should be able to find any discretization detail required to reproduce the simulations. We start with a description of the primitive variables that are evolved in our scheme. Their discretization in space is given along with the discretization in the momentum space for the particle distribution function. The finite difference representation of the Boltzmann equation (15) is then composed out of its constituting terms listed in Eqs. (16)-(22). Each term will be described in a separate subsection. We try to provide the idea behind the chosen finite difference representation, the detailed description of the chosen finite difference representation, and the evaluation of the consequences of the chosen finite difference representation for the discretization of other dependent terms that are linked by the requirement of mutual cancellation according to the discussion of Eq. (30). Finally we gather these terms in section 3.4 and describe how their evaluation is staggered in time and how the kinetic equation for radiative transfer is linked to the evaluation of the hydrodynamical evolution.

Knowledge of a complete set of primitive variables at a certain time instance allows the derivation of all other quantities of interest. Our choice of primitive variables is listed in table (1). The discretization in space is indicated by the index i . We adopt the convention that integer values of i point to zone edges while $i + 1/2$ refers to the zone mass-center between edge i and $i + 1$. We abbreviate $i + 1/2 = i'$ with a prime in order to not further challenge the readability of the finite difference equations with half-valued indices. We use in our calculations of order 100 spatial zones on a dynamically adaptive grid. The particle distribution functions, $F_{i',j',k'}$, additionally depend on the particle momentum phase space, i.e. the angle cosine of the particle propagation direction, μ , and the particle energy, E . In our scheme, both are measured in a comoving frame and discretized with zone center values $\mu_{j'}$ and $E_{k'}$ in compliance with the above-mentioned conventions. We use Gaussian quadrature in the angles $\mu_{j'}$ with weights $w_{j'}$ derived from Legendre polynomials in order to guarantee the integral $\int \mu d\mu = \sum \mu_{j'} w_{j'} = 2$. The range from inwards to outwards propagation is currently resolved with 6 different propagation angles, but we are free to choose a larger number of directions for higher resolution studies. The energy grid is set by geometrically increasing zone edge values E_k . Following a suggestion of Bruenn, the zone center energies are defined by

$$E_{k'} = \sqrt{\frac{E_{k+1}^2 + E_{k+1}E_k + E_k^2}{3}}.$$

This choice implements the phase space volume $E_{k'}^2 dE_{k'} = E_{k+1}^3 - E_k^3$ in an exact manner. We currently use 12 zone center energies ranging from 3 MeV to 300 MeV, but this number can also be increased for higher resolution studies. Note that the zone centered energies also form a geometric series. Thermodynamical and compositional quantities are obtained from the primitive variables by the equation of state. Properties of the particle radiation field are obtained by the evaluation of the expectation value of the corresponding particle property with the primitive particle distribution function.

3.2.1. Time derivative of the particle distribution function

The finite differencing of the time derivative of the particle distribution function, Eq. (16), is straightforward. It is implemented in the following way:

$$C_t = \frac{F_{i',j',k'} - \overline{F}_{i',j',k'} \frac{da_{i'}}{da_{i'}}}{\alpha_{i'} dt} + \frac{1}{\alpha_{i'} da_{i'}} \left[u_{i+1}^{\text{rel}} F_{i+1,j',k'}^* - u_i^{\text{rel}} F_{i,j',k'}^* \right]. \quad (35)$$

The quantities with an overbar refer to the previous value of the variables, all other quantities refer to the updated values after the time step $dt = t - \bar{t}$. We have included the corrections stemming from the adaptive gridding as discussed in appendix B. We also define the advected particle distribution function $F_{i,j',k'}^*$ in that context in Eq. (B8). On a Lagrangian grid, where the mass in a spherical shell $da_{i'} = a_{i+1} - a_i$ stays constant and the relative velocity (in mass) between the matter and the grid $u_i^{\text{rel}} = -(a_i - \bar{a}_i)/dt$ vanishes, the expression reduces simply to $C_t = (F_{i',j',k'} - \overline{F}_{i',j',k'}) / (\alpha_{i'} dt)$.

3.2.2. Collision term

The finite difference representation of the collision term, Eq. (22), with the above-listed reactions is described in detail in (Mezzacappa & Bruenn 1993b,c; Messer 2000). We represent it here with a simple placeholder, namely emissivity $j_{i',k'}$ and absorptivity $\chi_{i',k'}$ as a function of the thermodynamical state of the fluid,

$$C_c = \frac{j_{i',k'}(\rho_{i'}, T_{i'}^*, Y_{e,i'}^*)}{\rho_{i'}} - \chi_{i',k'}(\rho_{i'}, T_{i'}^*, Y_{e,i'}^*) F_{i',j',k'}. \quad (36)$$

The quantities designated with a star subscript refer to partially updated quantities between the operator split transport and hydrodynamics time step as defined in section 3.4, where we outline the temporal sequence of the evaluation of equations.

	primitive variable		primitive variable
a_i	enclosed rest mass	$\rho_{i'}$	rest mass density
r_i	radius	$T_{i'}$	temperature
u_i	velocity	$Y_{e,i'}$	electron fraction
m_i	enclosed gravitational mass	$\alpha_{i'}$	lapse function
		$F_{i',j',k'}$	neutrino distribution function

Table 1: The primitive variables are listed with an index i if they live on zone edges and an index i' if they live on zone centers. The momentum phase space for the neutrino distribution function is labelled with an index j' for the angle cosine of the propagation direction and an index k' for the neutrino energy.

3.2.3. Particle propagation in space

The term D_a in Eq. (17) accounts for the particles that are propagating into and out of a spherical mass shell. From first considerations it is evident that this term has to be proportional to the dot product between the particle propagation direction and the shell boundary, i.e. the angle cosine μ . By this property, the contribution becomes proportional to the gradient of the first angular moment of the particle distribution function when the Boltzmann equation (15) is integrated over the propagation angles. In the free streaming limit, the advected particle number in a time step (always in the perspective of a comoving observer) is large with respect to the particle number in the zone. Upwind differencing of the advection terms is appropriate to limit destabilizing errors in the advection fluxes. For discrete angle cosines $\mu_{j'}$ the direction of the particle “wind” is simply given by the sign of $\mu_{j'}$ (A particle with $\mu = 0$ propagates tangential to the mass shell). In diffusive conditions, however, the particle flux may be by orders of magnitude smaller than the prevailing nearly isotropic particle density in the mass shell. In this situation, an asymmetric differencing that depends on the particle wind can easily lead to an overestimate of the first angular moment because of improper cancellations among the contributions of the isotropic component of the particle field. We therefore adhere to the strategy chosen in (Mezzacappa & Bruenn 1993a) and, based on transport coefficients $\beta_{i,k'}$, interpolate between upwind differencing in free streaming regimes ($\beta_{i,k'} = 1$) and centered differencing ($\beta_{i,k'} = 1/2$) in diffusive regimes. The choice of the transport coefficients in (Mezzacappa & Bruenn 1993a) has the disadvantage, that they are not perfectly one half in the diffusive regime inside the neutrino sphere. With the compactification of the proto-neutron star, the deviation of the transport coefficient from one half may exceed the decreasing ratio between the neutrino flux and the neutrino density times the velocity of light. The consequence is an artificial overestimate of diffusive neutrino fluxes because of inaccuracies in the equilibrium constraint (73) in (Mezzacappa & Bruenn 1993a) that only holds for $\beta_{i,k'} = 1/2$. We therefore use transport coefficients according to

$$\beta_{i,k'} = \begin{cases} 1/2 & \text{if } 2dr_i > \lambda_i, \\ (2dr_i/\lambda_{i,k'} + 1)^{-1} & \text{otherwise.} \end{cases} \quad (37)$$

The transport coefficients at zone edges are set to depend on the ratio between the distance dr_i between zone centers and the neutrino energy dependent mean free path $\lambda_{i,k'}$. We then discretize the propagation term as in (Mezzacappa & Bruenn 1993a):

$$D_a = \frac{\mu_{j'}}{\alpha_{i'} da_{i'}} [4\pi r_{i+1}^2 \alpha_{i+1} \rho_{i+1} F_{i+1,j',k'} - 4\pi r_i^2 \alpha_i \rho_i F_{i,j',k'}] \quad (38)$$

with

$$\alpha_i \rho_i F_{i,j',k'} = \beta_{i,j',k'} \alpha_{i'-1} \rho_{i'-1} F_{i'-1,j',k'} + (1 - \beta_{i,j',k'}) \alpha_{i'} \rho_{i'} F_{i',j',k'}$$

for outwards propagating particles ($\mu_{j'} > 0$), and

$$\alpha_i \rho_i F_{i,j',k'} = (1 - \beta_{i,j',k'}) \alpha_{i'-1} \rho_{i'-1} F_{i'-1,j',k'} + \beta_{i,j',k'} \alpha_{i'} \rho_{i'} F_{i',j',k'} \quad (39)$$

for inwards propagating particles ($\mu_{j'} < 0$).

Based on this finite difference representation, we generate the term D_a^4 in Eq. (30) that has to be matched with the observer corrections described in subsection 3.2.5 and 3.2.7. We multiply Eq. (38) with the term $u_{i+1}\mu_{j'}$ from the energy of a distant inertial observer and mimic an integration by parts over da in the finite difference representation

$$\begin{aligned} & \frac{\mu_{j'}^2}{\alpha_{i'}da_{i'}} [4\pi r_{i+1}^2 \alpha_{i+1} \rho_{i+1} u_{i+1} F_{i+1,j',k'} - 4\pi r_i^2 \alpha_i \rho_i u_{i+1} F_{i,j',k'}] \\ &= \frac{\mu_{j'}^2}{\alpha_{i'}da_{i'}} [4\pi r_{i+1}^2 \alpha_{i+1} \rho_{i+1} u_{i+1} F_{i+1,j',k'} - 4\pi r_i^2 \alpha_i \rho_i u_i F_{i,j',k'}] \\ & - \frac{4\pi r_i^2}{\alpha_{i'}} \frac{u_{i+1} - u_i}{da_{i'}} \mu_{j'}^2 \alpha_i \rho_i F_{i,j',k'}. \end{aligned}$$

The last term corresponds to D_a^4 . By insertion of the interpolation prescription of $\alpha_i \rho_i F_{i,j',k'}$ for ingoing and outgoing particles, we obtain the matched finite difference representation for $A = -4\pi r^2 \rho / \Gamma \cdot \partial u / \partial a$:

$$A_{i',k'} = \frac{4\pi \rho_{i'}}{\Gamma_{i+1} da_{i'}} (r_{i+1}^2 (u_{i+2} - u_{i+1}) (1 - \beta_{i+1,k'}) + r_i^2 (u_{i+1} - u_i) \beta_{i,k'})$$

if $\mu_{j'} \leq 0$, and

$$A_{i',k'} = \frac{4\pi \rho_{i'}}{\Gamma_{i+1} da_{i'}} (r_{i+1}^2 (u_{i+2} - u_{i+1}) \beta_{i+1,k'} + r_i^2 (u_{i+1} - u_i) (1 - \beta_{i,k'})) \quad (40)$$

if $\mu_{j'} > 0$. We may use exactly the same analysis to define a matched finite difference representation for D_a^2 , with $\Lambda = -4\pi r^2 \rho \cdot \partial \Gamma / \partial a$:

$$\Lambda_{i',k'} = \frac{4\pi \rho_{i'}}{\Gamma_{i+1} da_{i'}} (r_{i+1}^2 (\Gamma_{i+2} - \Gamma_{i+1}) (1 - \beta_{i+1,k'}) + r_i^2 (\Gamma_{i+1} - \Gamma_i) \beta_{i,k'})$$

if $\mu_{j'} \leq 0$, and

$$\Lambda_{i',k'} = \frac{4\pi \rho_{i'}}{\Gamma_{i+1} da_{i'}} (r_{i+1}^2 (\Gamma_{i+2} - \Gamma_{i+1}) \beta_{i+1,k'} + r_i^2 (\Gamma_{i+1} - \Gamma_i) (1 - \beta_{i,k'})). \quad (41)$$

3.2.4. Angular corrections from particle propagation

The angle between the particle propagation direction and the radius decreases for a free streaming particle on an outgoing trajectory. Hence, particle propagation causes angular advection in the local view of a fixed angular bin at angle cosine $\mu_{j'}$. This contribution to the temporal evolution of the particle distribution function is described in the term D_μ in Eq. (18). The finite difference representation of this geometric correction is chosen such as to maintain an equilibrium between the radiation field and stationary matter (Lewis & Miller 1993). As in (Mezzacappa & Bruenn 1993a), we set

$$D_\mu = \left(\Gamma_{i+1} \frac{3 [r_{i+1}^2 - r_i^2]}{2 [r_{i+1}^3 - r_i^3]} - G_{i+1}^\mu \right) \frac{1}{w_{j'}} (\zeta_{j+1} F_{i',j+1,k'} - \zeta_j F_{i',j,k'}). \quad (42)$$

The angular difference coefficients, $\zeta = 1 - \mu^2$, are defined by

$$\zeta_{j+1} - \zeta_j = -2\mu_{j'} w_{j'}. \quad (43)$$

The angular integration of the correction D_μ produces the zeroth and second angular moments of the particle distribution function. Its finite difference representation is therefore not as sensitive to cancellations in the diffusive limit as D_a . Upwind differencing could be justified. The angular “wind” always points towards $\mu = 1$. However, for reasons of completeness and consistency, we also use centered differencing in the diffusive regime. With angular transport coefficients $\gamma_{i',k'} := \beta_{i',k'}$, we interpolate the values of the neutrino distribution function on angular zone edges by

$$F_{i',j,k'} = \gamma_{i',k'} F_{i',j'-1,k'} + (1 - \gamma_{i',k'}) F_{i',j',k'}. \quad (44)$$

New is the gravitational term $G^\mu = \Gamma \partial \Phi / \partial r$ in Eq. (42) that is responsible for the “light bending” in the gravitational field. We determine in Eq. (48) below its finite difference representation by the match ($C_t^2 D_t^{34} D_E^2$) in the diffusive limit.

The terms D_μ^{1-4} in Eq. (30) arise from an integration by parts over angle cosines after the multiplication of the Boltzmann equation (15) with $u\mu$. We introduce the abbreviation

$$\Upsilon_{i+1} = \Gamma_{i+1} \frac{3[r_{i+1}^2 - r_i^2]}{2[r_{i+1}^3 - r_i^3]} - G_{i+1}^\mu$$

for the prefactor in Eq. (42) and mimic the integration by parts in a sum over the discrete angle cosines:

$$\begin{aligned} & \sum_{j=1,j_{\max}} u_{i+1} \Upsilon_{i+1} (\zeta_{j+1} \mu_{j'} F_{i',j+1,k'} - \zeta_j \mu_{j'} F_{i',j,k'}) \\ &= \sum_{j=1,j_{\max}} u_{i+1} \Upsilon_{i+1} (\zeta_{j+1} \mu_{j'} F_{i',j+1,k'} - \zeta_j \mu_{j'-1} F_{i',j,k'}) \\ & \quad - \sum_{j=1,j_{\max}} u_{i+1} \Upsilon_{i+1} \zeta_j F_{i',j,k'} (\mu_{j'} - \mu_{j'-1}) \\ &= - \sum_{j=1,j_{\max}} u_{i+1} \Upsilon_{i+1} F_{i',j',k'} \\ & \quad \times [\gamma_{i',k'} \zeta_{j+1} (\mu_{j'+1} - \mu_{j'}) + (1 - \gamma_{i',k'}) \zeta_j (\mu_{j'} - \mu_{j'-1})]. \end{aligned} \quad (45)$$

The expression in the second line vanishes because of mutual cancellations and $\zeta_1 = \zeta_{j_{\max}+1} = 0$. Remembering that $\zeta = 1 - \mu^2$, we can identify the result as a special finite difference representation of the terms D_μ^{12} and D_μ^{34} in Eq. (30). Following the strategy of the previous paragraph, we extract from Eq. (45) information about the constraint ($D_\mu^{12} O_E^{34}$) in order to obtain global energy conservation in the combination with the observer corrections. We prepare an expression $B = (1 - \mu^2) u/r$ by the finite difference representation

$$B_{i',j',k'} = \frac{3}{2} \frac{r_{i+1}^2 - r_i^2}{r_{i+1}^3 - r_i^3} \frac{u_{i+1}}{w_{j'}} [\gamma_{i',k'} \zeta_{j+1} (\mu_{j'+1} - \mu_{j'}) + (1 - \gamma_{i',k'}) \zeta_j (\mu_{j'} - \mu_{j'-1})] \quad (46)$$

that will be used later in the implementation of the frequency shift term O_E^{34} . The finite difference representation of G_{i+1}^μ for the gravitational “light bending” still needs to be defined. It will be based on three assumptions: (i) We assume that the hydrodynamics part accurately implements Eq. (31), i.e.

$$C_t^2 \equiv -\frac{\Gamma_{i+1} - \bar{\Gamma}_{i+1}}{\alpha_{i'} dt} J_{i'} = -u_{i+1} \frac{\Gamma_{i+1}}{\alpha_{i'}} \frac{\alpha_{i'+1} - \alpha_{i'}}{r_{i'+1} - r_{i'}} J_{i'}. \quad (47)$$

If this is not the case, an alternative discretization based on the time derivative of Γ as a function of the velocity and the gravitational potential may also provide satisfactory results (see Eq. (B9) for the evaluation of du/dt on the adaptive grid),

$$C_t^2 \equiv -\frac{\Gamma_{i+1} - \bar{\Gamma}_{i+1}}{\alpha_{i'} dt} J_{i'} = \frac{u_{i+1}}{\Gamma_{i+1}} \left(\frac{du}{\alpha_{i'} dt} + 4\pi r_{i+1} p_{i'+1} + \frac{m_{i+1}}{r_{i+1} \bar{r}_{i+1}} \right) J_{i'}.$$

(ii) We assume an isotropic distribution function for the radiation particles and obtain with $J = 3K$ from Eq. (45)

$$\begin{aligned} D_\mu^{34} &= -u_{i+1} G_{i+1}^\mu F_{i',k'} \sum_{j=1,j_{\max}} \mu_{j'} (\zeta_{j+1} - \zeta_j) \\ &= u_{i+1} G_{i+1}^\mu F_{i',k'} \sum_{j=1,j_{\max}} \mu_{j'}^2 w_{j'} \\ &= \frac{2}{3} u_{i+1} G_{i+1}^\mu J_{i'}. \end{aligned}$$

Note that the Gaussian quadrature in the angle discretization provides the exact integral for $\int \mu^2 d\mu = 2/3$. (iii) We assume that we have already determined a contribution $u_{i+1} G_{i+1}^E J_{i'}/3$ for D_E^2 that depends on a slightly different discretization of $G^E = \Gamma \partial \Phi / \partial r$ defined later in Eq. (57). Table (30) then suggests the implementation of $C_t^2 + D_\mu^{34} + D_E^2 = 0$ and we find

$$G_{i+1}^\mu = \frac{3}{2} \frac{\Gamma_{i+1}}{\alpha_{i'}} \frac{\alpha_{i'+1} - \alpha_{i'}}{r_{i'+1} - r_{i'}} - \frac{1}{2} G_{i+1}^E. \quad (48)$$

3.2.5. Frequency shift from observer motion

We continue our description with the observer correction O_E in Eq. (20). We start with a review of the finite differencing procedure presented in (Mezzacappa & Bruenn 1993a) in order to extend it from local to global energy conservation in all $O(v/c)$ terms. Furthermore, the basic argumentation can be carried over to achieve a consistent description of the gravitational frequency shift, D_E , and the angular aberration, O_μ , in subsequent paragraphs.

If the observer of the radiation field is in motion, an observer correction O_E in the transport equation (15) has to account for the observed frequency shift in the description of the radiation field with respect to neighbor observers moving with different velocities. Suggested by the nature

of the prefactors for the energy and angle moments occuring in table 30, it is convenient to write the prefactor of this correction in terms of two separate quantities, A and B , such that

$$\begin{aligned} A &= \left(\frac{\partial \ln \rho}{\alpha \partial t} + \frac{2u}{r} \right) \\ B &= (1 - \mu^2) \frac{u}{r} \\ O_E &= (\mu^2 A - B) \frac{1}{E^2} \frac{\partial}{\partial E} [E^3 F]. \end{aligned} \quad (49)$$

It has been found in (Bruenn 1985; Mezzacappa & Bruenn 1993a) that the update $C_t + O_E = 0$ has an analytical solution. One may write the prefactor of the correction as a time derivative of a quantity $R_f = r^{(3\mu^2-1)} \rho^{(\mu^2)}$,

$$\frac{\partial \ln R_f}{\alpha \partial t} = \mu^2 A - B,$$

and rewrite $0 = C_t + O_E$ as

$$0 = E^3 \left(\frac{\partial F}{\partial t} \right)_E + \alpha (\mu^2 A - B) E \frac{\partial}{\partial E} [E^3 F]. \quad (50)$$

With the notation $(\partial/\partial t)_x$ for a time derivative at constant y and the chain rule $(\partial/\partial t)_x = (\partial/\partial t)_y + (\partial y/\partial t)_x (\partial/\partial y)$ we are searching for a “Lagrangian” description of the correction in the energy dimension. The transformation from the “Eulerian” variable $x = E$ to the “Lagrangian” variable $y = E/R_f$ simplifies Eq. (50) in the following way,

$$\begin{aligned} 0 &= \left(\frac{\partial}{\partial t} [E^3 F] \right)_E + \frac{\partial R_f}{R_f^2 \partial t} E \times R_f \frac{\partial}{\partial E} [E^3 F] \\ &= \left(\frac{\partial}{\partial t} [E^3 F] \right)_E - \left(\frac{\partial [E/R_f]}{\partial t} \right)_E \frac{\partial [E^3 F]}{\partial [E/R_f]} = \left(\frac{\partial}{\partial t} [E^3 F] \right)_{E/R_f}. \end{aligned}$$

For a small section of the energy phase space $E^2 \Delta E = (E_2^3 - E_1^3)/3$, this relationship leads to

$$\left(\frac{\partial}{\partial t} [E^2 F \Delta E] \right)_{E/R_f} = 0. \quad (51)$$

The validity of Eq. (51) for arbitrary distribution functions F points to the following interpretation: The particles initially residing in the energy phase space interval $E^2 \Delta E$ are shifted by the investigated observer correction along constant E/R_f in the energy phase space of a comoving observer. This relationship is very convenient to determine the evolution of any other particle property, as for example the specific energy of the particles in this phase space interval, $d\epsilon = E^3 F \Delta E$,

$$\left(\frac{\partial}{\partial t} [E^3 F \Delta E] \right)_{E/R_f} = E^2 F \Delta E \left(\frac{\partial E}{\partial t} \right)_{E/R_f} = \frac{\partial \ln R_f}{\partial t} d\epsilon. \quad (52)$$

A finite difference representation of Eqs. (51) and (52) has been used in (Mezzacappa & Bruenn 1993a) to realize a numerical implementation of the observer correction O_E that evolves the moments of the neutrino distribution function exactly as prescribed by the coefficients A and B in the

prefactor. The strategy is outlined in the view of a specific energy group k' with a neighbor group $k' + dk$, $dk = \pm 1$. Eq. (51) tells that the number of particles before the correction, $F_{i',j',k'} E_{k'}^2 dE_{k'}$, is equal to the number of particles after the correction. The state after the correction is represented by a diminished number of particles $F_{i',j',k'} E_{k'}^2 dE_{k'} - n_{i',j',k'}^-$ in group k' and an additional number of particles $n_{i',j',k'+dk}^+$ in the neighbor group $k' + dk$,

$$F_{i',j',k'} E_{k'}^2 dE_{k'} - \left[\left(F_{i',j',k'} E_{k'}^2 dE_{k'} - n_{i',j',k'}^- \right) + n_{i',j',k'+dk}^+ \right] = 0. \quad (53)$$

Eq. (52) now defines a similar relationship for the particle energies

$$\begin{aligned} F_{i',j',k'} E_{k'}^3 dE_{k'} &= \left[\left(F_{i',j',k'} E_{k'}^3 dE_{k'} - E_{k'+dk} n_{i',j',k'+dk}^+ \right) + E_{k'+dk} n_{i',j',k'+dk}^+ \right] \\ &= -(\mu_{j'}^2 A_{i',k'} - B_{i',j',k'}) F_{i',j',k'} E_{k'}^3 dE_{k'} \alpha_{i'} dt. \end{aligned} \quad (54)$$

As in (Mezzacappa & Bruenn 1993a), Eqs. (53) and (54) uniquely define the solution

$$\begin{aligned} n_{i',j',k'}^- &= (\mu_{j'}^2 A_{i',k'} - B_{i',j',k'}) \frac{dE_{k'}}{E_{k'+dk} - E_{k'}} E_{k'}^3 F_{i',j',k'} \alpha_{i'} dt \\ n_{i',j',k'}^+ &= n_{i',j',k'-dk}^- \end{aligned} \quad (55)$$

that leads, by the update $F_{i',j',k'} = \bar{F}_{i',j',k'} + (n_{i',j',k'}^+ - n_{i',j',k'}^-) / (E_{k'}^2 dE_{k'})$, to the finite difference representation

$$\begin{aligned} O_E &= \frac{1}{E_{k'}^2 dE_{k'}} \\ &\times \left[(\mu_{j'}^2 A_{i',k'-dk} - B_{i',j',k'}) \frac{dE_{k'-dk}}{E_{k'} - E_{k'-dk}} E_{k'-dk}^3 F_{i',j',k'-dk} \right. \\ &\left. - (\mu_{j'}^2 A_{i',k'} - B_{i',j',k'}) \frac{dE_{k'}}{E_{k'+dk} - E_{k'}} E_{k'}^3 F_{i',j',k'} \right]. \end{aligned} \quad (56)$$

New is the usage of the prefactors A and B as defined in Eqs. (40) and (46) such that the cancellations ($D_a^4 O_E^1$) and ($D_\mu^{12} O_E^{34}$) are exactly fulfilled (Liebendörfer 2000). Combining the partial updates of the observer correction into the single finite differencing step in Eq. (56) facilitates their inclusion into an update by implicit finite differencing.

3.2.6. Frequency shift in the gravitational potential

The correction stemming from the propagation of the particles in the gravitational potential, $C_t + D_E = 0$ in Eq. (19), is finite differenced in analogy with Eq. (56). We derive the discretization of the prefactor $G^E = \Gamma \frac{\partial \Phi}{\partial r}$ from Eq. (34) keeping the cancellation involving the terms ($C_t^4 D_a^2 D_E^1 O_\mu^1$) in mind:

$$\begin{aligned} G_{i+1}^E &= \frac{1}{\Gamma_{i+1}} \left(\frac{du}{\alpha_{i'} dt} + 4\pi r_{i+1} \rho_{i'} (1 + e_{i'} + p_{i'+1}/\rho_{i'}) \right) \\ &- \frac{1}{H_{i'}} \sum_{j,k} (\Lambda_{i',k'} - A_{i',k'}) F_{i',j',k'} E_{k'}^3 dE_{k'} \mu_{j'} w_{j'}. \end{aligned} \quad (57)$$

The coefficients $-A_{i',k'}$ and $\Lambda_{i',k'}$ from Eq. (40) and (41) construct the terms O_μ^1 and D_a^2 respectively. The time derivative du/dt requires adaptive grid corrections that are detailed in Eq. (B9). The implementation of the gravitational redshift is based on the same finite differencing as in Eq. (56) and reads with the new prefactor (57)

$$D_E = -\frac{\mu_{j'} G_{i+1}^E}{E_{k'}^2 dE_{k'}} \left[\frac{dE_{k'-dk}}{E_{k'} - E_{k'-dk}} E_{k'-dk}^3 F_{i',j',k'-dk} - \frac{dE_{k'}}{E_{k'+dk} - E_{k'}} E_{k'}^3 F_{i',j',k'} \right]. \quad (58)$$

This is a valid finite difference representation of $D_E = -\mu G^E/E^2 \cdot \partial(E^3 F)/\partial E$. We apply the corrections from Eqs. (56) and (58) with $dk = +1$ (blueshift) if $\sum_{j',k'} \mu_{j'}^2 A_{i',k'} - B_{i',j',k'}$ is positive with an absolute value $\left| \sum_{j',k'} (\mu_{j'}^2 A_{i',k'} - B_{i',j',k'}) \right| > \left| \sum_{j',k'} \mu_{j'} G_{i+1}^E \right|$, and with $dk = -1$ (redshift) otherwise. We know from Eq. (52) that a positive $\partial \ln R_f / \partial t$ corresponds to a shift to higher energies in the energy phase space so that the chosen sign of dk in Eqs. (56) and (58) implements upwind differencing. Note however, that the direction of the finite differencing in energy space must not depend on the angle bin in order to allow the necessary cancellations in the total gravitational redshift of in- and outgoing rays in an almost isotropic radiation field. Hence, the chosen differencing is upwind differencing for the angle averaged frequency shift, and not for each angular bin individually.

3.2.7. Angular aberration from observer motion

There remains the task of finding a finite difference representation of the angular aberration correction $C_t + O_\mu = 0$ in Eq. (21). Since the global energy depends on $(\Gamma_{i'} + u_{i'} \mu_{j'}) F_{i',j',k'}$ (Liebendörfer, Mezzacappa, & Thielemann 2001), any correction to the particle propagation direction also affects the energy conservation. It is therefore desirable to construct an implementation of angular aberration that allows an as precise prescription of the change of specific luminosity $\mu_{j'} F_{i',j',k'} w_{j'}$ as the frequency shift discussed in the previous paragraphs. As in (Liebendörfer 2000), we write the prefactor of correction (21) in terms of the quantities A and B defined in Eq. (49) and $\zeta = 1 - \mu^2$,

$$O_\mu = (A + B/\zeta) \frac{\partial}{\partial \mu} [\zeta \mu F].$$

As before, we search for an analytical solution to this update of the distribution function. And indeed, for the quantity $R_a = r^3 \rho$, we find

$$\frac{d \ln R_a}{\alpha dt} = A + B/\zeta.$$

It is now also possible to rewrite $0 = C_t + O_\mu$ in the “Lagrangian” variable $y = \zeta^{-1/2} \mu / R_a$ in angle momentum phase space instead of the “Eulerian” variable $x = \mu$. After a multiplication with $\zeta \mu$, the angular aberration correction $0 = C_t + O_\mu$ transforms to

$$0 = \zeta \mu \left[\left(\frac{\partial F}{\partial t} \right)_\mu + \alpha (A + B/\zeta) \frac{\partial}{\partial \mu} [\zeta \mu F] \right]$$

$$\begin{aligned}
&= \left(\frac{\partial}{\partial t} [\zeta \mu F] \right)_\mu + \zeta^{-1/2} \mu \frac{\partial R_a}{R_a^2 \partial t} \times \zeta^{3/2} R_a \frac{\partial}{\partial \mu} [\zeta \mu F] \\
&= \left(\frac{\partial}{\partial t} [\zeta \mu F] \right)_\mu - \left(\frac{\partial [\zeta^{-1/2} \mu / R_a]}{\partial t} \right)_\mu \frac{\partial [\zeta \mu F]}{\partial [\zeta^{-1/2} \mu / R_a]} = \left(\frac{\partial}{\partial t} [\zeta \mu F] \right)_{\zeta^{-1/2} \mu / R_a}.
\end{aligned}$$

The particles initially residing in the angular interval $(1 - 3\mu^2) \Delta\mu = \zeta_2 \mu_2 - \zeta_1 \mu_1$ are shifted by angular aberration along constant $\mu / (\sqrt{\zeta} R_a)$ in the angular phase space of a comoving observer

$$\left(\frac{\partial}{\partial t} [(1 - 3\mu^2) F \Delta\mu] \right)_{\zeta^{-1/2} \mu / R_a} = 0. \quad (59)$$

Based on this, we may evaluate the change in other particle properties, as for example the specific luminosity of those particles, $d\ell = (1 - 3\mu^2) \mu F \Delta\mu$,

$$\left(\frac{\partial}{\partial t} [(1 - 3\mu^2) \mu F \Delta\mu] \right)_{\zeta^{-1/2} \mu / R_a} = (1 - 3\mu^2) F \Delta\mu \left(\frac{\partial \mu}{\partial t} \right)_{\zeta^{-1/2} / R_a} = \zeta \frac{\partial \ln R_a}{\partial t} d\ell. \quad (60)$$

We then identify the bin size $(1 - 3\mu_{j'}^2) \Delta\mu_{j'} = w_{j'}$ with our Gaussian quadrature weights. As before, Eq. (59) leads to a condition for number conservation

$$F_{i',j',k'} w_{j'} - \left[\left(F_{i',j',k'} w_{j'} - n_{i',j',k'}^- \right) + n_{i',j'+dj,k'}^+ \right] = 0$$

and Eq. (60) produces a discrete prescription for the evolution of the luminosity

$$\begin{aligned}
F_{i',j',k'} \mu_{j'} w_{j'} &- \left[\left(F_{i',j',k'} \mu_{j'} w_{j'} - \mu_{j'} n_{i',j',k'}^- \right) + \mu_{j'+dj} n_{i',j'+dj,k'}^+ \right] \\
&= -(\zeta_{j'} A_{i',k'} + B_{i',j',k'}) F_{i',j',k'} \mu_{j'} w_{j'} \alpha_{i'} dt.
\end{aligned}$$

The increment $dj = \pm 1$ points to a neighbor bin. The solution for the update $F_{i',j',k'} = \bar{F}_{i',j',k'} + (n_{i',j',k'}^+ - n_{i',j',k'}^-) / w_{j'}$ is readily evaluated to become

$$\begin{aligned}
n_{i',j',k'}^- &= (A_{i',k'} + B_{i',j',k'} / \zeta_{j'}) \frac{w_{j'}}{\mu_{j'+dj} - \mu_{j'}} \zeta_{j'} \mu_{j'} F_{i',j',k'} \alpha_{i'} dt \\
n_{i',j',k'}^+ &= n_{i',j'-dj,k'}^-.
\end{aligned}$$

This leads to the following valid finite difference representation of $(A + B/\zeta) \partial (\zeta \mu F) / \partial \mu$ in the case of angular aberration:

$$\begin{aligned}
O_\mu &= \frac{1}{w_{j'}} \left[(A_{i',k'} + B_{i',j'-dj,k'} / \zeta_{j'-dj}) \frac{w_{j'-dj}}{\mu_{j'} - \mu_{j'-dj}} \zeta_{j'-dj} \mu_{j'-dj} F_{i',j'-dj,k'} \right. \\
&\quad \left. - (A_{i',k'} + B_{i',j',k'} / \zeta_{j'}) \frac{w_{j'}}{\mu_{j'+dj} - \mu_{j'}} \zeta_{j'} \mu_{j'} F_{i',j',k'} \right]. \quad (61)
\end{aligned}$$

We apply the aberration corrections with $dj = +1$ for $\mu \leq 0$ and $dj = -1$ for $\mu > 0$. This is not upwind differencing and therefore bears the risk of producing negative particle distribution

functions. There are however three reasons to accept this disadvantage: (i) The angular aberration correction is generally small with the only exception of strong shocks with large velocity gradients. (ii) As long as the angle integrated particle density is positive, transiently negative contributions from backwards directions on the Gaussian angular grid allow the computer representation of strongly forward peaked particle fluxes that would not be representable with positive particle distribution functions on a grid with limited angles $\mu_{\max} < 1$. (iii) The chosen direction of dj guarantees that no particles are shifted off the angular grid. This is a prerequisite for number and energy conservation.

3.2.8. Boundary corrections and the enforcement of Fermi statistics

There are k_{\max} energy groups that are subject to a frequency shift, but only $k_{\max} - 1$ enclosed group edges to shift particles across. In the energy phase space, upwind differencing is necessary and the straightforward application of Eqs. (56) and (58) unavoidably leads to particles that fall aside the grid. The resulting lack of particle number conservation and energy conservation is not acceptable. Thus, in our scheme, we do not apply the energy shift of the affected boundary group to the particle distribution function. Particle number is then conserved. The energy conservation is restored by applying an additional shift to the population of all other energy groups in a least invasive way that will be described here.

Another exceptional correction to the frequency shift is applied when the Fermi statistics of the radiation particles has to be enforced. The collision term C_c well includes all necessary blocking factors to avoid the overpopulation of states in the fermionic particle gas by emission or in-scattering. The transport terms $C_t + D_a + D_\mu + O_\mu + O_E$, however, do not know such means and particle distribution functions with values exceeding unity can well occur. As in (Mezzacappa & Bruenn 1993a), we apply another correction that recursively shifts overpopulated particles into the next higher energy group. This procedure is of course number conservative, but it introduces an artificial increase of the internal energy of the radiation field that we compensate by slightly lowering the energy of all higher energy nondegenerate populations.

These two corrections of completely different origin act on the particle distribution functions according to a similar mechanism. They are easily combined into the following correction scheme. First, we evaluate the missed energy contribution from the frequency shift of the boundary group

$$R_{i',j'} = (\mu_{j'}^2 A_{i',k'} - B_{i',j',k'} - \mu_{j'} G_{i+1}^E) \bar{F}_{i',j',k'} E_{k'}^3 dE_{k'},$$

with $k = k_{\max}$, if $dk = 1$ (blueshift); and $k = 1$, if $dk = -1$ (redshift). The boundary corrections are very small and the correction for Fermi statistics always leads to an energy redshift. Thus, we set $dk = -1$ and initialize the accumulation of corrections in $\Delta_{i',j',k'}$ with $\Delta = 0$. Then, we loop over k in ascending order and carry out the following procedure: (i) Distribute the correction $R_{i',j'}$

over all groups ℓ' with $k+1 \leq \ell \leq k_{\max}$ according to

$$\Delta_{i',j',\ell'} = \Delta_{i',j',\ell'} + \frac{R_{i',j'}}{\sum_{s=k+1,k_{\max}} \bar{F}_{i',j',s'} E_{s'}^3 dE_{s'}}.$$

(ii) Apply the correction $\Delta_{i',j',k'+1}$ according to the conservative finite differencing used in Eq. (55)

$$n_{i',j',k'}^+ = -\Delta_{i',j',k'+1} \frac{dE_{k'+1}}{E_{k'+1} - E_{k'}} E_{k'+1}^3 \bar{F}_{i',j',k'+1}$$

and update the particle distribution function

$$\frac{F_{i',j',k'} - \bar{F}_{i',j',k'}}{\alpha_{i'} dt} = \frac{n_{i',j',k'}^+ - n_{i',j',k'-1}^+}{E_{k'}^2 dE_{k'}}. \quad (62)$$

(iii) If the distribution function $F_{i',j',k'}$ is larger than $1/\rho_{i'}$, correct the particle flux into this group by the amount of overpopulation, $n_{i',j',k'}^+ = n_{i',j',k'}^+ + (1/\rho_{i'} - F_{i',j',k'}) E_{k'}^2 dE_{k'}$, and evaluate the energy change owing to this flux correction,

$$R_{i',j'} = (1/\rho_{i'} - F_{i',j',k'}) (E_{k'+1} - E_{k'}) E_{k'}^2 dE_{k'}.$$

Set $F_{i',j',k'}$ to the maximum value, $1/\rho_{i'}$ and apply the energy correction $R_{i',j'}$ with the next iteration of the loop over k .

3.3. Coupling between the radiation field and the fluid

The neutrino radiation field in a supernova is tightly coupled to the high density fluid. In order to obtain a well defined split between the evolution of radiation quantities treated in the Boltzmann equation (15) and the evolution of hydrodynamical quantities, we recall that the solution of the Boltzmann equation updates the radiation quantities according to Eqs. (26)-(28). We may now subtract these updates from the global evolution equations (6)-(11) and (12) to find the hydrodynamical part of the evolution equations

$$\frac{\partial}{\partial t} \left[\frac{\Gamma}{\rho} \right] = \frac{\partial}{\partial a} [4\pi r^2 \alpha u] \quad (63)$$

$$\begin{aligned} \frac{\partial}{\partial t} [\Gamma (1 + e)] &= -\frac{\partial}{\partial a} [4\pi r^2 \alpha u p] \\ &\quad - \alpha \Gamma \int \left(\frac{j}{\rho} - \chi F \right) E^3 dE d\mu + \alpha u \int \chi F E^3 dE d\mu \end{aligned} \quad (64)$$

$$\begin{aligned} \frac{\partial}{\partial t} [u (1 + e)] &= -4\pi r^2 \frac{\partial}{\partial a} [\alpha \Gamma p] \\ &\quad - \frac{\alpha}{r} \left[(1 + e) \left(1 + \frac{6Vp}{m} \right) \frac{m}{r} + 4\pi r^2 ((1 + e) \rho K + p J) \right] \end{aligned}$$

$$\begin{aligned}
& + \left(2u^2 - \frac{m}{r} \right) \frac{2p}{\rho} \Big] \\
& + \alpha \Gamma \int \chi F E^3 dE \mu d\mu - \alpha u \int \left(\frac{j}{\rho} - \chi F \right) E^3 dE d\mu
\end{aligned} \tag{65}$$

$$\frac{\partial}{\partial t} Y_e = \mp \alpha \int \left(\frac{j}{\rho} - \chi F \right) E^2 dE d\mu \tag{66}$$

$$\frac{\partial V}{\partial a} = \frac{\Gamma}{\rho} \tag{67}$$

$$\frac{\partial m}{\partial a} = \Gamma (1 + e + J) + u H \tag{68}$$

$$\rho (1 + e) \frac{\partial \alpha}{\partial a} = - \frac{\partial}{\partial a} [\alpha p] + \frac{\alpha}{4\pi r^2} \int \chi F E^3 dE \mu d\mu \tag{69}$$

$$\frac{\partial e}{\partial t} = - p \frac{\partial}{\partial t} \left(\frac{1}{\rho} \right) - \alpha \int \left(\frac{j}{\rho} - \chi F \right) E^3 dE d\mu. \tag{70}$$

The equations are formulated in such a way that the presence of the radiation field only enters in terms of energy and momentum exchange. In the limit of a decoupled radiation and matter flow we therefore solve for ideal hydrodynamics and free streaming in an independent and numerically stable manner, no matter what the size of the radiation field is. The only remaining interactions between the radiation field and the fluid are of a gravitational nature, for example in the contribution of the radiation field to the common gravitational mass in Eq. (68), or in the term $4\pi r^2 ((1 + e) \rho K + p J)$ in the momentum equation (65). The detailed discretization of Eqs. (63)-(70) has been described in (Liebendörfer, Rosswog & Thielemann 2002). The interaction terms between the radiation field and the fluid are

$$\begin{aligned}
e_{i'}^{\{\text{ext}\}} &= \sum_{j', k'} \left(\frac{j_{k'}(\rho_{i'}, T_{i'}^*, Y_{e, i'}^*)}{\rho_{i'}} - \chi_{k'}(\rho_{i'}, T_{i'}^*, Y_{e, i'}^*) F_{i', j', k'} \right) E_{k'}^3 dE_{k'} w_{j'} \\
S_{i'+1}^{\{\text{ext}\}} &= - \sum_{j', k'} \chi_{k'}(\rho_{i'}, T_{i'}^*, Y_{e, i'}^*) F_{i', j', k'} E_{k'}^3 dE_{k'} \mu_{j'} w_{j'} \\
Y_{e, i'}^{\{\text{ext}\}} &= \mp \sum_{j', k'} \left(\frac{j_{k'}(\rho_{i'}, T_{i'}^*, Y_{e, i'}^*)}{\rho_{i'}} - \chi_{k'}(\rho_{i'}, T_{i'}^*, Y_{e, i'}^*) F_{i', j', k'} \right) E_{k'}^2 dE_{k'} w_{j'},
\end{aligned} \tag{71}$$

where the minus sign in the Y_e -term is used for electron neutrinos and the plus sign for electron antineutrinos. Emission and absorption of $\mu-$ and τ -neutrinos do not change the electron fraction. The star subscript for the temperature and electron fraction variables indicates an evaluation of the cross sections for emission and absorption with a consistently updated thermodynamical state as described in the next section. A more complete description of the finite difference representation of the weak interactions in our code, including scattering and pair production, has been summarized in (Mezzacappa & Messer 1999).

3.4. Code flow

Now that we have finally described the individual finite differencing for all terms in the Boltzmann equation (15), we are ready to join them to an overall solution of the radiation hydrodynamical evolution. In our former simulations, (Mezzacappa et al. 2001; Liebendörfer et al. 2001), a full time step has been split threefold: into transport step, observer corrections, and hydrodynamics update, while the update due to transport, $C_t + D_a + D_\mu = C_c$, and hydrodynamics have been implemented with implicit finite differencing and the update from gravitational redshift and observer corrections, $C_t + D_E + O_\mu + O_E = 0$, with explicit finite differencing. However, the propagation angle dependent gravitational redshift contribution in the compact proto-neutron star drives the neutrino distribution out of the equilibrium on a very short time scale such that an operator splitting between this update and the restoration of equilibrium by the collision term was unfortunate. It led to a severely restricted time step in the longterm evolution of the problem. Hence, we included the gravitational and observer corrections into the implicit part. We perform the time evolution as a sequence of $1 \dots n$ time steps or cycles leading to time $t(n)$. Each cycle contains a sequence of several updates. The intermediately updated values are not belonging to uniquely defined physical times. We denote them by fractional values of the cycle counter. The updates of the primitive variables in one cycle are handled as follows:

1. We start with the neutrino distribution function $\bar{F} := F(n-1/2)$, given on a Lagrangian mass grid \bar{a} . We assume that we already know the hydrodynamic variables at step $\{\bar{a}, \bar{r}, \bar{u}, \bar{m}, \bar{\rho}, \bar{T}, \bar{Y}_e, \bar{\alpha}\} := H(n-1)$ as well as at step $\{a, r, u, m, \rho, T, Y_e, \alpha\} := H(n)$. In one update, we implicitly solve for $F(n) := F$ as prescribed by $C_t + D_a + D_\mu + D_E + O_E + O_\mu - C_c = 0$. The finite differencing is outlined in expressions (35), (38), (42), (58), (56), (61), and (36). Moreover, we implicitly couple the evolution of the neutrino distribution function to the radiation induced evolution of the electron fraction and temperature by additionally solving for

$$\frac{e_{i'}^* - e_{i'}^*}{dt} = \alpha_{i'} e_{i'}^{\{\text{ext}\}} \quad (72)$$

$$\frac{Y_{e,i'}^* - Y_{e,i'}^*}{dt} = \alpha_{i'} Y_{e,i'}^{\{\text{ext}\}}, \quad (73)$$

where the source term is given in Eq. (71). Note that internal energy and temperature are always linked by the equation of state, $e^*(\rho, T^*, Y_e^*)$ and $e(\rho, T, Y_e)$. The joint update of the neutrino distribution function with the temperature-sensitive neutrino opacities is important to safely find a quasi-equilibrium neutrino distribution function.

2. In this minor second update, we correct for discretization errors caused by the advection scheme in the energy phase space and for numerical violations of Fermi statistics. This update is not related to physical terms appearing in the Boltzmann equation. We set $\bar{F} := F(n)$, and update $F(n+1/2) := F$ as described by Eq. (62).
3. In the hydrodynamical update, the variables $\{\bar{a}, \bar{r}, \bar{u}, \bar{m}, \bar{\rho}, \bar{T}, \bar{Y}_e, \bar{\alpha}\} := H(n)$ are evolved to $H(n+1) := \{a, r, u, m, \rho, T, Y_e, \alpha\}$ in a fully implicit step according to Eqs. (63)-(70). Note

that we use the neutrino distribution function $F(n)$ rather than $F(n + 1/2)$ to evaluate the moments J , H , and K for the gravitational coupling. The former represent more accurately the quasi-stationary values. The hydrodynamics update is based on the transfer of internal energy, $e^{\{\text{ext}\}}$, electron fraction, $Y_e^{\{\text{ext}\}}$, and the neutrino stress, $S^{\{\text{ext}\}}$, as evaluated in the first step of this cycle. The finite difference representation in AGILE has been detailed in (Liebendörfer, Rosswog & Thielemann 2002).

Steps 1, 2, and 3 form literally a cycle; there is no position where *all* data are consistently updated. After step 1, the neutrino distribution functions $F(n)$ are in accurate equilibrium with the matter. After step 2, the energy conserving corrections from energy advection are included and the distribution functions $F(n + 1/2)$ obey Fermi statistics. After step 3, the overall energy conservation is balanced, but the new hydrodynamic variables $H(n + 1)$ already live on a different spatial grid than the neutrino distribution function. We chose to set the integer value of n at the instance we dump the result into files. This is between step 1 and step 2, where all quantities live on the same grid positions and where all rates and neutrino distribution functions accurately reflect equilibrium conditions if the mean free paths are small.

4. Description of two representative simulations

In this section, we provide an overview of core collapse and postbounce evolution in our models for the $13 M_\odot$ and $40 M_\odot$ stellar progenitors. These provide the physical context for the code tests in following the next section. A thorough discussion of supernova physics can be found in previous reviews, e.g. in (Bethe 1990; Janka, Kifonidis & Rampp 2001). The specific phenomenology of our $13 M_\odot$ model was outlined in (Mezzacappa et al. 2001; Liebendörfer et al. 2001)⁷. Here, we report on our first self-consistent simulation running all the way from core collapse to black hole formation in the case of the $40 M_\odot$ progenitor and add information on the formation of the neutrino luminosities. The chosen progenitors on the light and massive side of core collapse supernova progenitors might demonstrate the range of expected phenomena. Simulations for intermediate mass progenitors have been discussed in (Messer 2000; Liebendörfer et al. 2001a) based on a former finite differencing; and in (Liebendörfer et al. 2002) with the finite differencing documented in this paper.

As the most prominent characterization of attempted supernova simulations that do not yield an explosion, we draw the shock trajectories for our two progenitors in Figure (1). Our shock position marks the location with the maximum absolute value of the infall velocity. Before collapse, this is the sonic point, i.e. the separation between the causally connected inner core, and the outer core where infall velocities become supersonic. The left hand side of the figure zooms in on bounce.

⁷In appendix C we relate the finite differencing described in this paper to the former code version used in simulations for these publications.

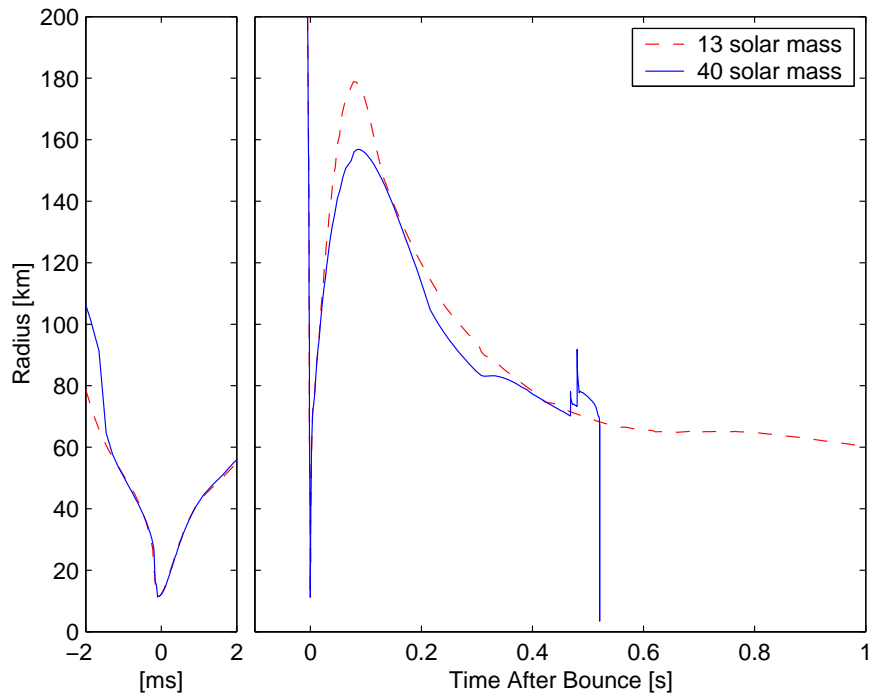


Fig. 1.— The trajectories show the position of the sonic point before bounce and the position of the shock front after bounce. The left hand part of the figure zooms on bounce and demonstrates the convergence of the sonic point in our models. The right hand part shows the shock trajectories over a longer time scale. After about 500 ms, the $40 M_{\odot}$ star collapses to a black hole.

It demonstrates convergence to exactly the same position of the sonic point in the two models. The “standard” electron capture rate for nuclei implements a hard cutoff due to the $f7/2$ shell closure (Bruenn 1985). This leads in our simulations to the dominance of electron capture on free protons when this shell in the heavy nuclei is closed. The convergence of the sonic point is a direct consequence of a negative feedback of the electron fraction evolution on the free proton abundance (Liebendörfer et al. 2002). This convergence may not occur with more realistic electron capture rates and is the subject of a more thorough investigation (Messer et al. 2002). The right hand side of Fig. (1) shows the shock trajectories over a longer time interval, up to one second after bounce. The transient stall in the receding shock front of the $40 M_{\odot}$ model at 0.3 s after bounce is a reaction to an enhanced electron flavour luminosity. It will be further analyzed with the description of the luminosities in a later section. In the evolution of the $40 M_{\odot}$ progenitor, we encountered a numerical stability problem after $t_{pb} = 0.4$ s. The adaptive grid created extremely small mass zones such that the convergence radius of the Newton-Raphson algorithm in the implicit hydrodynamics was severely reduced due to truncation errors. We increased the artificial viscosity in two sequential steps to widen the shock and continue the run. This numerical shock widening is responsible for the outward steps in the shock position ~ 0.5 s after bounce, just before the collapse of the protoneutron star to a black hole. Shortly later, our code crashes unavoidably because of the coordinate singularity in the comoving coordinates at the Schwarzschild horizon. We will extensively use the hydrodynamic profiles at 0.4 s after bounce for testing in later subsections.

We show the neutrino luminosities and rms energies around bounce in Fig. (2). The electron neutrino luminosities rise during core collapse up to bounce. The collapse is halted at nuclear densities and a bounce shock propagates outwards through neutrino opaque material. The neutrino luminosity decays to a lower level during this time of ~ 4 ms duration. When the shock reaches the electron neutrinosphere, an electron neutrino burst is launched by precipitous electron capture. The escaping neutrinos cease to block the phase space for the final state of the emitted electron neutrinos. Because of the very similar inner cores of the two different progenitors, the neutrino burst is almost identical. Differences appear later, when the accretion luminosity dominates over core diffusion luminosity. The higher densities in the outer layers of the more massive progenitor produce considerably higher accretion luminosities as they infall than the less dense outer layers of the smaller progenitor.

The rms energies before bounce reflect the conditions in the compactifying material at infall. After the neutrino burst, the rms energies adjust to the spectrum set by the shock heated mantle. The rms energy of the emanating neutrinos reflects the conditions at the location of decoupling. However, we have to keep in mind that the location of decoupling strongly varies for individual neutrino flavours and neutrino energies. Thus, the rms energy rather reflects an emission-weighted sampling of conditions at different locations. Quite generally, the μ and τ neutrinos decouple deeper because of the insensitivity of these neutrinos to charged current reactions, and the electron antineutrinos decouple deeper than the electron neutrinos because the proton abundance is much smaller than that of the neutrons.

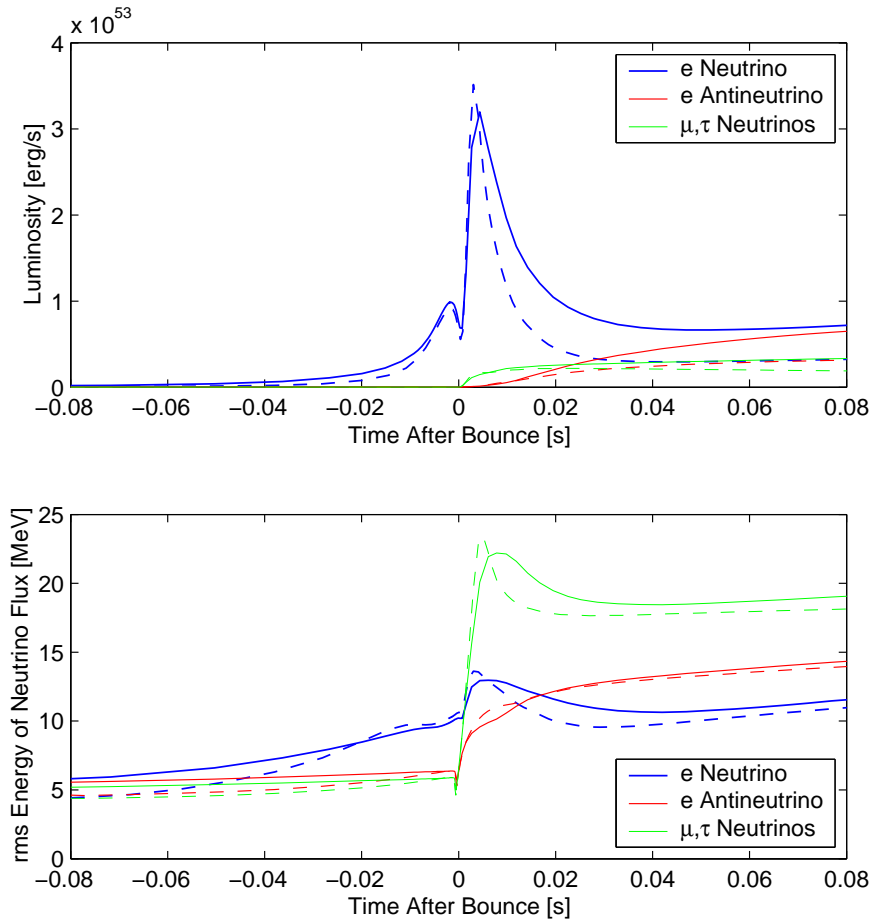


Fig. 2.— The luminosities and rms energies of the neutrinos are shown in this Figure as a function of time. We sample these quantities at a radius of 500 km and adjust the time coordinate by $\Delta t = -500 \text{ km}/c$ to eliminate the propagation time to the sampling radius. The two progenitors show a comparable neutrino burst and very different luminosities afterwards, during steady accretion of the outer layers.

In order to investigate the origin of the neutrino luminosities in more detail, we introduce in appendix D attenuation coefficients, ξ , that allow one to write the total luminosity as a weighed integration over neutrino sources. The neutrino phase space integrated energy emissivity $j^l(r)$ at radius $0 \leq r \leq R$ for reaction l contributes to the total luminosity, $L(R) = \sum L^l(R)$, at the surface of the star with

$$L^l(R) = \int_0^R \xi(r) j^l(r) 4\pi r^2 dr. \quad (74)$$

In the lowermost graphs in Figs. (3), (4), and (5) we show the neutrino sources $4\pi r^2 \xi(r) j^l(r)$ (with positive values) as a function of radius. Thick lines, (e), show the contributions from electron or positron capture, moderately thick lines, (f), show contributions from pair production, and thin lines, (g), show energy exchange by neutrino electron scattering. We use solid lines for electron neutrinos, dashed lines for electron antineutrinos, and dash-dotted lines for the μ -neutrino. We do not graph quantities for the μ -antineutrino and τ -(anti)neutrino because they are very similar to the quantities of the μ -neutrino. Note that the area enclosed under a source graph is an estimate for the total luminosity, $L^l(R)$, produced by reaction l . However, the area enclosed by lines for sinks do not have a global physical meaning. The absorption is shown to demonstrate the importance of absorption of type l in a local comparison with the emissivity j^l at the locations in the star where the luminosity and spectra are formed.

Fig. (3), for example, shows a time slice in the collapse of the $13 M_\odot$ progenitor at 5 ms before bounce. The upper two graphs show the thermodynamic conditions interior to a radius of 150 km. It is determined by the density, (a), the temperature, (c), and the electron fraction, (d). Also shown is the mass flux as a function of radius, (b). We note that the matter up to ~ 75 km is under compression at this time. The graph with the emissivities demonstrates an electron capture peak at 70 km radius. Emission is more steeply declining towards the interior because of the increased opacities. The infalling matter at larger radii also contributes to the luminosity with more broadly distributed emissivities below the trapping density. These absorptivities demonstrate the well-known fact that neutrino electron scattering is as important as neutrino reabsorption for the energy exchange between matter and electron neutrinos during infall. There is no relevant production of electron antineutrinos because of the absence of positrons under electron degeneracy.

The origin of the neutrino burst is shown in Fig. (4) at 5 ms after bounce. The mass flux, (b), exhibits a region of strong compression around a radius of 65 km. The infalling material with initially high electron fraction, (d), is heated, (c), by the shock. It emits neutrinos at a rate of order 5×10^{52} erg/s/km from a very narrow region behind the shock. Fig. (5) describes the situation at 50 ms after bounce. All luminosities are fully developed at this time. We see in the lowermost graph the origin of electron neutrino luminosities ~ 80 km, of electron anti-neutrino luminosities ~ 60 km, and of μ -neutrino luminosities ~ 30 km. This is the expected hierarchy. Note that emissivities of electron flavor neutrinos in moderately transparent regions may result in root mean square emission radii that are outside of the neutrinospheres. We can also deduce from the graph that neutrino electron scattering is an important energy sink for the luminosity and spectrum of the μ and τ flavor neutrinos. In our model, pair production is currently their only production

reaction. Pair production does not visibly contribute to the electron flavor luminosities.

Figure (6) shows the luminosities and rms energies of the neutrino flux after bounce on a longer time scale. In the $13 M_{\odot}$ model, the luminosities decrease as a consequence of the declining accretion rate and continued deleptonization of the core. The more massive $40 M_{\odot}$ model shows qualitatively different features. One can interpret the luminosity features in terms of the root mean square radius of neutrino emission (see appendix D for a more detailed definition), the root mean square entropy of the matter at the locations of neutrino emission, and the root mean square electron fraction at the origin of the neutrino emission. These quantities are shown in Fig. (7) for the $13 M_{\odot}$ star from bounce to 800 ms after bounce and for the $40 M_{\odot}$ star from 0.2 to 0.4 ms after bounce. Again, we use a solid line for the electron neutrino, a dashed line for the electron antineutrino, and a dash-dotted line for the μ -neutrino. In the simulation of the $13 M_{\odot}$ star, all neutrino spheres retract continuously after an initial phase of expansion in the first 20 ms after bounce. Consulting Figs. (20), (21), and (22) will put the traces in Fig. (7) into the context of a more detailed profile of the star at 10 ms, 100 ms, and 400 ms after bounce. Although the emission radii of the electron neutrino and antineutrino converge to a large extent at late times, there are significant differences in the rms entropy and rms electron fraction because of the steep gradient these latter quantities exhibit across the density cliff at the surface of the protoneutron star. The emission region for the electron flavor neutrinos is in the midst of this transition between the low entropy material and the accreting material with rising entropy differences because of the larger gravitational energy dissipated in the receding shock. In opposition to this, the production of μ - and τ -neutrinos predominantly occurs in the deleptonized low entropy material, which is further cooling and compactifying. The high electron degeneracy under these conditions suppresses the positron abundance, and as a consequence, the pair production of μ - and τ -neutrinos. We observe in Fig. (6) that the rms energy of the μ -neutrinos may even fall below the rms energy of the electron antineutrino, as it happens at 700 ms after bounce.

This is different in the simulation of the $40 M_{\odot}$ star. However, before discussing the luminosities we compare the mass flux in different time slices as shown in Fig. (8). The time slices cover the times from 100 ms to 500 ms after bounce in steps of 100 ms. The mass flux in the simulation of the $13 M_{\odot}$ star is shown as dashed lines, the mass flux in the simulation of the $40 M_{\odot}$ star as solid lines. There is the following qualitative difference: The $13 M_{\odot}$ star is far from its critical mass for further collapse. It appears as a quite incompressible inner core to the accreting outer layers. The $40 M_{\odot}$ star, on the other hand, behaves in a very similar way during the first 300 ms after bounce before the compactification of the inner core suddenly starts to accelerate. Nevertheless, this is still a hydrostatic phase preceding the later collapse to a black hole ~ 500 ms after bounce. Nonlinear general relativistic terms in the hydrodynamics equations lead to enhanced gravitational forces for further compactification such that the inner core appears more compressible to the accreting layers. This qualitative change coincides with the strong features in the luminosities presented in Fig. (6). We explain the step in electron flavor luminosities at 300 ms after bounce by the acceleration of accretion. The negative density gradient of the infalling matter continuously reduced the mass flux

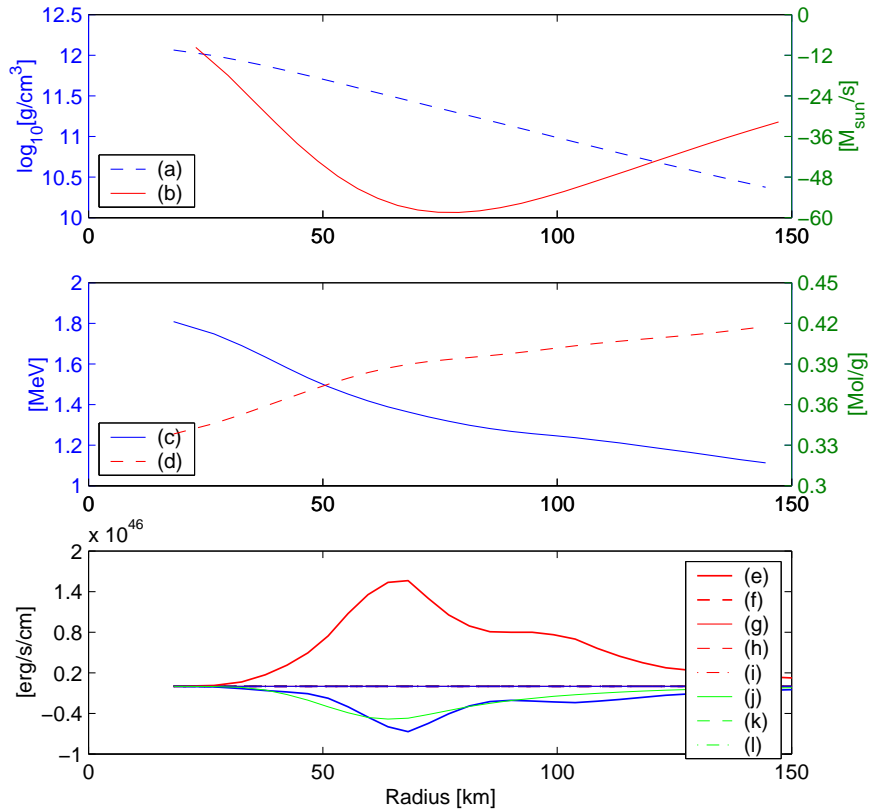


Fig. 3.— The upper two graphs show the thermodynamic conditions interior to a radius of 150 km in the evolution of the $13 M_{\odot}$ progenitor. The time is 5 ms before bounce. The plotted quantities are: (a) density, (b) mass flux, (c) temperature, (d) electron abundance. The lowermost graph shows the origin of the electron flavor neutrino luminosities as energy emission rates per radius interval. Linetype (e) with positive values indicates neutrino emission by electron capture, linetype (e) with negative values the inverse process. Line (j) represents the important neutrino-electron scattering during infall. The total luminosity of the star corresponds to the integral of the lines with positive values over radius.

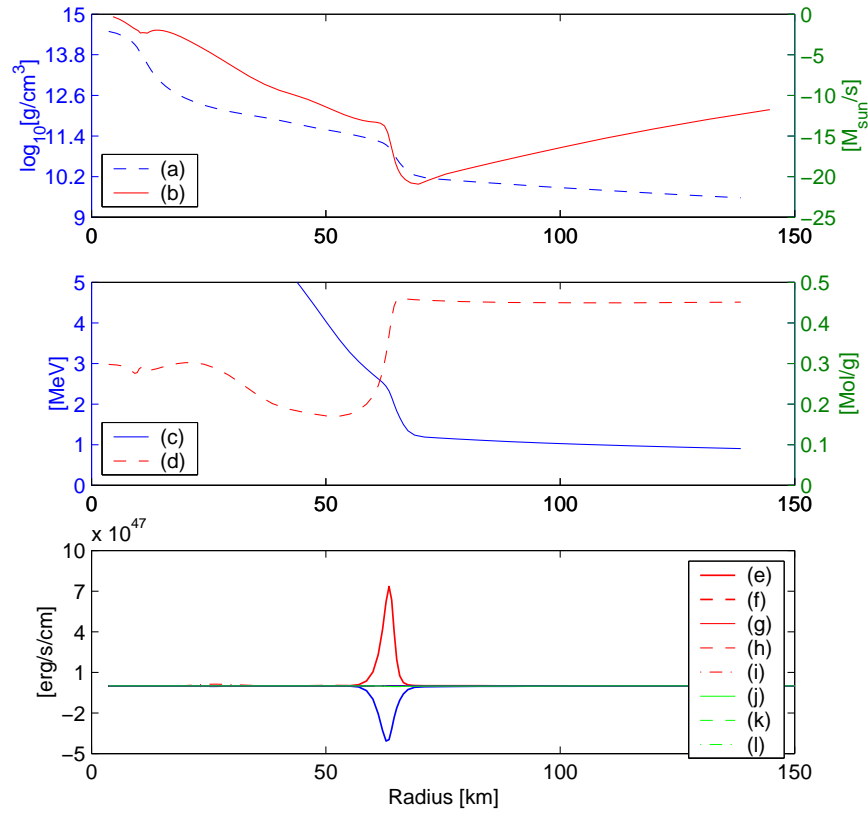


Fig. 4.— As in Fig. (3), but 5 ms after bounce. The mass flux (b) shows reduced infall inside of the shock front. The high electron abundance together with the reduced opacity leads to strong electron neutrino emission (30 times that shown in Fig. (3)) from a very narrow region.

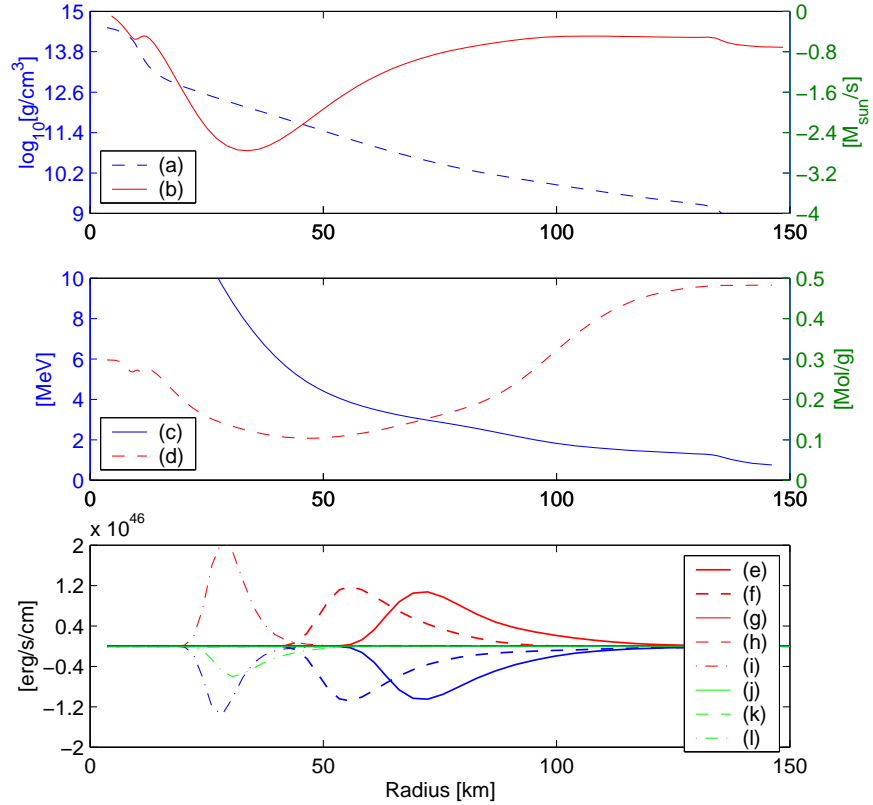


Fig. 5.— Similar to Fig. (3), but 50 ms after bounce. In the lowermost graph, we detail the origin of the neutrino luminosities. Lines with positive values show energy emission rates per radius interval, lines with negative values contrast the local energy emission rate with equally scaled energy absorption rates. We use solid lines for electron neutrinos, dashed lines for electron antineutrinos, and dash-dotted lines for μ - and τ -neutrinos. The reactions are: (e) electron capture, (f) positron capture, (g,h,i) pair production, (j,k,l) electron scattering. Line (l) demonstrates the importance of neutrino electron scattering for the μ - and τ -neutrinos.

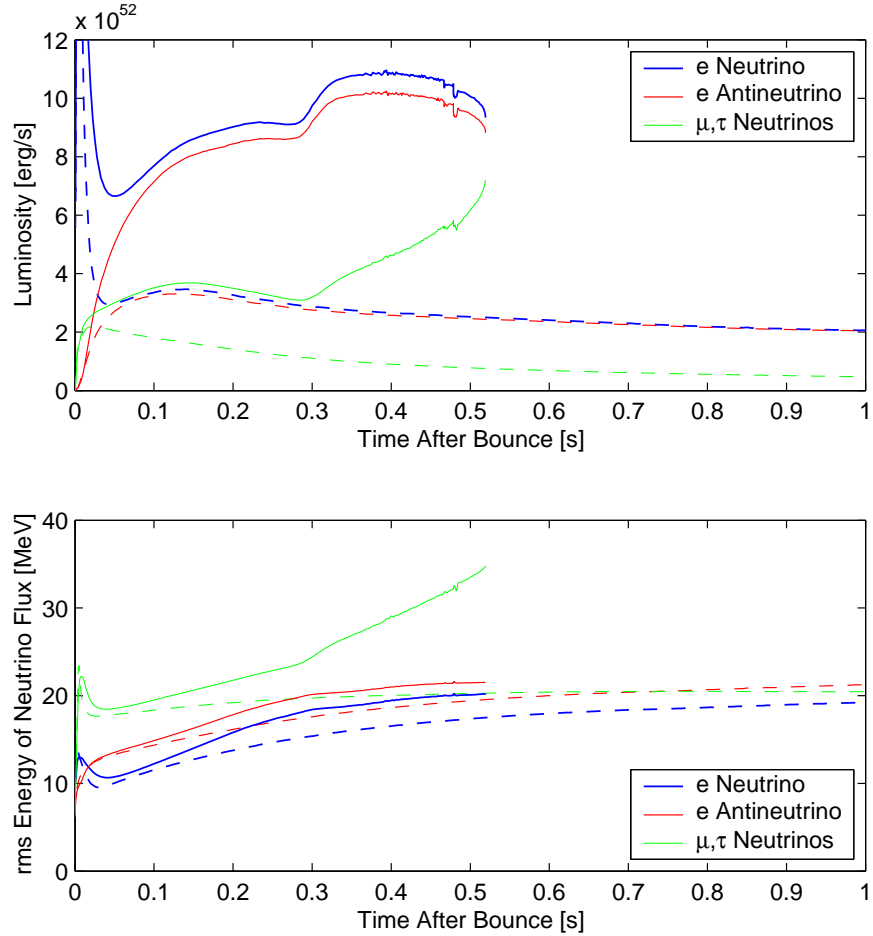


Fig. 6.— Here, we show the evolution of the luminosities and rms energies on a longer time scale. The $13 M_\odot$ model (dashed lines), far from forming a black hole, exhibits very slow changes in all quantities, while the luminosities in the $40 M_\odot$ model (solid lines) reflect the dynamics around black hole formation to a larger extent.

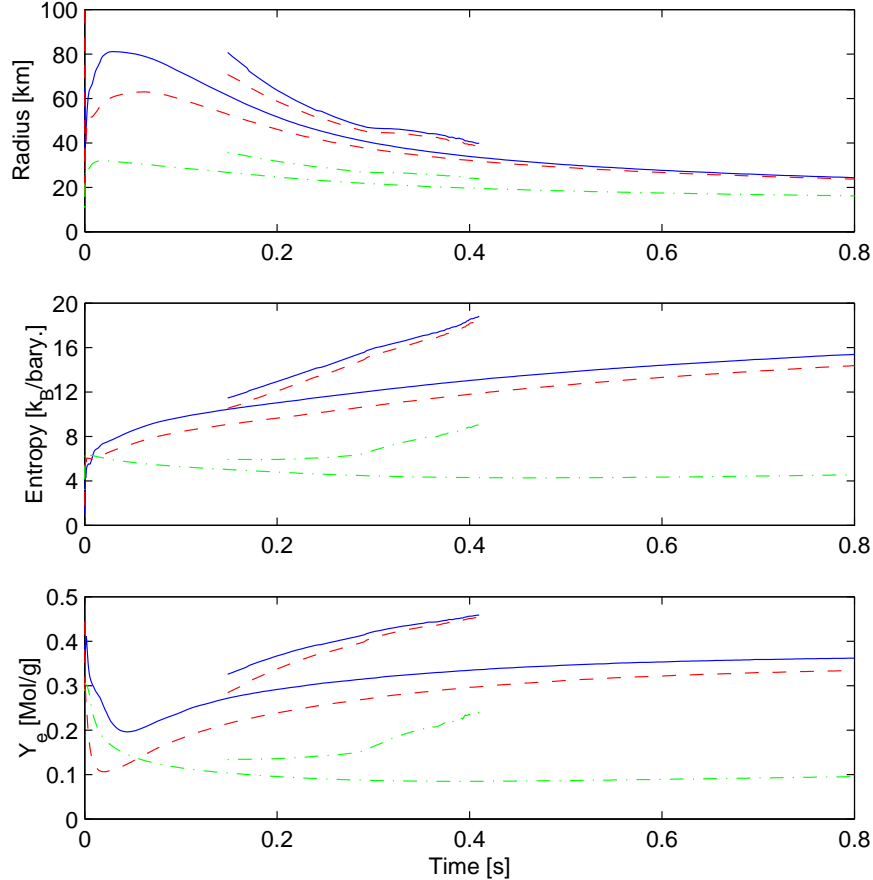


Fig. 7.— This figure shows traces of the energy emission weighted rms values for radius, entropy, and electron abundance of the material from which the neutrino luminosity originates. The solid lines correspond to the electron neutrino, the dashed lines to the electron antineutrino, and the dash-dotted line to the μ - and τ -neutrinos. The data for the $13 M_\odot$ star extends from bounce to 800 ms after bounce, the data for the $40 M_\odot$ star is inset across the interesting region from 200 ms to 400 ms.

with time. This is not to the same extent true between 300 ms and 400 ms after bounce, where the reduction in mass flux transiently comes to a complete stall. The higher accretion luminosities push the shock slightly outwards (see Fig. (1)) and the rms radius for electron flavor emission stops receding as well. This is evident in the uppermost graph of Fig. (7). The inset in the graph with the entropy shows a less steep entropy gradient at the rms emission position because it approaches the peak entropy. Correspondingly, the rms energies of the electron flavor neutrinos in Fig. (6) can be observed to increase more slowly. The luminosities and rms energies of the μ - and τ -neutrinos, however, increase steeply after 300 ms post bounce time. By the accelerated infall of the entire entropy- and electron fraction profile, the rms emission position of μ - and τ -neutrinos moves into the border of the not yet completely deleptonized material with higher entropies. The traces in the lower two graphs of Fig. (7) show a sudden increase in electron abundance and entropy. The reduced electron degeneracy allows higher positron populations and the pair production process for the μ - and τ -neutrinos dramatically increases its efficiency, leading to increasing luminosities and increasing rms energies. Unfortunately, we cannot follow the evolution any further at the time being because of the singularity at the forming Schwarzschild horizon. However, the neutrino luminosities are expected to decay on a short timescale (see e.g. (Baumgarte et al. 1985)).

5. Code Verification

We continue in this section with individual tests of the new terms and finite difference representations introduced since (Mezzacappa & Bruenn 1993a,b,c). First we investigate the diffusion limit and demonstrate that the diffusive flux is not affected by large and nearly isotropic radiation fields in our finite difference representation. We also check the other extreme, the evolution of the radiation moments in a free streaming situation in spherically symmetric geometry. Another test in stationary space-time investigates the implementation of gravitational terms, such as the radiative flux conservation, the gravitational frequency shift, and light bending. The additional frequency shift and angular aberration in the radiation field, as an effect of observer motion, are probed at the shock front, where we relate the discontinuity in radiation quantities to the smooth radiation field in the view of stationary observers. Finally, we perform a detailed energy and lepton number conservation analysis to check the overall consistency of our code. In the intended application of stellar core collapse and postbounce evolution, we compare our results with the independently developed multi-group flux-limited diffusion (MGFLD) code of (Bruenn, DeNisco, & Mezzacappa 2001; Bruenn et al. 2002). The latter implements a sophisticated but approximative treatment of radiative transfer in spherical symmetry and uses a different hydrodynamics code. The very similar results validate the the approximations in MGFLD whose effects were difficult to quantify in the dynamical context without a direct comparison to the now available complete solution of the Boltzmann transport equation (see (Messer et al. 1998; Yamada, Janka, & Suzuki 1999) for a stationary state comparison).

5.1. Diffusion limit

The neutrinos in the interior region of the protoneutron star are almost completely trapped. Because of the high electron chemical potential, they equilibrate with matter at elevated root mean square energies. The neutrino number density multiplied by the speed of light considerably exceeds the neutrino number flux. It is therefore essential that the finite difference representation of the Boltzmann equation does not allow errors in the large particle density and pressure to swamp the by orders of magnitude smaller particle flux. A derivation of the analytical diffusion equation from the Boltzmann equation is the first step in the derivation of a multi-group flux limited diffusion scheme (Bruenn 1985). We follow here exactly the same procedure in the finite difference world, but for simplicity, on a stationary background. The particle distribution function is assumed to have an isotropic and a flux component,

$$F_{i',j',k'} = \psi_{i',k'}^0 + \mu_{j'} \psi_{i',k'}^1.$$

We further assume that the flux component is stationary to the point that its time dependence in the radiation moment equation becomes negligible. Substituting this approximation of the neutrino distribution function into the finite difference representation of the Boltzmann equation 15 with time-independent hydrodynamics, $C_t + D_a + D_\mu + D_E = C_c$, and evaluating the radiation moment equation by the application of the operator $(3/2) \sum_j \mu_{j'} w_{j'}$ leads to

$$\begin{aligned} R_a^0 + R_a^1 + R_\mu^0 + R_\mu^1 + R_E^0 &= R_c, \quad \text{with} \\ R_a^0 &= \frac{2\pi}{\alpha_{i'} da_{i'}} [r_{i+1}^2 (\alpha_{i'} \rho_{i'} \psi_{i',k'}^0 + \alpha_{i'+1} \rho_{i'+1} \psi_{i'+1,k'}^0) \\ &\quad - r_i^2 (\alpha_{i'-1} \rho_{i'-1} \psi_{i'-1,k'}^0 + \alpha_{i'} \rho_{i'} \psi_{i',k'}^0)] \\ R_a^1 &= \frac{-3\pi}{2\alpha_{i'} da_{i'}} [r_{i+1}^2 (1 - 2\beta_{i+1,k'}) (\alpha_{i'} \rho_{i'} \psi_{i',k'}^1 - \alpha_{i'+1} \rho_{i'+1} \psi_{i'+1,k'}^1) \\ &\quad - r_i^2 (1 - 2\beta_{i,k'}) (\alpha_{i'-1} \rho_{i'-1} \psi_{i'-1,k'}^1 - \alpha_{i'} \rho_{i'} \psi_{i',k'}^1)] \\ R_\mu^0 &= -2\Upsilon_{i+1} \psi_{i',k'}^0 \\ R_\mu^1 &= 3\Upsilon_{i+1} \sum_j \mu_{j'} [(1 - \gamma_{i',k'}) \zeta_{j+1} (\mu_{j'+1} - \mu_{j'}) + \gamma_{i',k'} \zeta_j (\mu_{j'} - \mu_{j'-1})] \psi_{i',k'}^1 \\ R_E^0 &= -\frac{G_{i+1}^E}{E_{k'}^2 dE_{k'}} \left(\frac{dE_{k'-dk}}{E_{k'} - E_{k'-dk}} E_{k'-dk}^3 \psi_{i',k'-dk}^0 - \frac{dE_{k'}}{E_{k'+dk} - E_{k'}} E_{k'}^3 \psi_{i',k'}^0 \right) \\ R_c^1 &= -\chi_{i',k'} (\rho_{i'}, T_{i'}^*, Y_{e,i'}^*) \psi_{i',k'}^1. \end{aligned} \tag{75}$$

We have made use of $\sum_j \mu_{j'}^2 w_{j'} = 2/3$ to derive these equations. The simple expression R_μ^0 results from the specific property (43) of the angular difference coefficients. The different treatment of ingoing and outgoing particles in the choice of the transport coefficients in Eq. (37) is responsible for the unwanted term R_a^1 . Also R_μ^1 arises as an unwanted term with no analytical correspondence. It is therefore essential to set the transport coefficients in the diffusive regime precisely to $\beta_{i,k'} = 1/2$. This is the case with the new definition (37). With this choice, we immediately find $R_a^1 = 0$. Also R_μ^1

vanishes because the term under the sum over j becomes antisymmetric with $\gamma_{i',k'} = \beta_{i',k'} = 1/2$. For the next step, we need a more concise notation for differences and averages of a zone edge centered variable V :

$$\begin{aligned} d(V)_{i'} &= V_{i+1} - V_i \\ (V)_{i'} &= \frac{1}{2} (V_{i+1} + V_i). \end{aligned}$$

For zone center oriented variables, we use the analogous definitions, e.g. $d(\alpha\rho\psi_{k'}^0)_i = \alpha_{i'}\rho_{i'}\psi_{i',k'}^0 - \alpha_{i'-1}\rho_{i'-1}\psi_{i'-1,k'}^0$. With this, we may rewrite the terms R_a^0 and R_μ^0 as

$$\begin{aligned} R_a^0 &= \frac{d(4\pi r^2)_{i'}}{da_{i'}} \rho_{i'} \psi_{i',k'}^0 + \frac{4\pi}{da_{i'}} \frac{1}{2\alpha_{i'}} \left[r_{i+1}^2 d(\alpha\rho\psi_{k'}^0)_{i+1} + r_i^2 d(\alpha\rho\psi_{k'}^0)_i \right] \\ R_\mu^0 &= - \left(\Gamma_{i+1} \frac{3d(r^2)_{i'}}{2d(r^3)_{i'}} - G_{i+1}^\mu \right) 2\psi_{i',k'}^0. \end{aligned} \quad (76)$$

If the hydrodynamics equations relate the rest mass element to the volume element by $\Gamma_{i+1}da_{i'} = (4\pi/3)\rho_{i'}d(r^3)_{i'}$, the first term in R_a^0 cancels with the first term in R_μ^0 . Finally we try to extract the lapse function α from the gradient in the remainder of R_a^0 ,

$$\frac{4\pi}{da_{i'}} \frac{1}{\alpha_{i'}} [r^2 d(\alpha\rho\psi_{k'}^0)]_{i'} = \frac{1}{da_{i'}\alpha_{i'}} [4\pi r^2 (\rho\psi_{k'}^0) d\alpha]_{i'} + \frac{1}{da_{i'}\alpha_{i'}} [4\pi r^2 \alpha d(\rho\psi_{k'}^0)]_{i'},$$

and find for the diffusion limit in the finite difference representation

$$\begin{aligned} R_a'^0 + R_\mu'^0 + R_E^0 &= R_c, \quad \text{with} \\ R_a'^0 &= \frac{1}{\alpha_{i'}da_{i'}} [4\pi r^2 \alpha d(\rho\psi_{k'}^0)]_{i'} \\ R_\mu'^0 &= \frac{1}{\alpha_{i'}da_{i'}} [4\pi r^2 (\rho\psi_{k'}^0) d\alpha]_{i'} + G_{i+1}^\mu 2\psi_{i',k'}^0 \\ R_E^0 &= - \frac{G_{i+1}^E}{E_{k'}^2 dE_{k'}} \left(\frac{dE_{k'-dk}}{E_{k'} - E_{k'-dk}} E_{k'-dk}^3 \psi_{i',k'-dk}^0 - \frac{dE_{k'}}{E_{k'} + dk - E_{k'}} E_{k'}^3 \psi_{i',k'}^0 \right) \\ R_c^1 &= -\chi_{i',k'}(\rho_{i'}, T_{i'}^*, Y_{e,i'}^*) \psi_{i',k'}^1. \end{aligned} \quad (77)$$

If we compare this to the analytical radiation momentum equation in the diffusion limit with $J - 3K = 0$,

$$4\pi r^2 \frac{\partial}{\partial a} (\rho K^N(E)) + 4\pi r^2 \frac{1}{\alpha} \frac{\partial \alpha}{\partial a} \rho J^N(E) - \frac{\Gamma}{\alpha} \frac{\partial \alpha}{\partial r} \frac{\partial}{\partial E} (E^3 K^N(E)) = -\chi H^N(E), \quad (78)$$

we can identify the physical meaning of all remaining terms. The diffusive flux ψ^1 appearing in R_c^1 is determined by the opacity χ and operators acting on the particle density. The term in $R_a'^0$ describes the flux generated by a gradient in the particle density. It is the only term that survives in the Newtonian limit. In full general relativity, we have an additional gravitational force acting on the radiation particles. It contributes to the particle flux and is described in the term $R_\mu'^0$.

Its analytical analogue is $R_\mu'^0 = 3(\Gamma/\alpha)(\partial\alpha/\partial r)\psi^0$. The factor of three stems from our choice $3\psi^0 = 3K = J$.

The term R_E^0 , corrects for the fact that the gradient in $R_a'^0$ has been taken at constant local particle energy instead of constant particle energy at infinity. The terms $R_a'^0$ and R_c^1 emanate in a perfect way from our finite difference representation because of the special measures taken in the finite difference representation of the propagation terms D_a and D_μ in (Mezzacappa & Bruenn 1993a). However, the requirement of reasonable global energy conservation ties the finite difference representation of this basic choice to many other terms, as it has been outlined in table (30). These constraints impose a rather obscure finite differencing in the diffusive limit for the general relativistic corrections $R_\mu'^0$ and R_E^0 . However, one still recognizes each term as a finite difference representation of a physical term. If we integrate the corrections over energy, the contributions from R_E^0 are guaranteed to vanish. We therefore focus on the impact of the remaining correction $R_\mu'^0$ in our simulations. In order to ensure a vanishing flux in equilibrium, it remains to be shown that the results from our finite difference representation don't significantly deviate from a natural finite difference representation of Eq. (78), which becomes after an integration over energy,

$$\frac{4\pi r^2}{\alpha^3} \frac{\partial}{\partial a} (\alpha^3 \rho K^N) = -\chi H^N. \quad (79)$$

To this purpose, we collect from Eq. (77) the finite difference representations

$$\begin{aligned} \frac{\rho_{i'}}{\Gamma_{i+1}} dr_{i'} R_a'^0 &= \frac{3}{4\pi (r_{i+1}^2 + r_{i+1}r_i + r_i^3) \alpha_{i'}} [4\pi r^2 \alpha d(\rho\psi^0)]_{i'} \\ \frac{\rho_{i'}}{\Gamma_{i+1}} dr_{i'} R_\mu'^0 &= \frac{3}{4\pi (r_{i+1}^2 + r_{i+1}r_i + r_i^3) \alpha_{i'}} [4\pi r^2 (\rho\psi^0) d\alpha]_{i'} \\ &+ (r_{i+1} - r_i) G_{i+1}^\mu 2 \frac{\rho_{i'} \psi_{i'}^0}{\Gamma_{i+1}} \end{aligned} \quad (80)$$

and compare their sum with the natural finite difference representation

$$\frac{1}{\alpha_i^3} d(\alpha^3 \rho \psi_{k'}^0)_i \quad (81)$$

of Eq. (79). The comparison is performed in a time slice in the evolution of the $40 M_\odot$ progenitor of (Woosley & Weaver 1995) at 400 ms after bounce. We force the hydrodynamics to be static and evaluate the finite difference expressions (80) and (81) in the high density region, where the diffusion limit is valid and gravitational terms sizeable.

We find in Figure (9) that the terms derived from $R_a'^0$ (dashed line) and $R_\mu'^0$ (dash-dotted line) compose a sum (solid line) that agrees well with the source of the diffusive flux given by the more natural finite difference representation (81). Thus, we conclude that the opacities safely determine the diffusive flux in our finite difference representation of the Boltzmann equation.

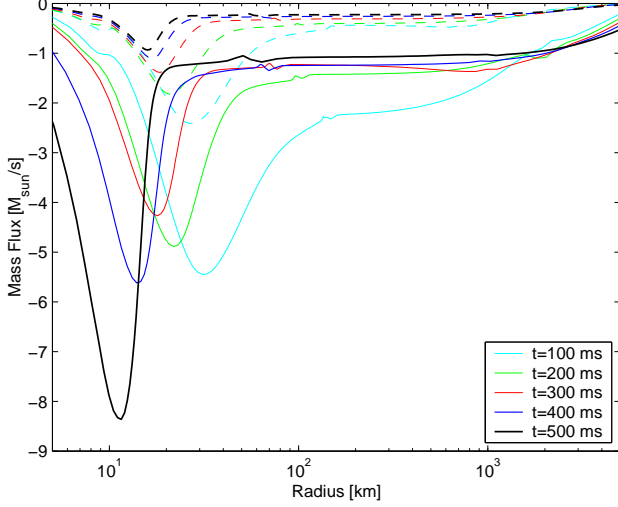


Fig. 8.— Mass flux in the $13 M_{\odot}$ (dashed lines) and $40 M_{\odot}$ (solid lines) simulations. While the smaller star steadily accretes onto a quite incompressible inner core, the larger progenitor changes its qualitative behaviour at 300 ms after bounce and accelerates hydrostatic compactification.

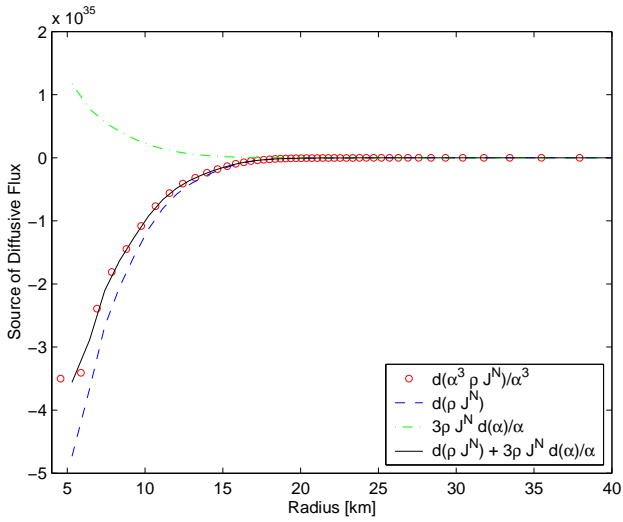


Fig. 9.— We demonstrate in this Figure the accuracy of our diffusion limit. The dashed line is a natural finite difference representation of the diffusive flux in the Newtonian limit. The dash-dotted line represents the general relativistic corrections in our code. The sum of both is shown as a solid line. It coincides very well with the circles which represent a natural finite difference representation of the general relativistic diffusion flux.

5.2. Redshift, light bending, and the evolution of angular moments

In this section we test free streaming in spherically symmetric geometry. This is the opposite limit to the diffusion investigated in the previous paragraph. For the time being, we stay with our stationary time slice at 400 ms after bounce, but focus on radii larger than 40 km. Outside this radius, we switch off all interactions between the radiation field and matter. This facilitates the comparison of the neutrino density, neutrino number flux, and neutrino luminosity with the expected behaviour. Unlike in the Newtonian limit, they are subject to time lapse, gravitational frequency shift, and light bending.

For a stationary neutrino flux in the free streaming limit, we derive from Eq. (23) the particle number conservation

$$\frac{\partial}{\partial a} [4\pi r^2 \alpha \rho H^N] = 0. \quad (82)$$

Figure (10) shows the radial dependence of the locally observed neutrino flux $4\pi r^2 \rho H^N$ (dashed line) and the conserved flux $4\pi r^2 \alpha \rho H^N$ (solid line). We find that the latter is constant to machine precision as required by Eq. (82). This is the direct result of our finite differencing of the term D_a , because we have placed the lapse function α inside the space derivative. The lapse function in the bracket converts the locally advected particle number per proper time to the particle advection per global coordinate time. The gravitational frequency shift enters the analogous equation (28) for the particle energy in form of a further lapse function inside the space derivative,

$$\frac{\partial}{\partial a} [4\pi r^2 \alpha^2 \rho H] = 0. \quad (83)$$

Figure (11) shows the radial dependence of the locally observed luminosity $4\pi r^2 \rho H$ (dashed line), the luminosity with the time lapse correction only, $4\pi r^2 \alpha \rho H$ (dash-dotted line), and the conserved luminosity, $4\pi r^2 \alpha^2 \rho H$, with included gravitational redshift. We see again, that the latter is fairly constant in the interaction free region. Unlike the number flux, the conservation of luminosity is not automatically fulfilled by the finite difference representation, and small deviations can be observed. As the local mean energies of the moving particles are determined by the ratio of energy and number flux, we may conclude from the fulfillment of Eqs. (82) and (83) that the gravitational energy shift of the particles is appropriately taken care of.

In order to fully constrain the redshift, light bending, and evolution of the angular moments, we need to test the radial dependence of a third quantity. Most appropriate is the particle number density. However, some special care is necessary to clearly separate the three effects of (i) gravitational light bending, (ii) the effect of geometric light bending in our spherically symmetric coordinates, and (iii) the numerical light bending caused by limited angular resolution in our finite difference method. We find an analytical derivation of the radial dependence of the particle density by applying the operator $\int dE d\mu E^2 \mu^{-1}$ to the interaction free stationary state limit of the

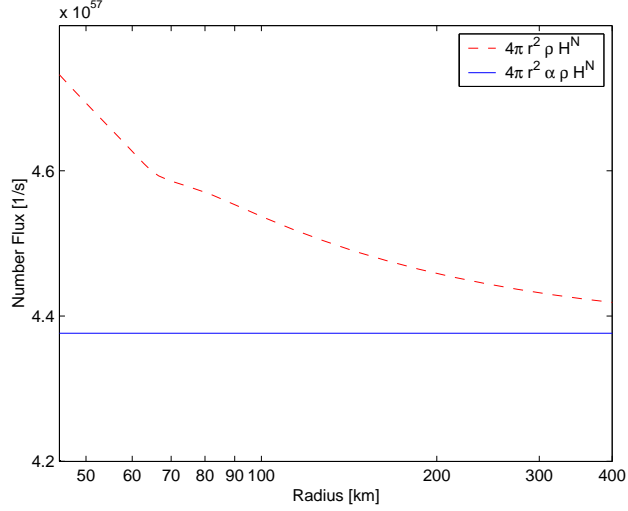


Fig. 10.— We demonstrate in this figure the constancy of the number flux through spheres in free propagation (solid line). The dashed line shows the number flux in the fluid restframe.

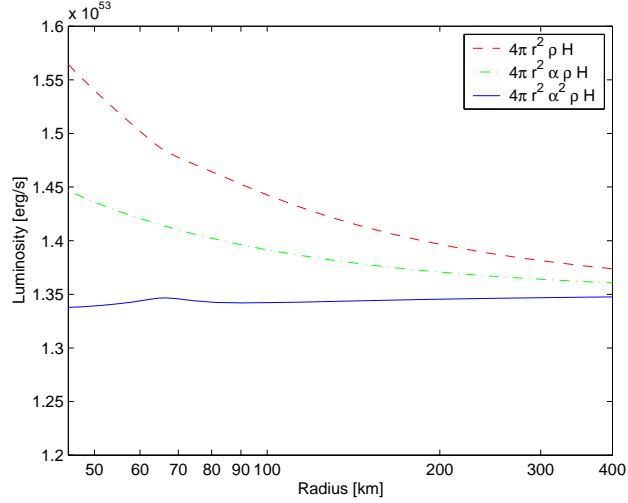


Fig. 11.— We demonstrate in this figure the constancy of the energy flux through spheres in free propagation (solid line). The dashed line shows the energy flux in the fluid restframe. The dash-dotted line shows the conserved number flux weighed with local particle energies. Only the consideration of the additional redshift of the local particle energies leads to the constant solid line.

Boltzmann equation (15),

$$\begin{aligned} \frac{\partial}{\partial a} (4\pi r^2 \alpha \rho J^N) + \Gamma \left(\frac{1}{r} - \frac{1}{\alpha} \frac{\partial \alpha}{\partial r} \right) \times \\ \left(4 \int F(\mu = 0) E^2 dE - \int [F - F(\mu = 0)] E^2 dE \frac{1 - \mu^2}{\mu^2} d\mu \right) = 0. \end{aligned} \quad (84)$$

As before, we may compare this to our finite difference representation. The application of the operator $\sum dE_{k'} w_{j'} E_{k'}^2 \mu_{j'}^{-1}$ to the finite difference representation of the Boltzmann equation leads to

$$\begin{aligned} (4\pi r_{i+1}^2 \alpha_{i+1} \rho_{i+1} J_{i+1}^N - 4\pi r_i^2 \alpha_i \rho_i J_i^N) = \\ -\alpha_{i'} \Upsilon_{i+1} \sum F_{i',j,k'} d\alpha_{i'} E_{k'}^2 dE_{k'} \frac{\zeta_j}{\mu_{j'} \mu_{j'-1}} (\mu_{j'} - \mu_{j'-1}). \end{aligned} \quad (85)$$

Here, $\alpha_i \rho_i J_i^N$ is interpolated according to Eq. (39) and $F_{i',j,k'}$ according to Eq. (44). Figure (12) compares the left hand side of Eq. (85) to the right hand side, evaluated in our 400 ms post bounce time slice. As expected, the match is to machine precision. In this computer representation, we can clearly distinguish the small effect of gravitational light bending, proportional to $(\Gamma/\alpha)(\partial\alpha/\partial r)$, from the much larger geometric effect, proportional to $\alpha\Gamma/r$. However, the main inaccuracy of the particle density in our finite difference representation stems from the fact that the sum over angles on the right hand side of the finite difference Eq. (85) is a poor representation of the angle integral in the analytical Eq. (84). This can be seen in Fig. (12), where we additionally show (cross markers) the evaluation of the more natural Gaussian quadrature of the integral according to

$$-\alpha_{i'} \Upsilon_{i+1} \left(4 \sum F(0)_{i',k'} E_{k'}^2 dE_{k'} - \sum [F_{i',j',k'} - F(0)_{i',k'}] d\alpha_{i'} E_{k'}^2 dE_{k'} \frac{1 - \mu_{j'}^2}{\mu_{j'}^2} w_{j'} \right) \quad (86)$$

The result of Eq. (86) depends quite sensitively on the choice of the distribution function in the tangential direction. For simplicity we use the maximum entropy model in angle space,

$$F_{j'} = A \exp(B \mu_{j'}), \quad (87)$$

for Boltzmann statistics (see e.g. (Smit, van den Horn, & Bludman 2000) for an overview on maximum entropy closures). The zeroth and second moments of Eq. (87) define the flux factor, $h = H/J$, as a function of the parameters A and B ,

$$\begin{aligned} J &= \frac{2A}{B} \sinh(B) \\ h &= \coth(B) - \frac{1}{B}, \end{aligned} \quad (88)$$

Here, we derive the free parameters A and B by inversion of Eq. (88) from the numerically evaluated zeroth and first angular moments of the numerical neutrino distribution function and define $F(0)_{i',k'} = A_{i',k'}$. In Fig. (12) we observe comparable values between the two finite difference

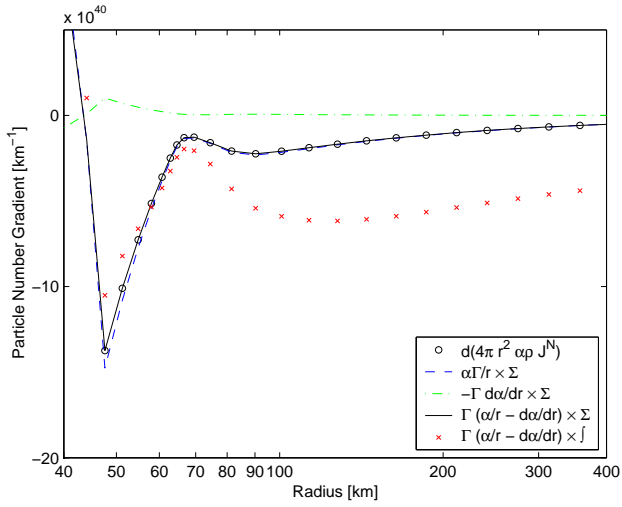


Fig. 12.— This figure shows the radial dependence of the particle number density. In free streaming, it depends on the angular distribution of the radiation field. The dashed line shows the geometric contribution to the gradient and the dash-dotted line the contribution from gravitational light bending. The sum (solid line) representing the left hand side of Eq. (85) exactly matches the right hand side (circles), indicating correct derivations and implementation. The main uncertainty is found in the numerical representation of the angle integral on the right hand side. The expected solution is indicated in the Figure with crosses.

representations (85) and (86) at smaller radius, where the flux factor is smaller (~ 0.75). Large differences are found at larger radii, where the flux factor would be expected to be close to one. In order to study this discrepancy in more detail, we apply the two finite difference expressions to the analytical angular distribution function given by Eq. (87). Different choices of the parameter B define the extent to which the radiation field is forward peaked, i.e. the flux factor. The integral in Eq. (84) evaluates to

$$\begin{aligned} \frac{A}{J} \int_{-1}^1 \frac{1}{\mu} \frac{\partial}{\partial \mu} [(1 - \mu^2) \exp(B\mu)] d\mu &= \\ -2 - Bh + \frac{B^2}{\sinh(B)} \left(B + \frac{B^3}{3 \cdot 3!} + \frac{B^5}{5 \cdot 5!} + \frac{B^7}{7 \cdot 7!} + \dots \right). \end{aligned} \quad (89)$$

We can now directly apply our finite differencing of the integral in Eq. (85) and compare with the analytical result. The comparison is shown in Table (2) for different flux factors and angular resolutions. We find quite poor convergence for the evaluation of the integral as it emerges from the finite differencing in the Boltzmann equation. The comparison with the center block, where no upwind differencing was used for the advection terms, demonstrates that the advective terms play a major rôle in the accuracy of the representation of this integral. A forward peaked radiation field shows a steep gradient in the angular distribution. The choice of upwind differencing always picks a smaller advective flux than at the edge of the angular zone. This is necessary for the stability of the scheme for arbitrary large time steps. The underestimation of the integral can therefore be substantial. The most populated forward bin, for example, never contributes to the integral. The distribution function asymptotically approaches a highly populated forward bin while all other angular bins are emptied. This corresponds to a maximum flux factor that is smaller than one. Although higher angular resolution improves the situation, it does not eliminate this systematic and method-inherent effect. The choice of a higher order advection scheme in angular space might be promising. More rigorous, however, appears the implementation of an adaptive angular grid in the transparent regime. It would be designed to minimize the advective flow in angle space such that the undesired effects are eliminated at the root. An independent and much smaller source of inaccuracy stems from the fact that the integral in Eq. (85) is not written as a sum over a function evaluated at Gaussian quadrature points and multiplied with Gaussian weights. Hence, it does not take profit from the fast convergence of Gaussian quadrature. This can be seen if the result is compared with the evaluation based on the Gaussian quadrature as given in Eq. (86).

In our supernova application, however, convergence tests have shown that 6 angle Gaussian quadrature produces physically reasonable results (Messer et al. 1998; Messer 2000). In the regions of free streaming, where angular diffusion becomes apparent, the neutrino field is already decoupled from the matter and does not influence the dynamical evolution anymore. This is certainly true with the failed explosions we have analyzed so far, given that a low angular resolution causes optimistic neutrino heating. Nevertheless, the use of higher resolution is desirable. The deeper cause that the dependence of the physical results on angular resolution is not as large as it could be expected from the above tests may lay in the broad region of emission across the cooling region.

	B	flux factor	j=6	j=12	j=48	analytical
Eq. (85)	0	0	-2.00	-2.00	-2.00	-2.00
	1	0.31	-1.10	-1.23	-1.36	-1.41
	2	0.54	-0.21	-0.22	-0.28	-0.32
	5	0.80	0.28	0.47	0.68	0.77
	10	0.90	0.06	0.14	0.26	0.31
Eq. (85),	0	0	-2.00	-2.00	-2.00	-2.00
but no	1	0.31	-1.48	-1.43	-1.41	-1.41
upwind	2	0.54	-0.47	-0.36	-0.32	-0.32
diff.	5	0.80	0.66	0.74	0.77	0.77
	10	0.90	0.27	0.30	0.31	0.31
Eq. (86)	0	0	-2.00	-2.00	-2.00	-2.00
	1	0.31	-1.41	-1.41	-1.41	-1.41
	2	0.54	-0.32	-0.32	-0.32	-0.32
	5	0.80	0.77	0.77	0.77	0.77
	10	0.90	0.32	0.31	0.31	0.31

Table 2: This table compares the result of the integral on the right hand side of Eq. (84). The uppermost block shows the evaluation with the finite differencing (85) used in the code. The center block shows the same evaluation without upwind differencing for the advected F . The lowermost block shows the evaluation based on the more natural finite difference representation (86). The result is shown for different angular resolutions.

As it is, for example, evident in Fig. (5), the evolution of the flux factor is not given by the geometry of a radiating sphere alone. The continuous admixture of isotropically emitted neutrinos to the scattered flux makes the correct implementation of balanced reactions as important as a geometrically accurate evolution of the flux under free streaming conditions.

5.3. Observer corrections

For the check of the observer corrections, we go back to the original solution at 400 ms after bounce. Both, the neutrino luminosities and rms energies show a discontinuity across the shock front because of the Doppler effect and angular aberration. In the laboratory frame of a distant observer, however, the radiation field should not be affected by the shock. We may therefore test the implementation of the observer corrections by transforming, for example, the electron neutrino luminosity and rms energy from our comoving frame to the rest frame. In (Liebendörfer, Mezzacappa, & Thielemann 2001) we determined for the particle propagation angle, μ^S , and particle energy, E^S , in Schwarzschild coordinates with $\Gamma^S = (1 - 2m/r)^{1/2}$ the relationship

$$\begin{aligned} (1 - \mu^{S2}) (\Gamma^S)^{-2} &= (1 - \mu^2) (\Gamma + u\mu)^{-2} \\ \Gamma^S E^S &= (\Gamma + u\mu) E. \end{aligned} \quad (90)$$

Assuming free outwards streaming with transport coefficients $\beta = 1$ in the interesting region around the shock, we evaluate for the luminosity, L^S , and rms energy, $\langle E^S \rangle$, the finite difference expression

$$\begin{aligned} L_i^S &= 4\pi r_i^2 \frac{2\pi}{(hc)^3} \sum_{j,k} \rho_{i'-1} F_{i'-1,j,k} E_{i,j',k'}^S E_{k'}^2 dE_{k'} \mu_{i',j'}^S c w_{j'} \\ \langle E^S \rangle_{i'} &= \left(\sum_{j,k} (E_{i,j',k'}^S)^2 F_{i',j',k'} E_{k'}^2 dE_{k'} w_{j'} \right)^{\frac{1}{2}} \left(\sum_{j,k} F_{i',j',k'} E_{k'}^2 dE_{k'} w_{j'} \right)^{-\frac{1}{2}}. \end{aligned} \quad (91)$$

The result is shown in Figure (13). The solid line is the luminosity in the rest frame according to Eq. (91). The dotted line shows the luminosity in the comoving frame for comparison. We find that the luminosity profile shows a numerical local distortion on top of the shock front. However, if we compare the left hand side values with the right hand side values, we find the expected disappearance of the discontinuity, indicating that the observer corrections in the comoving frame are well represented. The same behaviour can be seen in the rms energies. The latter tests the frequency shift, while the luminosity additionally depends on the angular aberration. The bump in the quantities on the shock front may be due to advection on the adaptive grid, it does not have non-local consequences.

5.4. Radiation pulse propagation

The observer corrections discussed so far describe the influence of the hydrodynamical motion on the observation of the radiation field in the fluid rest frame. In this section, we check the dynamics of the radiation field itself. The neutrino transport in the supernova is most dynamic when the shock crosses the neutrinosphere. As soon as neutrinos start to emanate from the hot shocked matter as a consequence of the decreased opacity, immediate electron capture can occur to refill the emptied phase space with new electron neutrinos. A neutrino burst carries an energy of order 10^{51} erg throughout the star towards the distant observer. Although the neutrino burst is not completely interaction free, it is an excellent example for a time-dependent radiation field where the pulse propagation speed can be tested. We do this by plotting the luminosity at selected times after the launch of the neutrino burst as a function of the radius. We shift the radial coordinate, r , in each time slice by the amount a free massless neutrino would have propagated during the time t since bounce, $r' = r - c * t$. With an ideal numerical solution to free propagation, we would expect congruent pulse shapes from each time slice at the same positions r' . Figure (14) shows the neutrino burst with the described radius adjustment in the evolution of the $40 M_{\odot}$ progenitor. We first observe, that the position of the pulse is fairly stationary. There is a well-defined point at about half the peak height where all rising luminosity slopes coincide. This is the point which travels exactly with speed of light through the star. However, we also observe that the shape of the pulse is not stationary. The pulse is considerably broadened with ongoing time. From the check of the neutrino flux conservation in Fig. (10), we already know that the number and energy of the emitted neutrinos is conserved during their propagation to larger radii. The broadening is likely to occur by artificial diffusion in our numerical finite differencing scheme. Indeed, from considerations in (Liebendörfer, Rosswog & Thielemann 2002) we remember that first order upwind differencing introduces a numerical diffusivity proportional to the advection speed and zone width,

$$D_{i'} = cdr_{i'}. \quad (92)$$

We determine the influence of this effect to the evolution of our neutrino pulse by approximating the diffusion between the time steps with $\Delta L \simeq D (\partial^2 L / \partial r^2) \Delta t$. At the pulse peak in a time slice, we evaluate the diffusivity (92) and the second derivative of the luminosity. The time span Δt to the next time slice gives us an estimate ΔL for the change of the peak luminosity. We subtract ΔL from the pulse height and draw at this estimated peak level for the next time slice a horizontal line on the right hand side in Fig. (14). The close to perfect agreement with the numerically evolved pulse height leads to the conclusion that the diffusivity (92) introduced with the low order advection scheme fully accounts for the observed pulse broadening.

5.5. Energy conservation analysis

In Fig. (15) we show the contribution of the space-integrated terms in Eq. (25) to the energy conservation. Leading in the graph is the energy generation from the collision term C_c^1 . At the very

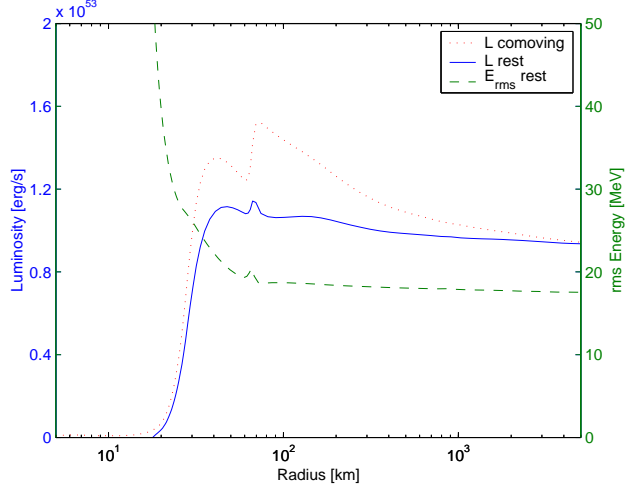


Fig. 13.— For this Figure, we have transformed the electron neutrino luminosity and the rms energy to the laboratory frame, where these quantities are expected to be continuous across the shock front. This tests frequency shift and angular aberration.

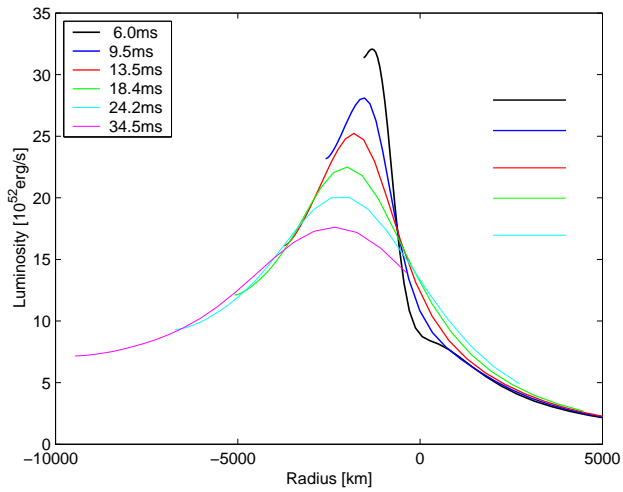


Fig. 14.— We demonstrate that the neutrino burst propagates with speed of light. The levels on the right hand side in the graph give estimates of the decaying peak height based on numerical diffusion from first order upwind differencing. They accurately explain the decay observed in the numerically propagated luminosity peak.

beginning of the simulation, this contribution is balanced by the generation of the initial neutrino field, i.e. by C_t^1 , which describes the time derivative of the space integrated neutrino energy. As soon as the field is established, the energy generation is balanced by the propagation term D_a^1 that counts the energy loss by neutrino emission at the surface. When the matter becomes more dense, just before bounce, we observe another steep rise in C_t^1 that indicates that the neutrinos become trapped and remain in the star until shock breakout. The energy generation is balanced by the increase of the energy of the neutrino field at this time. When the shock crosses the neutrino spheres, the neutrino burst becomes manifest in the reduction of the neutrino energy growth rate C_t^1 . From then on, the emission term D_a^1 balances the main energy generation by neutrino production. Also shown are the $O(v/c)$ contributions C_c^2 , C_t^3 , D_a^3 , and the gravitational coupling R_1 between the energy flux of the neutrino field and the energy density of the matter.

In Fig. (16) we demonstrate the importance of the $O(v/c)$ cancellations ($D_a^4 O_E^1$) and ($D_\mu^{12} O_E^{34}$). We have also included the drift in total energy conservation (left triangles) as a function of time. The two orders of magnitude difference between these lines make clear that the finite difference representation of D_a^4 , O_E^1 , D_μ^{12} , and O_E^{34} has to be chosen with care to allow proper cancellation and energy conservation. Also shown is the size of the higher order cancelling terms ($O_E^2 O_\mu^2$) and ($O_E^{56} O_\mu^{34}$) that are less important for total energy conservation.

In Fig. (17) the gravitational terms are presented that are within limits subject to matching for cancellation. For example the terms ($C_t^2 D_\mu^{34} D_E^2$) have comparable size and are supposed to add up to zero. In our scheme, they do so in the hydrodynamic limit and to the accuracy given by Eq. (47). We can read from the graph, that this cancellation becomes more important at later times when the protoneutron star becomes very dense. The hydrodynamic limit is a good approximation for the radiation field under these highly opaque conditions. Almost an order of magnitude larger are the terms D_a^2 and D_E^1 that essentially balance each other. The remaining difference is filled by the contribution of R_1 , O_μ^1 , and C_t^4 . Note the sizable contributions of the redshift, D_E^1 , and the gravitational matter-radiation coupling, R_1 , before bounce. In the $O(v/c)$ limit, none of them is present, while they demonstrate mutual cancellation in the general relativistic case.

The absolute necessity of accurate energy conservation may be discussed. However, it has shown to provide an invaluable check for the congruence between the programmers intention and the code implementation of the many intricate finite difference expressions.

5.6. Comparison with Multi-Group Flux-Limited Diffusion

Following our tradition (Mezzacappa & Bruenn 1993a,c), we conclude this paper with a comparison to simulations using the Multi-Group Flux-Limited Diffusion (MGFLD) approximation. We note that, excepting the pioneering Boltzmann solver of (Wilson 1971), codes with MGFLD currently provide the only alternative numerical data for the evolution of a supernova in full general relativity (Myra et al 1987; Schinder & Bludman 1989; Bruenn, DeNisco, & Mezzacappa 2001).

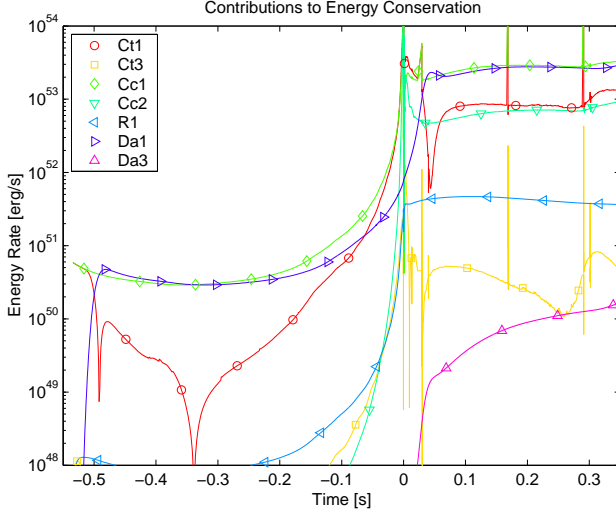


Fig. 15.— We plot absolute values of different energy terms in Eq. (30). We show the time derivatives, the collision term, and the main spatial propagation terms.

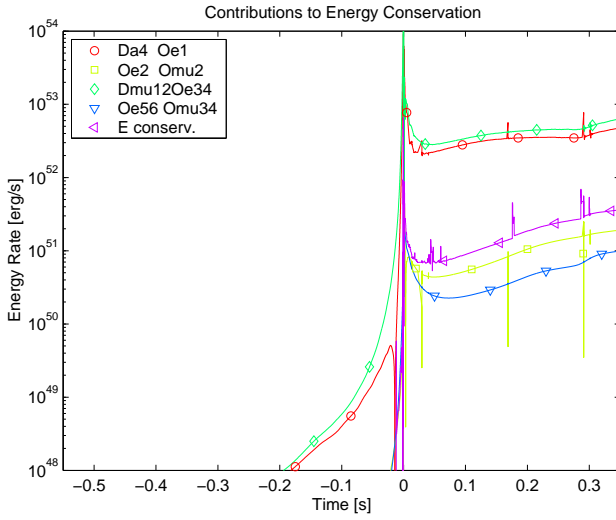


Fig. 16.— We plot absolute values of different energy terms in Eq. (30). We show a selection of propagation and observer corrections and the numerical drift in the total energy if a full energy balance, including radiation and work at the surface of the computational domain, is evaluated.

We compare the evolution of a $13 M_{\odot}$ progenitor (Nomoto & Hashimoto 1988). This is a stellar model with a small iron core which has been used throughout the supernova literature in the hope of seeing an explosion in numerical simulations. Questions have arisen concerning the accuracy of MGFLD in the dynamic semi-transparent region between the neutrino sphere and the heating region (Janka 1992; Messer et al. 1998; Yamada, Janka, & Suzuki 1999). Because the dynamics is very sensitive to neutrino emission, and because the energy deposition in the heating region reaches the order of explosion energies per second as demonstrated in Fig. (18), accurate neutrino transport is an important ingredient to realistic supernova simulations. Our testing supports the applicability of MGFLD, based on a recently developed general relativistic code incorporating a sophisticated flux limiter (Bruenn et al. 2002), in spherically symmetric supernova simulations. The two compared codes with Boltzmann neutrino transport and MGFLD approximation implement different hydrodynamics methods with different adaptive grid techniques.

We start with the comparison of a time slice at bounce in Figure (19). The ordinates of graphs (a-h) display the enclosed mass. At the end of core collapse, we find similar density profiles in graph (b), very similar deleptonization in the electron abundance (d), and comparable luminosities in graph (e). The central entropy in graph (c) coincides nicely in both codes. This leads to agreement in the temperature (f) in a region where the temperature very sensitively depends on the internal energy evolution because of electron and neutron degeneracy. The MGFLD code predicts slightly hotter material in the mass range $0.6 - 1 M_{\odot}$. This is most probably due to differences in the initial configuration or the treatment of hydrodynamics. At lower densities than $\sim 10^{10} \text{ g/cm}^3$, the dominant source of neutrinos is provided by electron capture on heavy nuclei. As the mass fraction of heavy nuclei is not very temperature dependent, the entropy difference only affects the deleptonization directly by the dependence of the electron capture rates. AGILE-BOLTZTRAN finds a slightly lower electron abundance in this regime. At densities exceeding $\sim 10^{10} \text{ g/cm}^3$, electron capture on free protons dominates because of the shell closure in the oversimplified independent particle model for electron capture on nuclei used in both models. The lower entropy in the simulation with AGILE-BOLTZTRAN leads to a smaller mass fraction of free protons and reduced deleptonization with respect to the MGFLD simulation. The slightly larger electron abundance between 0.65 and $0.8 M_{\odot}$ is a consequence. The shock formation at bounce occurs at similar positions (Fig. (19a)) in both runs. This is a consequence of the identical thermodynamical state within the homologous inner core up to the sonic point at an enclosed mass of $\sim 0.54 M_{\odot}$. Also in close agreement are, as expected, the rms energies of the neutrinos where they are in thermal equilibrium with the inner core (Fig. (19h)). Differences outside an enclosed mass of $1.2 M_{\odot}$ reflect the different treatment of the interface between the silicon layer and the iron core in nuclear statistical equilibrium. The mean flux factor as the ratio of neutrino flux over neutrino density, $F = H/(cJ)$, in graph (g) shows differences. The smaller flux factor of the MGFLD neutrinos $\sim 0.8 M_{\odot}$ is due to increased isotropic neutrino emission at the higher entropy. It leads to slightly higher luminosities and higher rms energies, and is consistent with the smaller electron fraction. As the gradient of the luminosity reflects neutrino emission, we may also conclude from graph (e) that the emission is larger in MGFLD where electron capture on protons dominates and smaller where

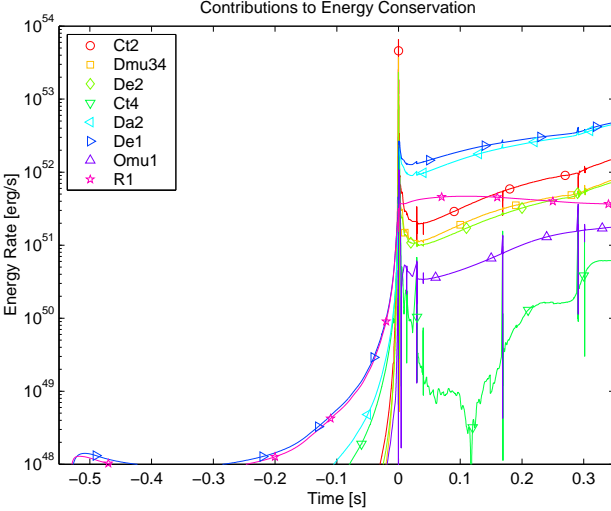


Fig. 17.— We plot absolute values of different energy terms in Eq. (30). We show a selection of propagation and observer corrections and the coupling term between radiation and matter.

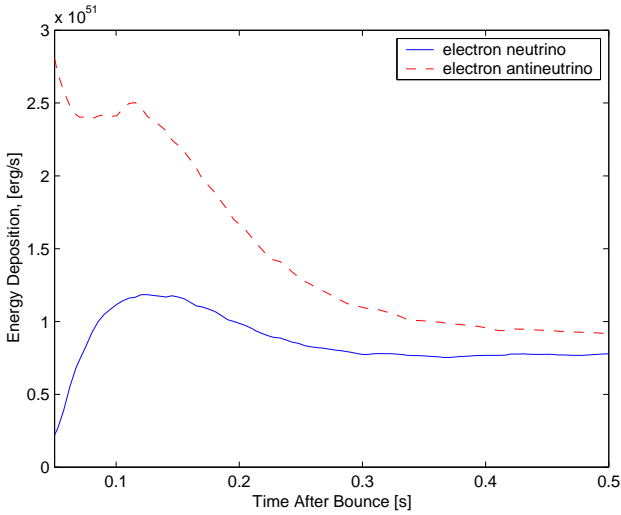


Fig. 18.— The net energy transfer from neutrinos to matter above the gain radius is shown. Note the significant dominance of heating by electron antineutrinos. As demonstrated with more detailed emission and absorption rates in (Liebendörfer et al. 2001), the electron chemical potential ~ 4 MeV in the heating region balances electron neutrino absorption to a larger extent by electron capture than antineutrino absorption by positron capture.

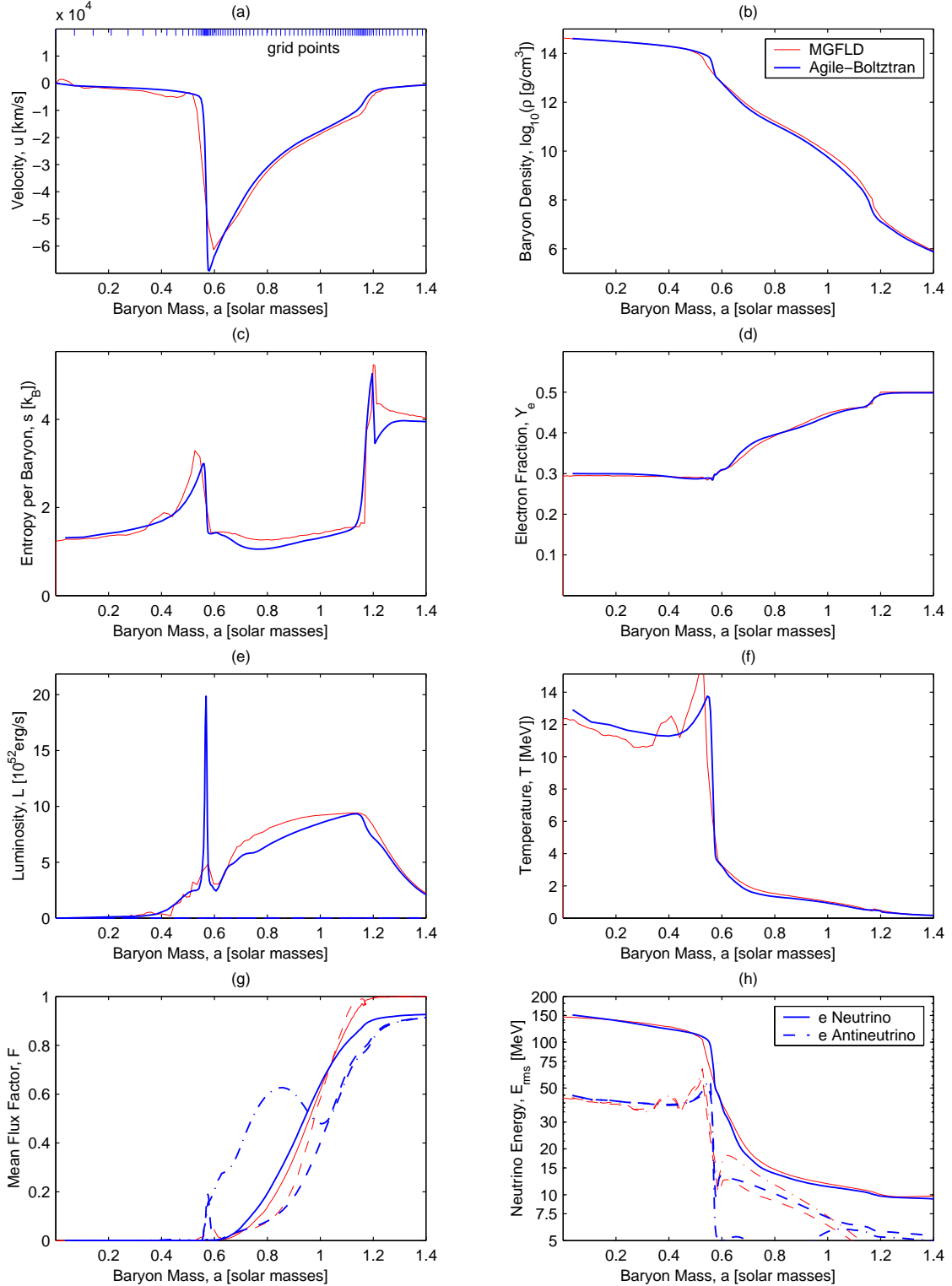


Fig. 19.— At bounce.

electron capture on heavy nuclei is active. The smaller flux factor in AGILE-BOLTZTRAN outside $1.1 M_{\odot}$ stems from the limited angular resolution discussed in section (5.2). It is systematic and visible in all the following figures. Its impact on the dynamics, however, is negligible because of the small coupling between the neutrino flux and matter at large radii.

Figure (20) shows a time slice just after the launch of the neutrino burst. This is the most dynamical phase in the radiation transport. In the luminosity graph (e), we observe a neutrino burst in both codes. The luminosity peak in AGILE-BOLTZTRAN is broader and smaller because of numerical diffusion as analyzed in section 5.4. The MGFLD burst changes its shape more slowly because the MGFLD code reverts, in the transparent regime, to centered difference advection (rather than first order upwind) which is second order accurate in space (on a uniform spatial grid). The MGFLD solution develops some noise when the shock ploughs through the high density regime. In AGILE, the dynamical adaptive grid enlarges zones once the shock has passed. This leads to a partial averaging out of the noise and a smoother solution. Note also, that the dynamical adaptive grid does not insert or destroy grid points. At the cost of advective diffusion (Liebendörfer, Rosswog & Thielemann 2002) the adaptive grid is no source of noise.

Most important for the success or failure of the supernova explosion in our spherically symmetric simulations is the time ~ 100 ms after bounce. Figure (21) shows the comparison of the two simulations at that time, when the efficiency of the neutrino heating is close to maximum. The agreement of the data in this phase is remarkable. The thermodynamical state of the matter inside the shock is identical. Also identical is the matter infall velocity between the neutrino sphere and the shock position. Since this infall velocity determines the time the infalling matter spends in the heating region before being accreted onto the protoneutron star, its value is essential for the success or failure of the shock revival. The identical thermodynamical state throughout the core allows an independent comparison of the flux factors. We find close agreement for all neutrino flavors. Among the detectable differences in the simulations are a slightly higher diffusive flux in AGILE-BOLTZTRAN at densities close to or above nuclear density and a higher neutrino temperature in the MGFLD simulation for all neutrino flavors between the neutrino sphere and the shock position. As this difference disappears outside the shock radius it might be due to differences in the implementation of the observer corrections. The remaining differences outside the shock radius are dominated by the chosen approximation for silicon burning and the angular resolution limitation in AGILE-BOLTZTRAN.

Similar agreements and differences are found in a later stage of the quasistationary phase, e.g. at 400 ms after bounce (Fig. (22)). We find again hotter neutrinos between the neutrino sphere and the shock position in the MGFLD simulation and a larger diffusive flux at very high densities in AGILE-BOLTZTRAN. On a longer time scale, the latter leads to a marginally larger deleptonization visible in the innermost 7 km of the electron fraction profile. A new difference appears in the entropy profile, which might be due, on the one hand, to a different right hand side state in the shock jump conditions as a result from the different treatment of silicon burning, and, on the other hand, also be caused by differences in the hydrodynamical scheme for the solution of the shock jump conditions.

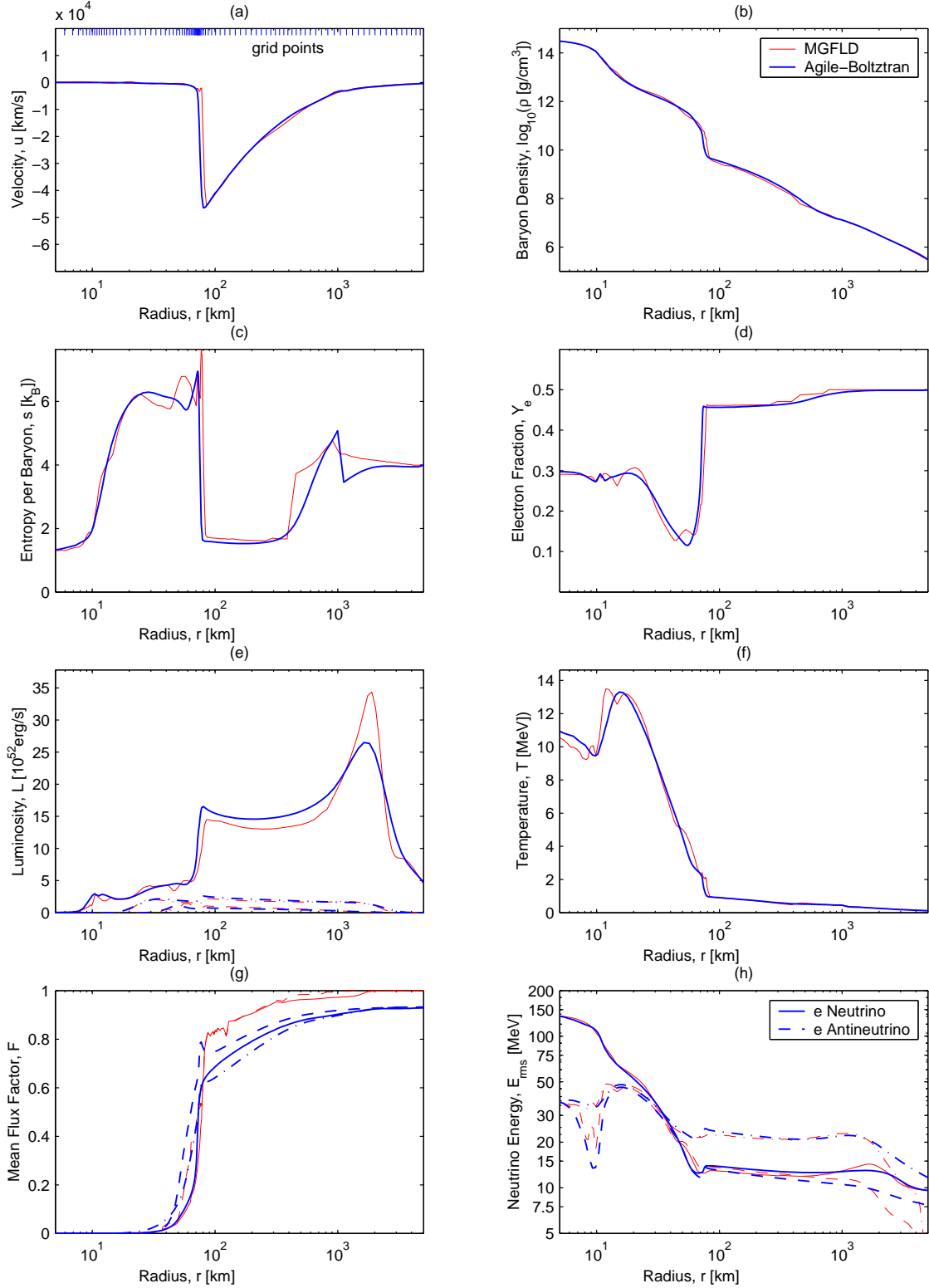


Fig. 20.— 10 ms after bounce.

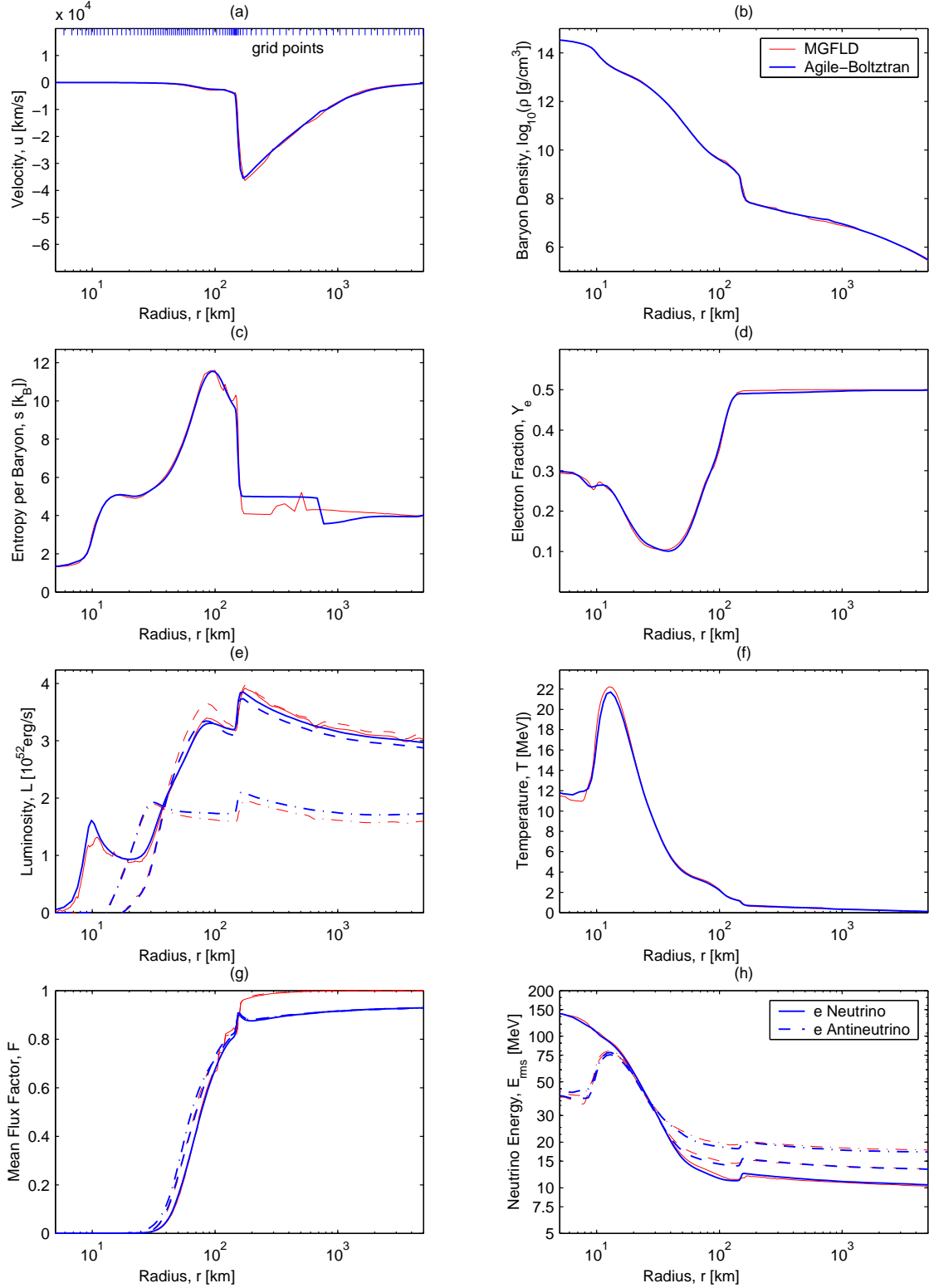


Fig. 21.— 100 ms after bounce.

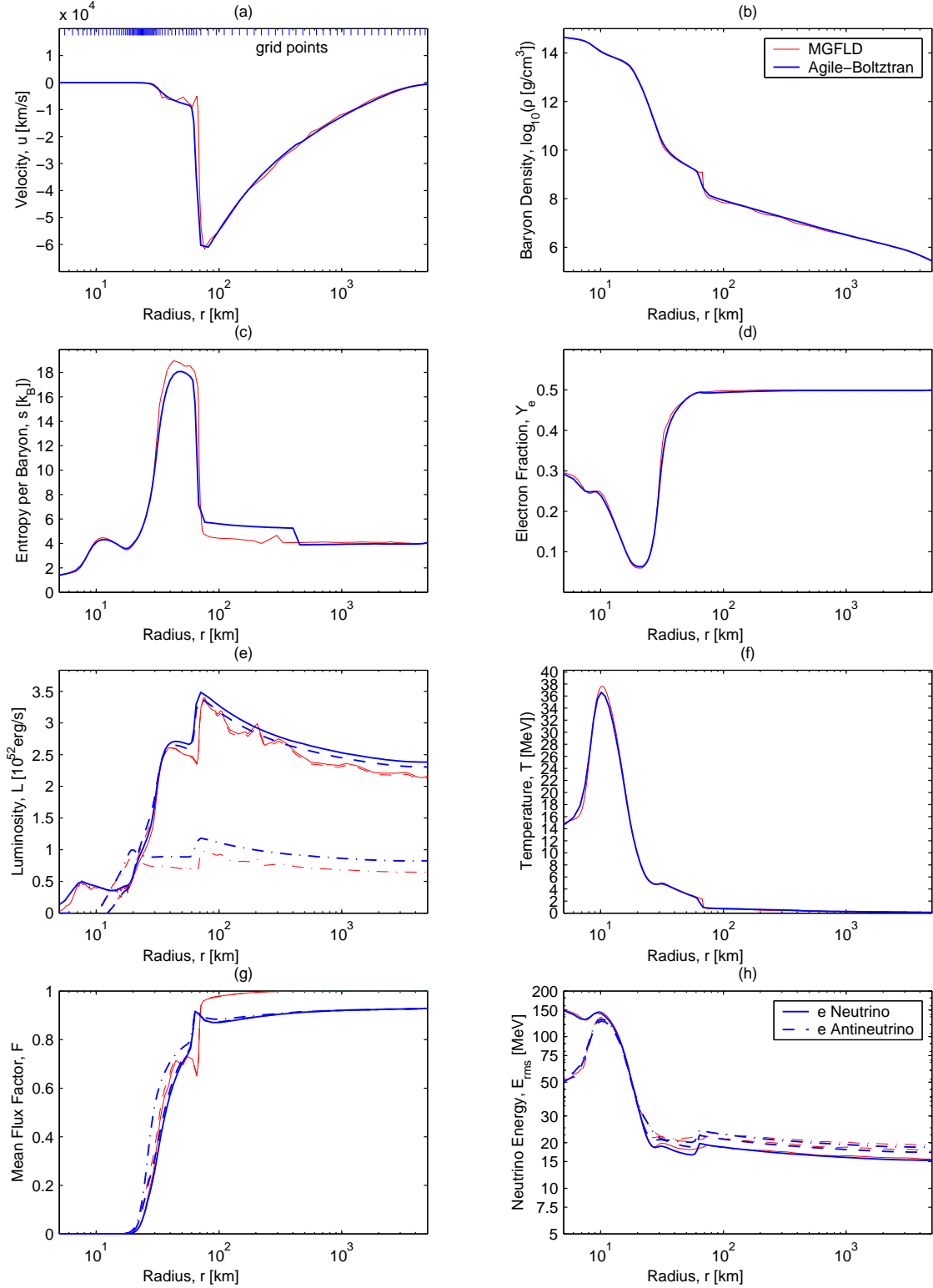


Fig. 22.— 400 ms after bounce.

We also remark that the mean flux factor in the MGFLD scheme shows an artificial sink on the left hand side of the shock while the mean flux factor in AGILE-BOLTZTRAN shows an artificial overshoot on the right hand side of the shock. However, the most significant new difference appears in the luminosity profiles. The small tendency to higher luminosities at smaller neutrino temperatures in AGILE-BOLTZTRAN is difficult to explain because higher luminosities would be expected to go along with higher neutrino temperatures if the emission region were the dominant difference. Here we suggest that energy exchange with the higher entropy and lower density regime in the MGFLD solution between radii of 30 and 60 km influences the neutrino luminosities accordingly. Another possible explanation could be given by differences in the implementation of the observer corrections.

Overall, in our simulations of stellar core collapse and postbounce evolution in spherically symmetric, general relativistic space-time, we find the identical physical evolution in simulations implementing the full Boltzmann transport equation and simulations based on the Multi-Group Flux-Limited Diffusion approximation with a new sophisticated flux limiter. This is especially true in all phases of stationary radiation transport. Differences are limited to small numerical deviations which have to be expected, given that we compare two different methods and computer implementations in the solution of a complex time-dependent physical problem.

6. Conclusion

We document the radiation transport part in our code AGILE-BOLTZTRAN for supernova simulations. AGILE-BOLTZTRAN directly solves the general relativistic Boltzmann transport equation for the specific neutrino distribution function in spherically symmetric space-time. In combination with general relativistic hydrodynamics, we therewith present a detailed and consistent finite differencing for fermion radiation hydrodynamics in spherical symmetry. We test our code in the context of stellar core collapse and postbounce evolution of a smaller $13 M_{\odot}$, and a more massive $40 M_{\odot}$ progenitor star. They embrace the progenitor mass range expected to produce supernova type II explosions.

As outlined in section 1, supernova simulations have to overcome a variety of application-specific challenges to ensure meaningful numerical results. The expected explosion energy is orders of magnitude smaller than individual energy components, such as, e.g. the binding energy of the protoneutron star or the internal energy of the collapsed matter. Moreover, the three neutrino flavors are subject to Fermi statistics, and neutrino number conservation is also important. The request for accurate conservation of global energy is balanced by the need of an accurate representation of internal energies in the form of temperatures, which essentially determine the neutrino-matter interaction cross sections. The full angular information of the neutrino radiation field is important in the broad and neutrino energy dependent semi-transparent regime around the neutrino spheres. It determines the propagation angle and path length of the neutrinos in the heating region, which are produced in the cooling region interior to it or emanate from the protoneutron star. The efficiency of neutrino heating on the infalling shock-dissociated matter is considered to be essential

for the successful shock revival and expulsion of the outer layers in a supernova explosion.

The Boltzmann transport equation plays a fundamental role in kinetic gas theory. One may derive from it the diffusion equation, or even complete hydrodynamics if one drives the limit further to vanishing effective transport. Thermodynamical quantities are simply determined by the expectation values of various operators on the fundamental particle distribution functions. Hence, it is very exciting to numerically solve a single equation for the fundamental particle distribution functions (in an object of astronomical size!) and determine all macroscopically interesting quantities from it by taking the appropriate expectation values in the numerical representation. However, as beautiful the approach is with regard to its concept, it is as intricate when it comes to the detailed finite difference representation of this one Boltzmann equation. In theory, the solution of the Boltzmann equation guarantees the correct behaviour of basic physical laws that can be expressed in terms of derived expectation values, such as, e.g., the conservation of energy or the equation of state for radiation, $p = \rho/3$, Fermi statistics, etc.. This is not automatically the case with a numerically solved Boltzmann equation. Especially in the astrophysical application, basic physical relationships are often more apparent to the distant observer than the detailed microscopic state of the matter and radiation field. The key to the realization of the approach is therefore the search for a justifiable finite difference representation of the microscopic physics such that basic macroscopic principles are accurately met when they are described in terms of finite difference expectation values of operators on the numerical particle distribution function.

To comply with this ambition would not be half as hard if there would not be an additional complication. Physically, the Boltzmann transport equation is a trivial equation, describing free particle propagation on geodesics between independent collisions, even more so in spherical symmetry, where only two independent spatial degrees of freedom have to be considered. However, the supernova has been investigated as a site of interesting nuclear and neutrino physics, mutually coupled through a variety of reactions with neutrino energy and angle dependent cross sections. The evaluation of these cross sections is greatly simplified in the fluid rest frame described by comoving coordinates. Comoving coordinates are also favored by the initial core collapse where the relevant computational domain collapses with the matter from several thousands to some hundreds of kilometer radius, before it hopefully expands again with the explosion. The comoving coordinates convert the simple statement of the Boltzmann equation, that the derivative of the invariant particle distribution function along the phase flow vanishes between collisions, into a complicated sum of partial derivatives along the comoving coordinates. These depend on the fluid motion even for a fully decoupled radiation field. As the macroscopic physical principles we would like to guarantee with a well-chosen finite differencing of the Boltzmann equation are supposed to emerge in the global view of a distant observer, the finite differencing of all comoving frame correction terms have to be adjusted in a mutually dependent way to correctly transform to conservation equations for the observer in a laboratory frame. It has been the focus of this paper to present such a finite difference representation of the Boltzmann transport equation.

AGILE-BOLTZTRAN is an extension of the implicit $O(v/c)$ Boltzmann solver documented in

(Mezzacappa & Bruenn 1993a,b,c), merged with the implicit general relativistic hydrodynamics code described in (Liebendörfer, Rosswog & Thielemann 2002). We endow our finite difference representation with a dynamically adaptive spatial grid to seamlessly follow the propagation of the shock through the outer layers of the infalling material. Our finite difference representation implements all physical terms in spherically symmetric general relativistic radiation hydrodynamics, with the exception of gravitational terms in the coefficients of the Boltzmann equation that are nonlinear in the radiation field. These terms cancel in the evaluation of relevant macroscopic quantities. We ensure particle number conservation to machine precision by construction. The space propagation terms are determined by the requirement of numerical stability in the free streaming limit. The coefficients of the corresponding partial derivatives with respect to radius and propagation angle are set to produce an accurate diffusion limit on top of a large equilibrated background radiation field. Beside of some metric coefficients, the coupling of the radiation transport part to hydrodynamics solely depends on the local collision integral and allows a numerically independent evolution of radiation and matter in a region with negligible opacities. Energy conservation is established with a finite difference representation of the observer corrections that matches the finite difference representation of the already determined propagation terms. This error matching technique leads to machine precision energy conservation in the Newtonian limit when the adaptive grid is switched off. The impact to energy conservation of the adaptive grid does not reach the order of magnitude of a supernova explosion. In the fully general relativistic case, a similar term-matching of all gravitational contributions is required for the long term evolution of massive progenitors if the violation of energy conservation should not exceed the expected explosion energy. In order to perform the simulation over a second or more, radiation transport and hydrodynamics have been implemented with implicit finite differencing. This allows reasonably sized time steps during the neutrino heating phase when the neutrinos deep in the radially hydrostatic protoneutron star find to an equilibrium with matter and when a small diffusive flux adds to the neutrinos generated at the neutrino sphere by stationary accretion of infalling matter.

We list our finite difference representation of each term in the Boltzmann equation and derive moments and other derived quantities. This procedure is essential to obtain detailed information on truncation errors, which are then compensated with selected finite differencing of other terms for perfect number and sufficient energy conservation. Moreover, we algebraically derive the finite difference representation of the diffusive limit, the nonrelativistic limit, and the radial dependence of the flux factor in a stationary state free streaming radiation field. These algebraic gymnastics lead to a better understanding of the internal mechanisms in our finite difference representation and, by comparison with the code results, enhances the confidence that the implementation exactly corresponds to the programmer’s intention. Besides the diffusion and free streaming limits, we check the implementation of the gravitational redshift and light bending. The dynamic observer corrections determine the continuity of the radiation quantities at the shock discontinuity. A transformation from the comoving into the laboratory frame indicates their correct implementation. The event of the neutrino burst is well suited to test the propagation of a radiation pulse through the outer layers of the star. The pulse shows the expected propagation speed, but is quickly broadened

by diffusion. We quantitatively relate this diffusion to the first order upwind differencing used in our radiation transport. Quite generally, we find that the choice of first order upwind differencing represents the limiting factor of the accuracy in our numerical solution. In space, it causes artificial pulse diffusion. In momentum space, it causes angular diffusion in the evolution of the particle distribution function. Finally, a limited resolution in energy may cause artificial variations in the reaction rates under degenerate conditions when the Fermi energy of the particles is not properly resolved (Mezzacappa & Bruenn 1993b). Although these limitations are easy overcome by choosing higher resolution, a more elaborate advection scheme or an adaptive grid for the radiation part might also improve the accuracy of the scheme without challenging the computer memory. In the supernova application, however, a reasonably low resolution appears to produce accurate physical results because the effects of low order upwind differencing predominantly affect the regions far from the neutrinospheres, where the radiation field is decoupled from the matter and adverse influence on the dynamics of the model can be excluded. We test the overall consistency of our radiation hydrodynamics code with a detailed energy conservation analysis. We track each term in the Boltzmann equation through the evolution of a $40 M_{\odot}$ star and demonstrate which terms have to be matched in what phases of the postbounce evolution. Finally we compare the evolution of a $13 M_{\odot}$ star with another new general relativistic code based on the Multi-Group Flux-Limited Diffusion approximation (Bruenn et al. 2002). We find excellent agreement. There is no situation in the evolution of our spherically symmetric postbounce simulation that could not equally well be treated with the MGFLD approximation, provided the flux limiter is sophisticated enough.

With the exponentially growing power of computer hardware, computational astrophysics may reach a comparable status in astronomical, nuclear and particle physics research as terrestrial experiments have received in the previous century. We may sort scientific progress into three phases: First, the astronomical observation or a new theoretical concept (e.g. the existence of neutrons in the history of core collapse supernova theory) lead to a primary idea about the basic physics responsible for the event (core collapse to protoneutron star formation with bounce). At this stage, order of magnitude estimates are made and compared to the qualitative observational data. The second step involves plausibility studies of the suggested scenario, which may include detailed numerical simulations and comparisons to observations. Often, however, approximations have to be used that are dictated by technical limitations in the newly developing field. Only in the simplest cases can it be shown that all assumptions are based on undeniably justifiable physical considerations. This exciting phase of discovery and controversy should be followed by more rigorous numerical simulations in a third step, when technical limitations fade and remaining approximations become quantifiable. This phase has to be accompanied by rigorous code documentation that allows independent researchers to analyse and eventually reproduce the numerical results, similar to the way the value of experimental data is enhanced by a detailed description of the reproducible experiment. The recent emergence of functional Boltzmann solvers leads the radiation hydrodynamics in spherically symmetric supernova models into this third phase. The third phase, by principle, should be accompanied by solid agreement in the numerical solution found with independent implementations of the same physical ingredients. In order to perform such comparisons, we appreciate the situation that

a basic set of standard nuclear and weak interaction physics has been defined and used for 15 years (e.g. (Tubbs & Schramm 1975; Schinder & Shapiro 1982; Bruenn 1985)). By a comparison with the second phase—which used the former standard scheme for neutrino transport in supernovae—Multi-Group Flux-Limited Diffusion, we hope to increase the confidence in our results on the one hand, while, on the other hand, we strongly support the validity of the MGFLD approximation in spherical symmetry as well. As satisfying as these close results are, they should not be mistaken as an example of convergence to agreement in the sense of the third phase. The third phase is only reached if similar agreement is found between independent groups and other ambitious codes that solve physically complete neutrino transport equations, such as, e.g., the well-documented implementation of the variable Eddington factor method by (Rampp & Janka 2002). We hope that our effort to dispel uncertainties in the neutrino transport in spherical symmetry presents a first step to guide the more comprehensive multi-dimensional supernova models from phase two, where we certainly allocate most of them at present time, into an extraterrestrial laboratory in the sense of phase three. Spherically symmetric and general relativistic supernova models with accurate and detailed neutrino information may meanwhile be used for a continued exploration and improvement of the local microscopic input physics.

We thank Raph Hix for fruitful discussions and comments on the manuscript. We enjoyed discussions with Markus Rampp, Thomas Janka, Gabriel Martinez-Pinedo, and Karlheinz Langanke. We acknowledge support from the National Science Foundation under contract AST-9877130, the Oak Ridge National Laboratory, managed by UT-Batelle, LLC, for the U.S. Department of Energy under contract DE-AC05-00OR22725, the Swiss National Science Foundation under contract 20-61822.00, the NSF under contract 96-18423, the NASA under contract NAG5-3903, the Joint Institute for Heavy Ion Research, a DOE PECASE Grant, and the DOE HENP Scientific Discovery through Advanced Computing Program. Our simulations were carried out on the National Energy Research Supercomputer Center Cray SV-1.

A. $\mathcal{O}(v/c)$ limit of the finite difference representation

The $\mathcal{O}(v/c)$ Boltzmann equation has been derived by Castor (1972). One can also obtain it by directly dropping the higher order terms from Eq. (15), i.e. by setting $\alpha = \Gamma = \text{const.} = 1$ and replacing u by the nonrelativistic velocity v . The conservation properties of the $\mathcal{O}(v/c)$ Boltzmann equation become apparent when we take its energy and angular moments (Mihalas & Mihalas 1984):

$$\begin{aligned} \frac{\partial J}{\partial t} + \frac{\partial}{\partial a} [4\pi r^2 \rho H] + \frac{v}{r} (J - K) - \left(\frac{\partial \ln \rho}{\partial t} + \frac{2v}{r} \right) K \\ - \int \frac{j}{\rho} E^3 dE d\mu + \int \chi F E^3 dE d\mu = 0, \end{aligned}$$

$$\begin{aligned} \frac{\partial H}{\partial t} + \frac{\partial}{\partial a} [4\pi r^2 \rho K] - \frac{1}{r} (J - K) - \left(\frac{\partial \ln \rho}{\partial t} + \frac{2v}{r} \right) H \\ + \int \chi F E^3 dE \mu d\mu = 0. \end{aligned} \quad (\text{A1})$$

As we construct the specific radiation energy in the laboratory frame, $J + vH$, we keep *all* terms that arise from the $O(v/c)$ Boltzmann equation and obtain, in analogy to Eq. (25), an almost conservative evolution equation for the radiation moments,

$$\begin{aligned} 0 = & \frac{\partial}{\partial t} (J + vH) + \frac{\partial}{\partial a} [4\pi r^2 \rho (vK + H)] \\ & - \int \frac{j}{\rho} E^3 dE d\mu + \int \chi F E^3 dE d\mu + v \int \chi F E^3 dE \mu d\mu \\ & - \frac{1}{4\pi r^2 \rho} \frac{\partial}{\partial t} (4\pi r^2 \rho v) H. \end{aligned} \quad (\text{A2})$$

Although terms of higher order than (v/c) , especially the gravitational terms, require consideration in realistic supernova simulations, the $O(v/c)$ limit may be used for various explorative studies. A corresponding finite difference representation of the Boltzmann equation can be derived from the general relativistic expressions by simply setting $\alpha = \Gamma = 1$. The terms that constitute the $O(v/c)$ Boltzmann equation, are then given by

$$C_t = \frac{F_{i',j',k'} - \bar{F}_{i',j',k'} \frac{da_{i'}}{dt}}{dt} + \frac{1}{da_{i'}} \left[u_{i+1}^{\text{rel}} F_{i+1,j',k'}^* - u_i^{\text{rel}} F_{i,j',k'}^* \right] \quad (\text{A3})$$

$$D_a = \frac{\mu_{j'}}{da_{i'}} \left[4\pi r_{i+1}^2 \rho_{i+1} F_{i+1,j',k'} - 4\pi r_i^2 \rho_i F_{i,j',k'} \right] \quad (\text{A4})$$

$$D_\mu = \frac{3[r_{i+1}^2 - r_i^2]}{2[r_{i+1}^3 - r_i^3]} \frac{1}{w_{j'}} (\zeta_{j+1} F_{i',j+1,k'} - \zeta_j F_{i',j,k'}) \quad (\text{A5})$$

$$\begin{aligned} O_E = & \frac{1}{E_{k'}^2 dE_{k'}} \left[(\mu_{j'}^2 A_{i',k'-dk} - B_{i',j'}) \frac{dE_{k'-dk}}{E_{k'} - E_{k'-dk}} E_{k'-dk}^3 F_{i',j',k'-dk} \right. \\ & \left. - (\mu_{j'}^2 A_{i',k'} - B_{i',j'}) \frac{dE_{k'}}{E_{k'+dk} - E_{k'}} E_{k'}^3 F_{i',j',k'} \right] \end{aligned} \quad (\text{A6})$$

$$\begin{aligned} O_\mu = & \frac{1}{w_{j'}} \left[(A_{i',k'} + B_{i',j'-dj}/\zeta_{j'-dj}) \frac{w_{j'-dj}}{\mu_{j'} - \mu_{j'-dj}} \zeta_{j'-dj} \mu_{j'-dj} F_{i',j'-dj,k'} \right. \\ & \left. - (A_{i',k'} + B_{i',j'}/\zeta_{j'}) \frac{w_{j'}}{\mu_{j'+dj} - \mu_{j'}} \zeta_{j'} \mu_{j'} F_{i',j',k'} \right] \end{aligned} \quad (\text{A7})$$

$$C_c = \frac{j_{i',k'}(\rho_{i'}, T_{i'}^*, Y_{e,i'}^*)}{\rho_{i'}} - \chi_{i',k'}(\rho_{i'}, T_{i'}^*, Y_{e,i'}^*) F_{i',j',k'}. \quad (\text{A8})$$

The expressions basically reduce to the finite difference representation described in (Mezzacappa & Bruenn 1993a), except for the adaptive grid extension, the new code flow outlined in section 3.4, the improved choice of transport coefficients $\beta_{i,k'}$ and $\gamma_{i',k'}$, in Eq. (37), the new discretization of angular aberration, and the matched finite difference representation of $A_{i',k'}$ and $B_{i',j',k'}$ (Liebendörfer

2000),

$$A_{i',k'} = \frac{4\pi\rho_{i'}}{da_{i'}} (r_{i+1}^2 (v_{i+2} - v_{i+1}) \beta_{i+1,k'} + r_i^2 (v_{i+1} - v_i) (1 - \beta_{i,k'})) \quad (\text{A9})$$

$$B_{i',j',k'} = \frac{3r_{i+1}^2 - r_i^2}{2r_{i+1}^3 - r_i^3} \frac{v_{i+1}}{w_{j'}} [\gamma_{i',k'} \zeta_{j+1} (\mu_{j'+1} - \mu_{j'}) + (1 - \gamma_{i',k'}) \zeta_j (\mu_{j'} - \mu_{j'-1})]. \quad (\text{A10})$$

The angular difference coefficients, ζ_j , are defined in Eq. (43). In the spherically symmetric implementation of radiative transfer in terms of comoving particle momenta, these two important matches in table (30), ($D_a^4 O_E^1$) and ($D_\mu^{12} O_E^{34}$), establish overall energy conservation to $O(v/c)$. On a Lagrangian grid, a finite difference expression for energy conservation according to Eq. (A2) is obtained by the application of the operator $\sum_j (1 + v_{i+1} \mu_{j'})$ to the finite differenced Boltzmann equation described in Eqs. (A3)-(A10). Since there is no gravitational frequency shift, and the velocities v/c can be assumed to be small in the Newtonian limit, the update of the observer corrections O_E and O_μ can be implemented with explicit finite differencing as in (Messer 2000; Mezzacappa et al. 2001).

B. Particle advection on a dynamically adaptive grid

AGILE-BOLTZTRAN has the capability to dynamically adapt the computational grid to the evolution of the stellar profile. The scheme allows the concentration of the zones for the computationally expensive implicit solution of the full Boltzmann equation to domains where radiation transport is active and important. It also allows a proper shock capturing and propagation. Since the method of a dynamically adaptive grid has already been described in other places (e.g. (Winkler, Norman, & Mihalas 1984; Dorfi & Drury 1987; Liebendörfer, Rosswog & Thielemann 2002)), we just resume in this appendix its impact on the discretization of the Boltzmann equation presented above. The adaptive grid affects above all the evaluation of time derivatives. We have therefore payed attention to reduce the occurence of time derivatives to a minimum in the implementation of the Boltzmann equation. However, a few wrinkles have still to be considered:

Let us imagine that we are sitting in the center of a zone and are observing a nonzero neutrino radiation field. Now the adaptive grid moves a boundary of the zone towards us. We know the baryon flux that is leaving our zone into the neighbor zone. From this information it is simple to calculate the new zone averages for the conserved specific volume, energy and momentum that are attached to the baryons. It is however not as trivial to calculate the new specific neutrino distribution function averages since the description of the neutrino in the comoving frame momentum phase space depends on the position of the neutrino in the spatial phase space. Unless we use a description that decouples the momentum phase space as e.g. the view of distant inertial observer, we should correct the state of the neutrino in the momentum phase space when it is assigned to new fluid elements at a different position and with a different velocity. In the decoupled description, we argued in (Liebendörfer, Mezzacappa, & Thielemann 2001), Eq. (40)-(41)) that the impact

parameter, b , and the particle energy at infinity, ε , are nearly independent of the particle position,

$$\begin{aligned} b &= r \frac{\sqrt{1 - \mu^2}}{\Gamma + u\mu} \\ \varepsilon &= (\Gamma + u\mu) E. \end{aligned} \quad (\text{B1})$$

Any change in radius, r , or velocity, u , of the fluid element where the neutrino is assigned to, leads to a change in the propagation angle, μ , and energy, E , of the neutrino if it is supposed to maintain its kinematic parameters in the view of an inertial observer. It is not all to consider the neutrinos that are assigned to a neighbor zone! Also the state of the neutrinos that remain in the zone need to be corrected: By moving a boundary of the zone, the zone center is redefined and since the state in neutrino momentum phase space refers to the zone center radius, it also needs to be transformed to the displaced zone center and the new zone average velocity. In the more general derivation of the adaptive grid equations in Winkler and Norman (Winkler, Norman, & Mihalas 1984), these two corrections do not appear. In order to convince ourselves that they cancel, we do the following exercise of calculating them explicitly.

Following the rules of the adaptive grid technique, we start by applying the Reynolds theorem to the specific neutrino distribution function $\hat{F}(t, a, b, \varepsilon)$ that is written in terms of invariant momentum phase space coordinates. Within this description we may move and average neutrino distribution functions without affecting the momentum state of the neutrinos

$$\frac{\partial}{\partial t} \int_{a(q_1)}^{a(q_2)} \hat{F} da + \left[-\hat{F} \frac{\partial a}{\partial t} \right]_{q_1}^{q_2} = \int_{a(q_1)}^{a(q_2)} \frac{d\hat{F}}{dt} da. \quad (\text{B2})$$

Partial time derivatives $\partial/\partial t$ are taken at constant grid label q and Lagrangian derivatives d/dt at constant baryon mass a . Evaluating the first term by the chain rule gives

$$\begin{aligned} \frac{\partial}{\partial t} \int_{a(q_1)}^{a(q_2)} \hat{F} da &= \frac{\partial}{\partial t} \int_{a(q_1)}^{a(q_2)} F da \\ &+ \int_{a(q_1)}^{a(q_2)} \left[\frac{\partial F}{\partial \mu} \frac{\partial \mu}{\partial t} + \frac{\partial F}{\partial E} \frac{\partial E}{\partial t} \right] da + \int_{q_1}^{q_2} (\hat{F} - F) \frac{\partial}{\partial t} \frac{\partial a}{\partial q} dq \end{aligned} \quad (\text{B3})$$

and the second term can be written as

$$\begin{aligned} \left[\hat{F} \frac{\partial a}{\partial t} \right]_{q_1}^{q_2} &= \left[F \frac{\partial a}{\partial t} \right]_{q_1}^{q_2} \\ &+ \int_{a(q_1)}^{a(q_2)} \left[\frac{\partial F}{\partial \mu} \frac{\partial \mu}{\partial a} + \frac{\partial F}{\partial E} \frac{\partial E}{\partial a} \right] \frac{\partial a}{\partial t} da + \int_{a(q_1)}^{a(q_2)} (\hat{F} - F) \frac{\partial}{\partial a} \frac{\partial a}{\partial t} da. \end{aligned} \quad (\text{B4})$$

While the term on the right hand side evaluates to

$$\int_{a(q_1)}^{a(q_2)} \frac{d\hat{F}}{dt} da = \int_{a(q_1)}^{a(q_2)} \frac{dF}{dt} da + \int_{a(q_1)}^{a(q_2)} \left[\frac{\partial F}{\partial \mu} \frac{d\mu}{dt} + \frac{\partial F}{\partial E} \frac{dE}{dt} \right] da. \quad (\text{B5})$$

Substitution of expressions (B3)-(B5) into Eq. (B2) shows that the correction terms indeed cancel. Hence, we can directly apply the Reynolds theorem to the neutrino distribution functions in the comoving frame

$$\frac{\partial}{\partial t} \int_{a(q_1)}^{a(q_2)} F da + \left[-F \frac{\partial a}{\partial t} \right]_{q_1}^{q_2} = \int_{a(q_1)}^{a(q_2)} \frac{dF}{dt} da. \quad (\text{B6})$$

The corresponding numerical tests show that we give up machine precision in $O(v/c)$ energy conservation due to the finite difference representation of the integral, but the deviation is small enough to not adversely affect the physical outcome of our simulations.

In the finite difference representation, Eq. (B6) reads

$$\frac{F_{i',j',k'} da_{i'} - \bar{F}_{i',j',k'} \bar{d}a_{i'}}{dt} + \left[u_{i+1}^{\text{rel}} F_{i+1,j',k'}^* - u_i^{\text{rel}} F_{i,j',k'}^* \right] = \left(\frac{dF}{dt} \right)_{i'} da_{i'}, \quad (\text{B7})$$

where $u_i^{\text{rel}} = -(a_i - \bar{a}_i) / dt$ is the relative mass-velocity between the zone edges and the rest mass. The zone edge neutrino distribution function is found by upwind differencing:

$$F_{i,j',k'}^* = \begin{cases} F_{i'-1,j',k'} & \text{if } u_i^{\text{rel}} \geq 0 \\ F_{i',j',k'} & \text{otherwise.} \end{cases} \quad (\text{B8})$$

Note that the advection in this case is determined by the unlimited grid velocity, and not by the mean free path of the propagating particles. We can therefore not apply the same interpolating transport coefficients as with the advection due to particle propagation in Eq. (37). If we divide Eq. (B7) by the zone rest mass $da_{i'}$ and the lapse function $\alpha_{i'}$, we obtain the adaptive grid corrections that we have already included in Eq. (35) and (A3).

There is one other occurrence of a time derivative du/dt in Eq. (57). We determine the zone center relative velocity $u_{i'}^{\text{rel}}$ as an arithmetic mean of the zone edge values, and the dynamic zone edge rest mass da_i as an arithmetic mean of the zone center values. The Reynolds theorem applied to the velocity leads to

$$\frac{du}{dt} = \frac{u_i - \bar{u}_i \frac{\bar{d}a_i}{da_i}}{dt} + \frac{1}{da_i} \left[u_{i'}^{\text{rel}} u_{i'}^* - u_{i'-1}^{\text{rel}} u_{i'-1}^* \right]. \quad (\text{B9})$$

The zone center velocity is again found by upwind differencing:

$$u_{i'}^* = \begin{cases} u_i & \text{if } u_{i'}^{\text{rel}} \geq 0 \\ u_{i+1} & \text{otherwise.} \end{cases}$$

C. Experiences with previously used finite differencing

Our previous code version used in (Liebendörfer 2000; Mezzacappa et al. 2001; Liebendörfer et al. 2001) applied the observer corrections in Eq. (56), (58), and (61) in an operator split way.

This is fully justifiable in the Newtonian limit, where these corrections are small in the diffusive regime. In the general relativistic context however, we may have an appreciable frequency shift on individual propagation directions in the protoneutron star: a blueshift for ingoing particles and a redshift for outgoing particles. On the other hand, the particles stand in thermodynamical equilibrium with matter at high densities and tend to assume an isotropic angular distribution. These two contradictory affinities are strongly coupled and should not be operator split. Although the result of the simulations have not been affected by frequent iterations, the time step in our former general relativistic calculations was severely impeded by the forth and back corrections with respect to the frequency shift. The inclusion of all observer corrections into the general implicit solution for the radiation quantities has remedied this restriction on the time step.

We could improve the implementation of the general relativistic terms. From the physical point of view, we have added the gravitational backreaction of the neutrinos. We now neglect only some high order (in G/c^2) field quantities in the coefficients of the Boltzmann equation that do not enter the evolution of macroscopic quantities. From the numerical point of view, we have extended the error matching technique from the $O(v/c)$ corrections (Mezzacappa & Bruenn 1993a; Liebendörfer 2000) to the higher order relativistic terms. In previous code versions, we have used a more natural finite difference representation of $\Gamma \partial \Phi / \partial r$ in Eqs. (48) and (57). The former choice, together with the neglection of the gravitational backreaction, were sufficient for an accurate evolution of the lightweight $13M_\odot$ progenitor star. More massive progenitors, however, developed after a few hundred milliseconds a compactness that lead to energy conservation violations of order of several explosion energies with the unmatched general relativistic terms.

The third improvement is related to the choice of the transport coefficients in Eq. (37). As explained in detail in the next section, our present choice more rigorously eliminates numerical truncation errors from the equilibrium field in the diffusive flux than the previous setting defined in (Mezzacappa & Bruenn 1993a), Eq. (91). We now obtain about 10% smaller luminosities in all neutrino flavors. As a consequence, the maximum shock also reduces from nearly 200 km to about 180 km.

Last and least, we have marginally improved our adhoc treatment of silicon to nuclear statistical equilibrium (NSE) conversion. We assume an (unphysically) distinct separation between zone i in NSE and zone $i + 1$ from the silicon layer. In a Lagrangian scheme, we would simply convert zone $i + 1$ to NSE during infall as soon as the burning time scale becomes considerably smaller than the evolution time scale. The conversion from a given composition to NSE is handled such that energy remains conserved with the respective equations of state. With the dynamical adaptive grid, we additionally apply this conversion to continuous mass advection between zone i and $i + 1$. In the case of an inwards moving grid, advection from zone i to zone $i + 1$ led to the transient conversion of advected material labelled with “NSE” to “silicon” until enough advected NSE material into zone $i + 1$ triggered the conversion of zone $i + 1$ back to the physically unchanged NSE. In our most recent code version, we buffer unphysical NSE to silicon conversion until a relabelling of zone $i + 1$ can be made. This avoids adverse effects to the thermodynamical state at the transition between

layers with different composition.

D. Attenuation factors for the presentation of interaction rates

Whenever one composes a graph for the discussion of weak interaction rates in the supernova environment, one has to circumvent the inherently large scale differences of the rates at different locations in the star. Many details are hidden in a logarithmic presentation and scale differences between absorption and emission are difficult to appreciate. One possible way out is to focus on the neutrinospheres and to investigate the rates of interest under the corresponding conditions. However, the definition of the neutrino sphere is only based on the opacity and does not account for eventual large emissivities outside the neutrino sphere. An investigation of the environment at the neutrinosphere may miss important sources of the total neutrino luminosity and fail in the explanation of the spectra. Moreover, it is common to average the extremely energy-dependent location where a given optical depth is reached to one single neutrinosphere—an even more problematic concept. In this appendix, we motivate a convenient presentation of interaction rates according to their relevance to the total luminosities. The approach aims to produce intuitively accessible figures with information about where the neutrinos come from, which reactions contribute to the total luminosity, how they locally compare to other reactions, and how the neutrino spectra are formed.

We derive the auxiliary attenuation factors in terms of a staggered grid with zone edge indices i and zone center indices $i' = i + 1/2$. We start with a conserved flux H_i through spheres around the symmetry center. We may choose the neutrino number flux in units of particles per second or the neutrino luminosity in ergs per second. Each zone may have a number or energy source, $em_{i'}$, and a number or energy sink, $ab_{i'}$, in number or ergs per gram and second. The flux is then recursively defined by its central value $H_0 = 0$ and

$$H_{i+1} = H_i + (em_{i'} - ab_{i'}) da_{i'}, \quad (D1)$$

where $da_{i'}$ denotes the rest mass contained in the mass shell i' . Subject to absorption in this shell are the entering flux, H_i , plus the source, $em_{i'} da_{i'}$. We define an attenuation factor, $x_{i+1} \leq 1$, which reduces this input by the amount of absorption in the shell,

$$H_{i+1} = x_{i+1} (H_i + em_{i'} da_{i'}). \quad (D2)$$

From Eq. (D1) and (D2), we can readily isolate x_i :

$$x_i = \frac{H_i}{H_{i-1} + em_{i'-1} da_{i'-1}} = \frac{H_i}{H_i + ab_{i'-1} da_{i'-1}}.$$

In the rare cases of a negative x_i , we set x_i to zero. If we calculate a mean free path, $\lambda_{i'}$, from all reactions that may act as a sink, the absorption rate can also be derived from the local specific number or energy density, $J_{i'}$, according to $ab_{i'} = cJ_{i'}/\lambda_{i'}$. The attenuation factor x_i can then

be expressed by physical quantities that are well accessible in a numerical evolution of radiation hydrodynamics,

$$x_i = \frac{H_i}{H_i + \frac{cJ_{i'-1}}{\lambda_{i'-1}} da_{i'}}. \quad (\text{D3})$$

On the other hand, we derive from Eq. (D2) by two recursive self-substitutions,

$$H_{i+1} = x_{i+1} (x_i (x_{i-1} (H_{i-2} + em_{i'-2} da_{i'-2}) + em_{i'-1} da_{i'-1}) + em_{i'} da_{i'}).$$

The continuation to $H_0 = 0$ and a rearrangement of the terms leads to

$$H_{n+1} = \sum_{i=1}^n \left(\prod_{k=i+1}^{n+1} x_k \right) em_{i'} da_{i'}. \quad (\text{D4})$$

This equation describes how the total number flux or luminosity at a radius r_{n+1} is composed by contributions of distributed emissivities in the star. The attenuation coefficients

$$\xi_{n+1,i'} = \prod_{k=i+1}^{n+1} x_k = \prod_{k=i+1}^{n+1} \frac{H_k}{H_k + \frac{cJ_{k'-1}}{\lambda_{k'-1}} da_{i'}} \quad (\text{D5})$$

suppress irrelevant sources that are subject to large reabsorption. We can use the attenuation coefficients in many convenient ways. One may, e.g., disentangle the emissivities and absorptivities into separate reactions and/or energy groups, $em_{i'}(l)$, and $ab_{i'}(l)$. A figure with l graphs showing

$$g_{n+1}^l(r_{i'}) = \xi_{n+1,i'} em_{i'}(l) \frac{4\pi}{3} (r_{i+1}^2 + r_{i+1} r_i + r_i^2) \rho_{i'} \quad (\text{D6})$$

as a function of radius $r_{i'}$ (where $\rho_{i'}$ is the rest mass density) would visualize by the enclosed area under line l the contribution of reaction l to the total luminosity at radius r_{n+1} . If l labels energy groups instead and the distinction between energy groups has been made in the definition of λ , the formation of the neutrino spectrum immediately becomes apparent. The shape of the lines and their maxima make evident where the neutrinos of type l originate. Type l may refer to a specific energy group, a specific neutrino flavor, a specific production reaction, and furthermore. The graph is automatically scaled such that the most important reactions for the total luminosity are presented most prominently. One may additionally plot absorption or scattering rates with the attenuation coefficients,

$$h_{n+1}^l(r_{i'}) = \xi_{n+1,i'} ab_{i'}(l) \frac{4\pi}{3} (r_{i+1}^2 + r_{i+1} r_i + r_i^2) \rho_{i'}. \quad (\text{D7})$$

Although attenuated absorption and scattering rates do not have any physical meaning in the global picture, they allow a direct local comparison of rates in the regions where the neutrino luminosities and spectra are formed. Finally, we mention the potential use of the attenuation coefficients for statistical evaluations, e.g. for the root mean square radius of neutrino production,

$$r_{rms} = \left(\frac{\sum_{i=1}^n r_{i'}^2 \xi_{n+1,i'} em_{i'} da_{i'}}{\sum_{i=1}^n \xi_{n+1,i'} em_{i'} da_{i'}} \right)^{1/2}. \quad (\text{D8})$$

In contrast to the classical definition of the neutrinosphere, the quantity r_{rms} accounts for regions with high emissivities in transparent regimes. Many other statistical informations at the origin of the neutrino emission may be obtained analogously. As a check of the approach we compare in Fig. (23) the luminosities H_{n+1} with the reconstructed luminosities given by Eq. (D4).

REFERENCES

Arnett, W. D. 1967, Canadian J. of Phys., 215, 1621

Arnett, W. D. 1977, ApJ, 218, 815

Arnowitt, A., Deser, S., & Misner, C. W. 1962, in Gravitation: An Introduction to Current Research, ed. L. Witten (New York: Wiley)

Baron E., Cooperstein J., & Kahana, S. 1985, Phys. Rev. Lett., 55, 126

Baumgarte, T. W., Janka, H.-T., Keil, W., Shapiro, S. L., & Teukolsky, S. A. 1996, ApJ, 468, 823

Bethe, H. A. & Wilson, J. R. 1985, ApJ, 295, 14

Bethe, H. A. 1990, Rev. Mod. Phys., 62, 801

Bowers, R. L. & Wilson, J. R. 1982, ApJS, 50, 115

Bruenn, S. W. 1985, ApJS, 58, 771

Bruenn, S. W., DeNisco, K. R., & Mezzacappa, A. 2001, ApJ, 560, 326

Bruenn, S. W. et al. 2002, in preparation

Burrows, A., Hayes, J., & Fryxell, B. A. 1995, ApJ, 450, 830

Burrows, A., Young, T., Pinto, Ph., Eastman, R. & Thompson, T. A. 2000, ApJ, 539, 865

Castor, J. I. 1972, ApJ, 178, 779

Colgate, S. A. & White, R. H. 1966, ApJ, 143, 626

Dorfi, E. A., & Drury, L. O’C. 1987, J. Comput. Phys., 69, 175

Fryer, C. F. & Heger 2000, A., ApJ, 541, 1033

Fryer, C. F. & Warren, M. S. 2002, to be published in ApJ

Galama, T. J., et al. 1998, Nature, 395, 670

Glendenning, N. K. 1985, ApJ, 293, 470

Herant, M., Benz, W., & Colgate, S. A. 1992, *ApJ*, 395, 642

Herant M., Benz W., Hix R. W., Fryer C. L., & Colgate, S. A. 1994, *ApJ*, 435, 339

Höflich, P., Wheeler, J. C., & Wang, L. 1999, *ApJ*, 521, 179

Janka, H.-T. 1992, *A&A*, 256, 452

Janka, H.-T. & Müller, E. 1996, *A&A*, 306, 167

Janka, H.-T., Kifonidis, K., & Rampp, M. 2001, in Proc. Workshop on Physics of Neutron Star Interiors, ed. D. Blaschke, N. Glendenning, & A. Sedrakian, Lecture Notes in Physics (Germany: Springer), 333

Khokhlov, A. M., Höflich, P. A., Oran, E. S., Wheeler, J. C., Wang, L., & Chtchelkanova, A. Yu. 1999, *ApJ*, 524, 107

Lattimer, J. & Swesty, F. D. 1991, *Nucl. Phys.*, A535, 331

Leonard, D. C., Filippenko, A. V., Barth, A. J., & Matheson, T. 2000, *ApJ*, 536, 239

Lewis, E. E. & Miller Jr., W. F. 1993, Computational Methods of Neutron Transport, (La Grange Park, Illinois: American Nuclear Society, Inc.)

Liebendörfer, M. 2000, Ph.D. thesis (Basel: University of Basel)

Liebendörfer, M., Mezzacappa, A., & Thielemann, F.-K. 2001, *Phys. Rev. D*, 63, 104003

Liebendörfer, M., Mezzacappa, A., Thielemann, F.-K., Messer, O. E. B., Hix, W. R., & Bruenn, S. W. 2001, *Phys. Rev. D*, 63, 103004

Liebendörfer, M., Messer, O. E. B., Mezzacappa, A., & Hix, W. R. 2001, in Proceedings of the 20th Texas Symposium on Relativistic Astrophysics, ed. by J. C. Wheeler & H. Martel (American Institute of Physics), 472

Liebendörfer, M., Messer, O. E. B., Mezzacappa, A., Hix, R., Thielemann, F.-K., & Langanke, K. 2002, Proc. of the 11th Workshop on Nuclear Astrophysics, ed. W. Hillebrandt & E. Müller (Garching b. München: Springer)

Liebendörfer, M., Rosswog, S. K., & Thielemann, F.-K. 2002, *ApJS*, 141, 229

Lindquist, R. W. 1966, *Ann. Phys.*, 37, 487

MacFadyen, A. I. & Woosley, S. E. 1999, *ApJ*, 524, 262

May, M. M. & White, R. H. 1967, *Comput. Phys.*, 7, 219

Messer, O. E. B., Mezzacappa, A., Bruenn, S. W., & Guidry, M. W. 1998, *ApJ*, 507, 353

Messer, O. E. B. 2000, Ph.D. thesis (Knoxville: University of Tennessee)

Messer, O. E. B. et al. 2002, in preparation

Mezzacappa, A. & Matzner, R. A. 1989, *ApJ*, 343, 853

Mezzacappa, A. & Bruenn, S. W. 1993, *ApJ*, 405, 669

Mezzacappa, A. & Bruenn, S. W. 1993, *ApJ*, 405, 637

Mezzacappa, A. & Bruenn, S. W. 1993, *ApJ*, 410, 740

Mezzacappa, A., Calder, A. C., Bruenn, S. W., Blondin, J. M., Guidry, M. W., Strayer, M. R., & Umar, A. S. 1998, *ApJ*, 495, 911

Mezzacappa, A. & Messer, O. E. B. 1999, *JCAM*, 109, 281

Mezzacappa, A., Liebendörfer, M., Messer, O. E. B., Hix, W. R., Thielemann, F.-K., & Bruenn, S. W. 2001, *PRL*, 86, 1935

Mihalas, D. & Weibel-Mihalas, B. 1984, Foundations of Radiation Hydrodynamics, (Oxford University Press)

Miller, D. S., Wilson, J. R., & Mayle, R. W. 1993, *ApJ*, 415, 278

Misner, C. W., & Sharp, D. H. 1964, *Phys. Rev.*, B136, 571

Myra, E. S., Bludman, S. A., Hoffman, Y., Lichtenstadt, I., Sack, N., & Van Riper, K. A. 1987, *ApJ*, 318, 744

Myra, E. S. & Bludman, S. A. 1989, *ApJ*, 340, 384

Nomoto, K. & Hashimoto, M. 1988, *Phys. Rep.*, 163, 13

Pons, J. A., Reddy, S., Prakash, M., Lattimer, J. M., & Miralles, J. A. 1999, *ApJ*, 513, 780

Rampp, M. & Janka, H. T. 2000, *ApJ*, 539, L33

Rampp, M. & Janka, H. T. 2002, *astro-ph/0203101*

Rezzolla, L. & Miller, J. C. 1994, *Class. Quantum Grav.*, 11, 1815

Schinder, P. J. & Shapiro, S. L. 1982, *ApJS*, 50, 23

Schinder, P. J. & Bludman, S. A. 1989, *ApJ*, 346, 350

Schwartz, R. A. 1967, *Ann. Phys.*, 43, 42

Smarr, L. & York, J. W. 1978, *Phys. Rev.*, D17, 2529

Smit, J. M., van den Horn, L. J., & Bludman, S. A. 2000, A&A, 356, 559

Strom., R., Johnston, H. M., Verbunt, F., & Aschenbach, B. 1995, Nature, 373, 587

Swesty, F. D. 1995, ApJ, 445, 811

Tubbs, D. & Schramm, D. 1975, ApJ, 201, 467

Tueller, J., Barthelmy, S., Gehrels, N., Leventhal, M., MacCallum, C. J., & Teegarden, B. J. 1991, in Supernovae, ed. by Woosley, S. E. (Berlin: Springer), 278

Van Riper, K. A. 1979, ApJ, 232, 558

Van Riper, K. A., & Lattimer, J. M. 1981, ApJ, 249, 270

Wheeler, J. C., Yi, I., Höflich, P. & Wang, L. 2000, ApJ, 537, 810

Wilson, J. R. 1971, ApJ, 163, 209

Wilson, J. R. 1985, in Numerical Astrophysics, ed. by Centrella, J. M., LeBlanc, J. M., & Bowers, R. L. (Boston: Jones and Bartlett)

Winkler, K.-H., Norman, M. L., & Mihalas, D. 1984, J. Quant. Spectrosc. Radiat. Transf., 31, 473

Woosley, S. E., Weaver, T. A. 1995, ApJS, 101, 181

Yamada, S. 1997, ApJ, 475, 720

Yamada, S., Janka, H.-T., & Suzuki, H. 1999, A&A, 344, 533

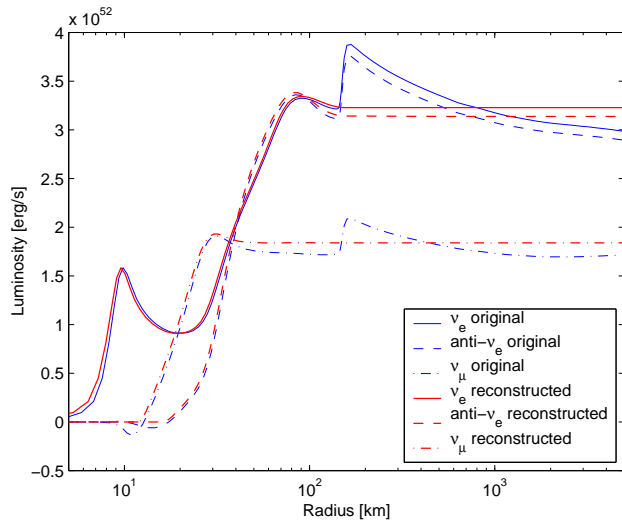


Fig. 23.— A comparison of the original luminosity with the reconstructed luminosity by the attenuation coefficients. The reconstruction obviously misses the observer corrections in regions with low interaction rates. Otherwise, it is accurate. The luminosities have been taken from the evolution of the $13 M_{\odot}$ progenitor at 100ms after bounce.